A COMPREHENSIVE STUDY OF THE MICROSTRUCTURE AND MECHANICAL BEHAVIOR OF HCP-BASED MULTILAYERED NANOFILMS

by

Yuanyuan Lu

A dissertation submitted to the faculty of
The University of North Carolina at Charlotte
in partial fulfillment of the requirements
for the degree of Doctor of Philosophy in
Mechanical Engineering

Charlotte

2014

Approved by:

_____
Dr. Qiuming Wei

_____
Dr. Ronald Smelser

_____
Dr. Aixi Zhou

_____
Dr. Haitao Zhang

_____
Dr. Jing Zhou

ABSTRACT

YUANYUAN LU. A comprehensive study of the microstructure and mechanical behavior of HCP-based multilayered nanofilms
(Under the direction of Dr. QIUMING WEI)

Metallic multilayer films with the individual layer thickness *h* decreased to submicron or even less have attracted a great deal of attention over the past decades because of their impressive mechanical properties, especially the high strength. Most experimental and analytical efforts in this research field have been endeavored to the multilayer films composed of body-centered cubic (BCC) or face-centered cubic (FCC) metals. Consider the unique deformation mechanisms of hexagonal close-packed (HCP) metals, the microstructure and mechanical behavior of HCP-based multilayered nanofilms are of particular interest in this work while the typical HCP-based multilayer system, magnesium (Mg)/titanium (Ti), is primarily investigated.

Mg and Ti layers, with equal individual layer thickness ranging from 2.5 nm to 200 nm, were alternately deposited onto a single crystal silicon substrate via magnetron sputtering to form multilayered Mg/Ti nanofilms. The as-deposited films exhibit a strong texture along Mg (0002) and Ti (0002) with preference for an epitaxial growth pattern, as characterized by X-ray diffraction (XRD) and transmission electron microscopy (TEM). Two primary orientation relationships between Mg and Ti have been identified, depending on the length scale of *h*. Both instrumented nanoindentation and microcompression experiments were performed to study the effects of individual layer thickness on the hardness/strength and strain rate sensitivity in Mg/Ti multilayers. The strength of Mg/Ti multilayered nanofilms was found to be generally increasing as the individual layer

thickness is decreased, eventually reaching the peak value of ~1.56 GPa at the smallest *h*. The dislocation pile-up based Hall-Petch law can be used to interpret the increase in strength at relatively large layer thickness (>50 nm), while the confined layer slip model provides a better explanation for the relationship between strength and layer thickness at smaller layer thickness. The flow strength measured from microcompression is much higher than the nanoindentation derived value when *h* decreases to several nanometers, which can be explained by the vanishing Schmid factor under uni-axial compression.

As a critical criterion for industrial applications, the thermal stability of Mg/Ti multilayered nanofilms was also evaluated by examining the microstructure and hardness after annealing. The multilayers with $h \geq 5$ nm possess excellent capabilities in maintaining the lamellar morphology and high strength up to 200 °C. However, the h=2.5 nm Mg/Ti multilayered nanofilms following the annealing at 200 °C for 2 h exhibit a drop in hardness to ~3.3 GPa, which is intimately related to the morphological changes at elevated temperatures.

Preliminary experimental results on Mg/Zr multilayer nanofilms show trend in mechanical properties similar to those of the Mg/Ti nanofilms as a function of individual layer thickness. Further investigation is needed to come up with a more complete understanding of this system.

DEDICATION

This dissertation is dedicated to my dear Dad, Mom and Grandma.

ACKNOWLEDGMENTS

I am very grateful to Dr. Qiuming Wei for advising me all through my PhD study. I deeply appreciate the valuable suggestions from my committee members, Dr. Ronald Smelser, Dr. Aixi Zhou, Dr. Haitao Zhang and Dr. Jing Zhou. I would like to thank Dr. Sergey Yarmolenko and Dr. Ruben Kotoka at NC A&T State University who helped me prepare the multilayer films and perform X-ray related experiments. Particular thanks are due to Dr. Jonathan Ligda and Dr. Brian Schuster in Army Research Laboratory (ARL) for fabricating the TEM samples and micropillars for microcompression. I also acknowledge the favors that Dr. Thomas Koch and Franklin Green did for me by setting up the heating furnace equipped with flowing Argon gas. Appreciations are expressed to the Graduate and Professional Student Government (GPSG) at UNC Charlotte and China Scholarship Council (CSC) for financial supports to my study. Without the encouragements and supports from my family members, this dissertation would not have been possible. “Be strong” is what my parents always tell me, and what I appreciate the most.

TABLE OF CONTENTS

LIST OF TABLES

LIST OF FIGURES

NOMENCLATURE

σ	normal stress
τ	shear stress
h	individual layer thickness
μ	shear modulus
E	Young's modulus
ν	Poisson's ratio
λ	wavelength
b	magnitude of Burgers vector
C	elastic constant
ζ	wavelength of applied X-ray
h_{cr}	the critical layer thickness for misfit dislocation formation
σ_i	nanoindentation-measured flow strength
σ_m	microcompression-measured flow strength
Λ	bilayer period
m	strain rate sensitivity
V^*	activation volume
s	distance between adjacent misfit dislocations
ξ	misfit strain
γ_{gb}	grain boundary energy
γ_{int}	interface energy

LIST OF ABBREVIATIONS

BCC	body-centered cubic
CLS	confined layer slip
CVD	chemical vapor deposition
DP	diffraction pattern
DSC	differential scanning calorimetry
FCC	face-centered cubic
FFT	fast Fourier transformation
GB	grain boundary
HCP	hexagonal closed-packed
HRTEM	high resolution transmission electron microscope/microscopy
MD	molecular dynamics
OR	orientation relationship
PVD	physical vapor deposition
SEM	scanning electron microscope/microscopy
SRS	stain rate sensitivity
TBC	thermal barrier coating
TEM	transmission electron microscope/microscopy
XRD	x-ray diffraction

CHAPTER 1: INTRODUCTION

1.1 An Overview of Multilayered Composites

With ever increasing demands for exceptional performance in a variety of structural and functional applications, researchers maintain an interest in and enthusiasm for designing unprecedented materials. Due to the intrinsic physical limitations of most monolithic materials such as high density, low strength, ductility and melting point, poor corrosion resistance or other undesirable properties for practical use, efforts are largely devoted to fabricating composites made up of different materials with specific structures [1], one of which is a multilayer structure.

A multilayered composite can be briefly defined as a material composed of alternating layers of two or more different constituents, naturally or artificially. A typical example of multilayered composites that exist in nature is nacre, the inner part of mollusk shells. Figure 1.1(a) is a microscopic image displaying the microstructure of nacre, where the aragonite plates (~200—900 nm thick) are well arranged in a lamellar pattern and separated by fine biopolymer layers (~10—50 nm thick) [2]. The mechanical properties of aragonite which accounts for 95% of nacre by volume are analogous to ceramics, hard and brittle. However, nacre exhibits impressive fracture toughness and damage-tolerant capability in various mechanical tests, despite the chemical predominance of the brittle constituent [3-5]. The deformation mechanisms responsible for this phenomenon have been widely explored. Mechanisms such as aragonite platelet sliding, effective adhesion

from the organic components, interfacial blocking of the nano-asperities at interfaces, and others [6, 7] have been proposed. As expected, all these mechanisms are linked to the inherent lamellar microstructure (interface) of nacre. A three-dimensional (3D) schematic diagram was devised and shown in Figure 1.1(b) to explicitly illustrate how the constituents in nacre are linked together, aiming to balance the mutual conflict between strength and toughness [8].

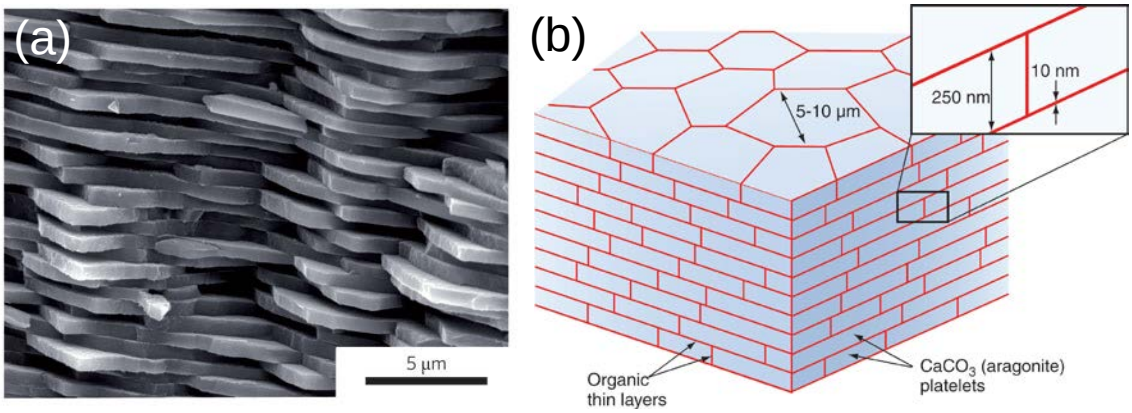

Figure 1.1: The microstructure of nacre illustrated by (a) a scanning electron microscope (SEM) image [2] and (b) a three-dimensional (3D) schematic diagram [8].

Directly inspired by the lamellar architectural configuration which results in the extraordinary mechanical behavior of nacre, numerous multilayered composites have been artificially synthesized over the past few decades. For instance, a rapid and efficient self-assembly routine to prepare organic-inorganic nanolaminated coatings that mimic nacre was proposed by Sellinger, et al. [9]. Waraich and coworkers successfully reproduced the ordered layer structure by assembling pre-synthesized α-zirconium hydrogenphosphate hydrate (ZrP) platelets and organic chitosan via a layer-by-layer deposition method [10].

Interestingly, most synthetic multilayered composites exhibit strength levels higher than their components in bulk, especially when the individual layers have a micrometer or

nanometer size scale. As reported by Misra et al., the nanoindentation measured strength of a sputter-deposited Cu/Nb nanolayered composite is ~2.6 GPa with an individual layer thickness of 1.0 nm, compared with 344 MPa of copper (cold drawn) and 585 MPa of niobium (wrought) in bulk forms [11, 12]. The enhanced strength were also found in nanocrystalline (nc)-TiN/amorphous (a)-Si_3N_4, Al/Cu, amorphous ZnCuTi/PdCuSi, and many other heterostructural multilayer systems [13-15]. In addition, layering with ductile phases (metals) has been proved to be an effective approach in toughening ceramics and intermetallics. A work from Launey et al. indicates that the fracture toughness of Al_2O_3/Al-Si (ceramic/metal) laminates could reach $40\ \mathrm{MPa}\cdot\sqrt{\mathrm{m}}$ while maintaining the same order of tensile strength as pure Al_2O_3, ~300 MPa [16]. Through the creation of a large crack bridging zone or introducing debondings along the interface in response to the crack growth, these intentionally built-up lamellar structures are able to improve the toughness and ductility of monolithic brittle materials, which could hardly be achieved by other processing methods.

From the experimental data provided above, it is pretty straightforward that the strength or toughness of the resultant multilayer system is not simply a numerical summation of bulk components as described by “the rule of mixture”. Novel properties, not merely in mechanical but also in optical, magnetic and electrical aspects, can be expected on multilayered composites. The most renowned example related to this is perhaps the “superlattice”, which was first developed by Leo Esaki and Raphael Tsu in 1970 [17]. In a superlattice structure, two superconductor materials are layered alternately on each other. The periodic variation of compositions works with the relatively short period (on the order of 100 Å), eventually leading to the electrical structure modifications from

the original states. The superlattice has such a significant meaning in the research community that almost all the multilayered composites built at nanoscale bear its name. A study reflecting the amazing effects of lamellar structure on the magnetic characteristics is that from Robinson et al. whose simulation results suggest that a multilayered composite composed of two antiferromagnetic minerals (haematite and ilmenite) would be able to show macroscopic magnetic properties [18].

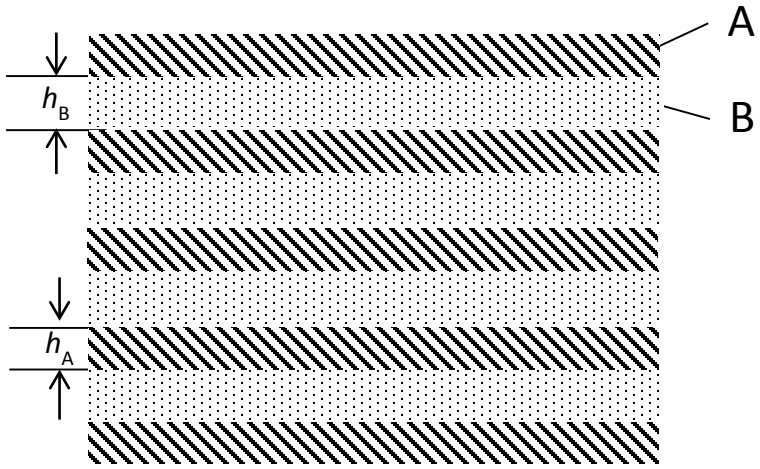

Figure 1.2: A two-dimensional (2D) schematic diagram illustrating the essential parameters involved in the design of multilayered composites. h_A and h_B designate the individual layer thickness of constituent A and B, respectively.

A common idea about the unique properties of multilayered composites differing from their constituents in bulk form is that, a great deal of interfacial area has been introduced into the materials. The importance of interface in designing multilayered composites has been widely recognized. From the mechanical viewpoint, the lamellar interface within a multilayered composite act as obstacles in impeding the motion of gliding dislocations, which consequently makes it stronger. To better illustrate the essential

parameters associated with the layer interface that could be tailored purposefully to meet particular performance requirements, the basic structure of multilayered composites has been extracted and depicted in Figure 1.2.

Primarily, the characteristics of interfaces are mainly determined by the materials on both sides of it (labeled as “A” and “B” in the schematic diagram). In the case of a multilayered composite made of miscible elements (e.g. Cu/Ni [11, 19]), the interface may consist of a mixture of laminate constituents resulting from their mutual diffusion. Therefore, it is extremely difficult to predict the width, potential artifacts and other parameters of the interface, since all of them are sensitive to the processing conditions such as temperature and pressure. On the other side, the interface of a multilayered composite constructed with immiscible layers is no less complex, as exemplified by the terminology of “coherency” which refers to the degree of lattice matching between adjacent layer materials.

Moreover, to what degree the interface influences the overall performance of a specific multilayered composite depends on the volume fraction of the interface with in the composite. Owing to the fact that the interfacial area is inversely proportional to the thickness of individual layers, the volume fraction of the interface in the multilayer composite can be tuned through the variation of layer thicknesses (indicated by h_A and h_B in Figure 1.2). Following similar working principles as grain boundaries, higher yield strengths could be obtained in the multilayer composites with a larger fraction of interfaces, or in other words, thinner layers. A number of investigations have verified that the dependence of strength on the layer thickness obeys the Hall-Petch relation when the layer

thickness is above submicron level [20-23]. We will revisit these geometrical and chemical concerns in the following section but in the context of metallic multilayered nanofilms.

Generally speaking, it is the tremendously wide possibility of combination of layer components and thicknesses that generates the diverse behavior of multilayered composites. Lloyd and Molina vividly described the multilayers as a palette for scientists, providing an ideal platform to give full play of our imaginations and explore innovative materials [24].

The outstanding physical and chemical properties of multilayered composites enable them to be one of the most promising candidates accessible to the industry. In what follows, we will give several specific examples of the engineering applications of multilayers.

The X-ray mirror is among the first applications of artificial multilayers which dates back to 1970s when Barbee and his colleagues at Stanford University developed a precise technique to control the layer thickness with accuracy of 5 Å during deposition [25]. Taking advantage of the high density of interface between layers, a multilayer X-ray mirror is able to yield a greater reflectivity in comparison with a monolayer mirror. Nowadays, multilayered films become a vital part in many Extreme Ultra-violet (EUV) and soft X-ray optical systems that essentially aids the fast growth of X-ray optics. A wide variety of multilayer systems have been exploited with respect to working in different wavelength (λ) regions, including Co/C and CoCr/C multilayer mirrors at λ=6 nm [26], Mo/Si multilayer mirror at λ=14 nm [27], SiC/Mg multilayer mirror at λ=30 nm (NTT Advanced Technology Corporation) [28] and so on. These synthetic multilayer mirrors perform powerfully in lights focusing properties with small wavelengths, not only in X-ray microscopy but also in X-ray astronomy. The famous NuSTAR space telescope, which presents us with

enormous high-resolution images of the Sun and planets, is equipped with plenty of mirrors made up of W/Si or Pt/SiC layer pairs. Figure 1.3 is a reference X-ray mirror fabricated by the Center for X-ray Optics (CXRO).

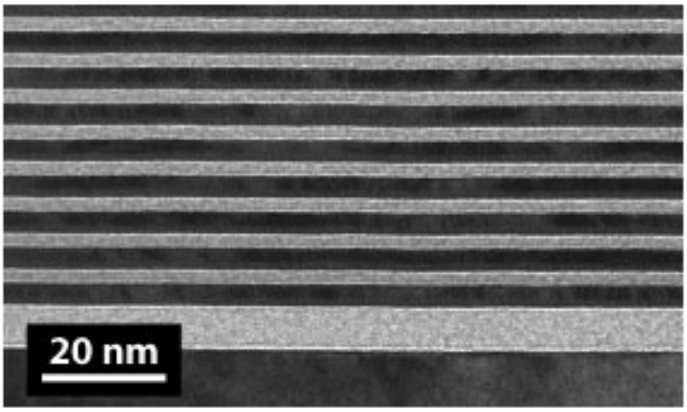

Figure 1.3: A reference X-ray mirror fabricated by the Center for X-ray Optics (CXRO).

Hard and super-hard nanolayered materials, such as nc-TiN/a-SiN_X (SHM Ltd., PLATIT AG [29]) and $Ti_{0.8}Si_{0.2}N/Ti_{0.5}Al_{0.5}N$ (Hitachi Tool Eng. Ltd.), have been commercially used as protective coatings of machining tools. A series of experimental works carried out by Veprek demonstrate the hardness of artificial nc-TiN/a-SiN_X multilayers is over 50 GPa, approaching or even surpassing that of intrinsically hard materials such as diamond and cubic boron nitride [13, 30]. In Figure 1.4(a), the superiority of using an nc-TiN/a-SiN_X layered material coating in prolonging the lifetime of drills is clearly seen, owing to its higher hardness and oxidation resistance, lower thermal conductivity as well as smoother surface. The tools coated with superhard multilayer films (comprised of silicon nitride and transition metal nitride nanocrystalline layers) perform very well in machining steels, cast iron, Inconel and even the extremely stiff nickel-based superalloys [31, 32]. Figure 1.4(b) presents the lamellar microstructure of a deposited nc-

TiN/a-SiN_X nanocomposites, in which the optimum modulation period and maximum hardness has been achieved. It is very important to note that the hardness of nc-TiN/a-SiN_X multilayered coating could be further improved by decreasing the content of impurities or promoting the phase segregation in the deposition process.

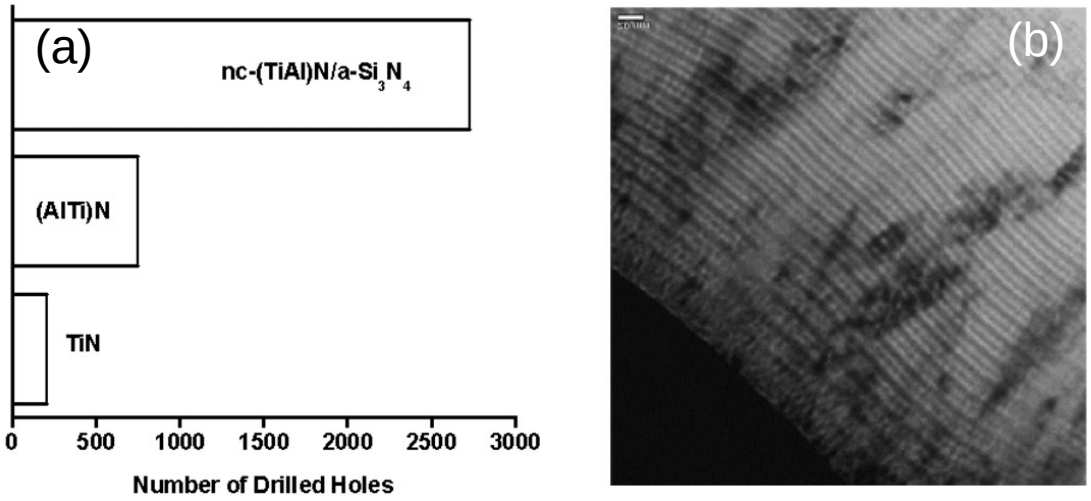

Figure 1.4: The excellent performance of multilayered superhard coatings. (a) A comparison of the lifetime of drills (diameter 5 mm, made of cemented carbide) coated with different coatings. (b) The microstructure of a nano-layered superhard coatings with a high hardness and high resistance against brittle fracture [32].

Another engineering application of multilayered composites is thermal barrier coatings (TBCs). In an early project collaborated among Lawrence Livermore National Laboratory, Pratt & Whitney and Rohr Inc., high-performance multilayered coatings were developed, increasing the working temperature of aircraft engines by 10 to 38 °C and thereby allowing higher thrust [33]. The very TBCs that have gained the most commercial attention have such a characteristic microstructure: a bond-coat (NiCrAlY or NiCoCrAlY alloy, ~100 μm in thickness) is first deposited onto the superalloy, followed by a ~10 μm thick thermally grown oxide (TGO), and is finally covered with a ceramic top-on coat

(Y_2O_3-stabilized ZrO_2 (YSZ), 100-400 μm in thickness). Composed of metallic and ceramic layers, these TBC multilayers are beneficial to insulate the turbine from the hot gas streams and offer effective protections for the industrial gas-turbine engines used in aircraft and marine propulsion [34-36]. Moreover, the layer interface has been deemed as an efficient media to impede the heat flow, which in turn reduces the thermal conductivity of TBCs. Recently a few new superlattices with ultra-low thermal conductivity such as W/Al_2O_3 nanolaminates are synthesized, which exhibit huge potentials in replacing conventional 7YSZ as TBCs [37-39]. In this sense, we can expect more efficient TBCs owing to the use of multilayered structures.

Multilayered thin films are also becoming more popular in the field of micro-electronics. Giant magneto-resistance (GMR), which brought Albert Fert and Peter Grünberg the 2007 Nobel Prize in Physics, has been used in the hard disk drives, biosensors, oscillator detectors and other electronic devices to read data. By changing the aligning direction of adjacent ferromagnetic and non-magnetic conductive layers, the GMR is endowed with varying electronic resistance, low for parallel alignment while high for antiparallel alignment [40]. The appearance of GMR is undoubtedly a milestone in the history of electronic data storage, significantly increasing the data reading speed and contributing to many commercial areas.

To summarize, this section presents a brief review of multilayered composites, including the concept, properties, structural characteristics, designing concerns and major applications. Multilayer composites are an inherently broad subject, ranging from organic to inorganic, large size to small size, stable to unstable, and so on. Hence, it is extremely difficult to cover all of them in such a short description. The in-situ lamellar composites

(e.g. Nb_{SS}/Nb_5Si_3 [41], Ni/Ni_3Ti [42] multilayers) and macroscopic sandwiched materials, which are also topics of interest in multilayered composite research, are not the focus here. Our discussion, specifically in regard to industrial applications, is concentrated on the metallic multilayers consisting of small size dimensions, since the emphasis of this thesis is on multilayered nanofilms. It is worth noting, that although the size regime of interest is at the micro-scale or nanoscale, the extensive applications of multilayer composites in optical, mechanical, thermal and magnetic areas are also witnessed. In the next section we will present more details about the chemical and geometrical concerns, synthesis methods and deformation mechanisms of multilayered nanofilms, a particular branch of multilayered composites, based on available experimental data.

1.2 Fundamentals of Multilayered Nanofilms

The importance of lamellar structure in industrial developments has been recently recognized via the novel properties arising from multilayered nanofilms—the multilayered composites with one dimension decreased to micrometer or even nanometer scale. Increasing attention has been given to them in terms of theoretical and experimental studies. Prior to considering the performance improvements for a given multilayered nanofilm, the focus of most studies in this area, it is necessary to know which parameters associated with multilayer synthesis can be artificially altered and how these changes can be made. The first question will be addressed in the first section discussing the chemical and geometrical concerns with respect to multilayered nanofilms, whereas the answer to the second question will be found in the following part regarding common processing techniques. Finally, we will discuss the general mechanical performance and deformation mechanisms of multilayer nanofilms.

1.2.1 Chemical and Geometric Concerns

As previously mentioned, multilayered nanofilms belong to the family of "multilayer composites", and thus bearing the fundamental characteristics depicted in its definition — alternating layers of two or more different materials. Nevertheless, the term "nanofilm", which normally refers to a two-dimensionally formed thin film with the thickness no more than one micron, imposes extra geometrical restrictions that differentiate them from other multilayered composites.

Retrospective to our descriptions of Figure 1.2, it is quite straightforward that the chemical composition and length scale of constituent layers are the major controllable parameters of multilayered nanofilms. Akin to conventional composites, the primary concern about the design of multilayered nanofilms, is which elements or compounds should be selected as nanolaminates. In fact, any solid material, and possibly even some liquid materials, as long as they could be manufactured into laminates, are qualified to be components. Meanwhile, advances in multilayer preparation methods foster this kind of diversity by enabling a greater variety of raw materials to be fabricated into laminates.

However, due to the mechanical integrity and thermal stability that are usually required for practical applications, careful attention needs to be paid to the selections of constituents for multilayered nanofilms. For example, the constituents of a multilayered coating designed for corrosive environment necessarily possess a high level of corrosion resistance in order to work properly. It is also reasonable that materials with relatively poor thermal stability are unsuitable to make up multilayers used at elevated temperature. In addition to the properties of each individual constituent on its own, moderate compatibility among constituents is another criterion that must be considered during the design of

multilayered nanofilms. In most cases, mutual reactions of constituents are undesirable, except where the reaction products act as a final constituent of the film (e.g. The amorphization reaction between Cu and Zr layers was intentionally carried out to form the crystalline Cu—amorphous Cu/Zr nanolaminates in Wang's work [43]). Extra efforts might be demanded to tackle the problems emerging in the synthesis process or inadequacies of the eventual performance caused by the incompatibilities.

The significance of choosing appropriate constituents is also reflected in the characteristics of layer interface. As for multilayered nanofilms, the interface can be divided into three categories according to the extent of lattice matching between adjacent layers: coherent interface, semi-coherent interface and incoherent interface. For a coherent interface, the two crystals match perfectly in the interface plane and the lattices are continuous from one layer to another. The semicoherent interface is usually defined as the interface in which the disregistry is periodically taken up by misfit dislocations. When the interface plane has a very different atomic configuration in the two adjacent phases and there is no possibility of good matching across the interface, the interface can be taken as incoherent. It is argued that the misfit dislocations at phase interface, resulting from the lattice mismatch between adjoining layers or that between the first deposited layer and the substrate upon which the film is deposited, can affect the mechanical behavior of the whole film significantly. For all the reasons above, the choice of layer components for a multilayered nanofilm greatly depends on the requirements of its future applications and should be carefully treated.

The thickness of each layer in the nanofilm is another parameter that could be manipulated during preparation. Multilayered nanofilms are well-known for their high

area-to-volume ratio which can be tailored by varying the individual layer thickness. For optical multilayer films, the individual layer thickness is so critical that a small deviation would bring about a large change in the reflectivity, interference and diffraction. Furthermore, the dependence of yield strength on the layer thickness of multilayer films was early revealed in Koehler's attempts to design a strong solid [44]. Since then, thinning layers has been used as an efficient path to enhance the strength of materials composed of alternating layers. As suggested by Zhang et al., it is not only the absolute value of the layer thickness that affect the performance of multilayered nanofilms, layer thickness (modulation) ratio η of constituents also matters. They fabricated Cu/X (X=Nb, Zr) nanostructured multilayered films (NMF) with various modulation ratios ranging from 0.11 to 3.0 on which the uniaxial tensile tests showed the remarkable dependence of yield strength on η [45].

1.2.2 Synthesis and Fabrication Techniques

In the past decades a number of manufacturing techniques have been developed to synthesize multilayered nanofilms, among which the physical/chemical vapor deposition (PVD/CVD), electro-deposition and accumulative roll bonding (ARB) are frequently used to fabricate the metallic multilayered nanofilms [46].

1.2.2.1 Physical/chemical Vapor Deposition (PVD/CVD)

When preparing a thin film, both physical and chemical vapor deposition techniques utilize the evaporated atoms or molecules of metals and other materials in a vacuum, and subsequently adhere them to the substrate. Unlike CVDs in which chemical reactions between the gaseous-phase raw materials and substrate surfaces always occur, PVDs are much easier to monitor and generally consist of three major steps: (i) removal of

original materials from the source; (ii) transport of the excited atoms to the substrate; (iii) film growth. For earlier developed PVDs, the evaporated atoms were ejected from the original source by heating (thermal evaporation). However, modern PVDs generally refer to the sputtering deposition techniques where the source is bombarded by energetic particles bombardment such as electrons, ions and photons [47, 48].

A significant advancement that has been made in the area of sputtering methods is undoubtedly the appearance of magnetron sputtering, which uses the applied magnetic field to trap as many as electrons in the vicinity of the source target, therefore greatly increasing the opportunity of ionizing electron-atoms collision and in turn the deposition rates [49, 50]. According to the working principles of magnetron sputtering technique, we can see that this method is competent in depositing materials with high melting point. Compared with conventional evaporated films, magnetron-sputtered films possess many advantages such as a better adhesion of deposited materials onto the substrate, higher compatibility with reactive gases and closer composition with the target source. Because of all these merits, the HCP-based multilayered nanofilms to be investigated in this thesis are prepared by magnetron sputtering. More details about this processing method will be presented in the coming chapter, specific to the instrument that we used.

1.2.2.2 Electrodeposition

Electrodeposition, also known as electroplating, is a process that uses electrical current to deposit dissolved metals or alloys on an electrode with the electrolyte, following the passage of current. The first electrodeposited multilayer film was prepared in 1921 by Blum who deposited copper and nickel alternately from two different electrodes [51]. Although the resulting Cu/Ni multilayer had a relatively coarse repeat length of ~24 μm at

that time, the developments over the past century on the electrodeposition techniques have enabled the accurate control of nanoscale layers. So far, this deposition method has been extensively employed to make protective or decorative coatings for magnetic tape drives, hard disk drives, semiconductor flash memory, random-access memory and other components essential to this information era [52]. It is worth noting that most GMR multilayered nanofilms are fabricated by means of electrodeposition [53-55]. Apart from the favorable magnetic properties, electrodeposited multilayer films also exhibit impressive mechanical properties, e.g. the tensile strength of an electrodeposited multilayer with nominal composition of 10%-Cu/90%-Ni is roughly 1.3 GPa when the thickness of Cu laminates is decreased below 0.4 μm [56].

Despite the comparatively low cost and operating temperature of electrodeposition, potential displacement reactions between deposited materials always act as the bottlenecks preventing the electrodeposition technique from producing a large variety of multilayered nanofilms. A lack of experimental data to illustrate which materials can be electrodeposited further harms the relevant applications. We believe electrodeposition is a promising method to prepare metallic multilayered nanofilms, but only after more research efforts are devoted can its advantages be fully exploited.

1.2.2.3 Accumulative Roll Bonding (ARB)

As compared with the aforementioned processing methods of multilayered nanofilms, accumulative roll bonding (ARB) is a new technique which was invented by Saito et al. in 1999, originally aiming to fabricate ultrafine grained metallic materials via severe plastic deformation [57]. Figure 1.5 schematically represents the standard procedures involved in ARB: stacking, roll bonding, cutting, restacking and rerolling,

repeated multiple times until the desired layer thickness is achieved. During the whole process, the step of rolling has dual functions of creating extremely large plastic strain and increasing bonding strength between constituent layers. Previous studies on the nanoscale multilayers prepared by such a mechanical alloying route indicate an achievement of extraordinary strength, good ductility and exceptional thermal stability [58-61]. The profound impact of the ARB method in the regime of multilayer synthesis lies in the fact that it provides the possibility to make multilayered nanocomposites in bulk form.

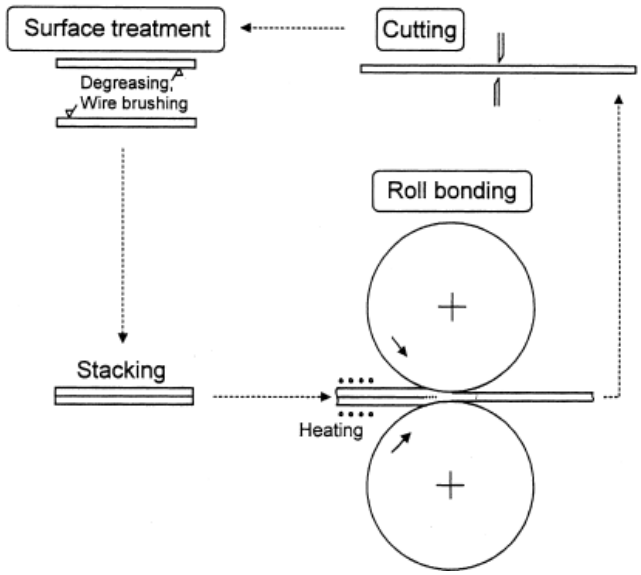

Figure 1.5: Diagrammatic representations of the accumulative roll-bonding (ARB) process [57].

The morphology of ARB metallic multilayered nanofilms, characterized with flat and sharp phase interfaces, has been proven to play an even more important role in the improvement of mechanical properties than bi-metal combination [60]. The TEM observations of ARB Cu/Nb multilayers made by Han [62] and Zhang [58, 63] suggest that

deformation twins emitted at interfaces under special crystallographic conditions directly are directly linked to the involving deformation or strengthening behavior.

In summary, multilayered nanofilms can be fabricated via different approaches, either in the form of bottom-up process such as PVD and electrodeposition, or top-down process such as ARB, or both [64], following the traditional category of manufacturing methods for nanomaterials. The microstructure, crystallographic texture, mechanical properties and thermal stability of resulting multilayer materials largely depend on the synthesis method that has been applied. To our knowledge, the three techniques introduced here are typical and are currently the prevailing ones to prepare multilayered nanofilms, and yet there are still several other synthesis methods that have not been described due to the limited references.

1.2.3 Mechanical Behavior and Strengthening Mechanisms

1.2.3.1 Mechanical Behavior

Current research on multilayered nanofilms has become multidisciplinary, encompassing physics, chemistry, optics and mechanics. Although most attention has been paid to the improvement of their optical and magnetic properties, as driven by the consumer market; mechanical performance, as a crucial prerequisite for the practical applications of thin films, must be considered carefully as well. Similar to the bulk materials which are required to display sufficient mechanical robustness, multilayered nanofilms ought to withstand a certain level of impact and exhibit enough resistance against fatal failures in practice. Thereby a full understanding of the fundamental deformation mechanisms is critical in designing multilayered nanofilms of higher quality.

This section mainly consists of two parts. The first part is a quick review of the mechanical properties of various nanostructured multilayer systems, including the hardness, yield strength, flow stress, fracture toughness, ductility, fatigue and creep responses, etc. The second part describes the major deformation mechanisms involved in multilayered nanofilms on the basis of dislocations, twins and shear bandings.

The extremely high strength of multilayered composites started to gain recognition when Koehler proposed the design of strong solids by laying materials with high and low elastic constants alternately, under the assumption that the layers were thin enough to constrain the operation of Frank Read source [44]. He inferred that the resolved shear stress of a metallic multilayer with such a structure could theoretically reach the order of $G_{low}/100$, where G_{low} is the shear modulus of the softer constituent. Afterward, a number of experiments were devised to verify this strengthening mechanism. Recent developments in the research of multilayered nanocomposites, however, indicate they are capable of exhibiting an even higher strength than that predicted by Koehler theory. For example, the measured nano-hardness of a Cu/Ni multilayer deposited by means of electron beam evaporation is up to 6.8 GPa while the theoretically predicted peak hardness is only 4.0 GPa [65]. Table 1 summarizes recorded tensile/compressive strength or hardness of a variety of metallic multilayer systems. We can easily figure out that, the majority of these metallic multilayered nanofilms listed in Table 1 exhibit a strength of several GPa at room temperature, approaching 1/3 to 1/2 of the theoretical limit of strength ($E/30$, E is the elastic modulus) and obviously outperforming most nanocrystalline materials, if not all. What is more, the prominent strength enhancement arising from layering two metallic components alternately implies that it could be a promising path to make stronger materials. The

dominating mechanisms behind this phenomenon that have greatly intrigued people will be discussed later.

For metallic multilayered nanofilms, the mechanical properties are usually evaluated in terms of nano-hardness because it is comparatively easy to perform nanoindentation tests on the specimens with a size dimension at or below micrometer scale. Meanwhile, increasing efforts are being made to perform conventional mechanical tests such as tensile and compression experiments on them. Wang and his coworkers have conducted uniaxial tensile tests on Cu/Cu-Zr glass nano-laminate specimens with a total thickness of 30-110 μm, gauge width of 6 mm and length of 3 mm [43]. Such miniature tensile tests have been carried out on other multilayer specimens by Josell [66] and Zhang [45]. On the other hand, microcompression tests have also been delicately devised to study the stress-strain response and plastic deformation behavior of multilayered nanofilms such as Cu/Nb (Mara, et al. [67]), Al/Nb (Kim, et al. [68]) and Al/Al_3Sc (Han, et al. [69]).

Although the experimental data in Table 1 was mainly collected from mechanical tests operated at room temperature, Mara et al. investigated the evolution of mechanical properties of polycrystalline 75 nm Cu/75 nm Nb multilayer thin films at elevated temperatures and concluded that the films were able to retain a high level of strength, ~450 MPa up to 500 °C [70].

Table 1: The strength and hardness of various metallic multilayer systems.

Multilayer	Synthesis technique	Layer thickness (total thickness)	Mechanical properties (peak value)	Reference
Cu/Nb	dc magnetron sputtering	0.8-600 nm (1 μm);	Nanoindentation hardness ~7.1 GPa	[11, 71]
		75 nm (15 μm);	Tensile strength (500 ˚C) ~450 MPa	[70]
		5-125 nm (0.5 μm);	Tensile strength ~1.3 GPa	[45]
		5 nm	Compressive strength ~2.4 GPa	[67]
Cu/Ni	dc magnetron sputtering	25-1000 nm	Nanoindentation hardness ~3.9 GPa	[11]
	e-beam evaporation	2-26 nm (0.5 μm)	Nanoindentation hardness ~6.8 GPa	[65]
Cu/V	dc magnetron sputtering	1-200 nm (1.6 μm)	Hardness ~5.1 GPa	[72]
Cu/W	e-beam evaporation	2-30 nm (0.4 μm)	Nanoindentation hardness ~8.9 GPa	[73]
Cu/Ag	e-beam evaporation	5-200 nm (1 μm)	Nanoindentation hardness ~4.8 GPa	[74]
		1.5 nm-1.5 μm (3 μm)	Yield stress ~0.65 GPa	[75]
Cu/Cr	dc sputtering	20-1000 nm	Nanoindentation hardness ~7.0 GPa	[11]
Cu/Zr	dc magnetron sputtering	5-125 nm (1 μm)	Tensile strength ~1.1 GPa	[45]
Cu/330Steel	dc sputtering	1-500 nm (2 μm)	Nanoindentation hardness ~5.1GPa	[76]
Cu/304 SS	dc magnetron sputtering	1-500 nm (2 μm)	Nanoindentation hardness ~5.5 GPa	[77]
Ag/Fe	e-beam evaporation	2-30 nm (0.5 μm)	Nanoindentation hardness ~5.5 GPa	[78]
Ag/Ni	dc magnetron sputtering	1-200 (1-4 μm)	Nanoindentation hardness ~6.2 GPa	[79]
Al/Nb	dc magnetron sputtering	1-200 nm (1.6 μm)	Hardness ~4.8 GPa	[72]
		5 nm	Compressive strength ~1.7 GPa	[68]
Mg/Nb	dc magnetron sputtering	2.5-200 nm (1.5-5 μm)	Nanoindentation hardness ~2.5 GPa	[80]
Al/Al_3Sc	dc magnetron sputtering	6-100 nm (1 μm)	Nanoindentation hardness ~3.0 GPa	[81]
			Compressive strength ~1.7 GPa	[69]

Note:* Without the indication of testing temperature, the experiments were performed at room temperature. ** The compressive strength was measured in microcompression test.

As we know, for most materials, the increase of strength is usually accompanied with the sacrifice of toughness. Following the general concept to strengthen crystalline materials by suppressing the slip activities of dislocations, the huge amount of interface in the metallic multilayered nanofilms indeed act efficiently in impeding the dislocation motions and improving flow stress, but simultaneously impose negative effects on the inherent resistances against crack propagation and fracture. Consequently, in contrast to the numerous encouraging records of improved strength and hardness, little experimental data is available regarding the fracture toughness or ductility of nanoscale metallic multilayers. The majority of the relevant information was only extracted from experiments where the primary objective was to determine the tensile strength. For example, the tensile stress-strain plots in Josell's work indicate that the elongation of the 25 nm Al/15 nm Ti multilayer sample was no more than 2% [66]. A similar result was obtained by Zhang et al. on Cu/Zr multilayers whose critical strain corresponding to ductility fell into the range of 2-3%. Based on batches of tensile tests, Mara et al. suggested that the ductility of the freestanding Cu/Nb multilayer (~65 nm in layer thickness) held a gradual increasing trend with the increase of temperature but the plastic strain to fracture measured at room temperature was still merely 5% [82]. All such experimental evidence demonstrates that metallic multilayered nanofilms are likely to be in essential poverty of ductility [45]. Worth noting, though, is a recent breakthrough in the deformability of nanolaminates was that achieved in a nanocrystalline-amorphous multilayer system (35 nm Cu/ 5nm Cu-Zr metallic glass) with ~1.1 GPa flow stress and ~13.8% tensile elongation which is encouraging for the future of the engineering plasticity in multilayer nanocomposites [43].

There exist sporadic published works focusing on the fracture processes of metallic multilayers, particularly the dependence of fracture behavior on the length scale of constituent layers [83, 84]. In a previous study, Li and Zhang designed three-point bending experiments on an Instron Electroplus E1000 testing machine to investigate the localized fracture behavior of miscible Cu/Au and immiscible Cu/Cr multilayers [84]. As for the Cu/Au multilayer system, they observed intra-granular brittle shear fracture in the h=25 nm sample, inter-granular brittle shear fracture in the h=50 nm sample and ductile shear fracture in the h=100 nm and 250 nm samples. However, Cu/Cr multilayers invariably showed brittle normal fracture mode, independent of layer thickness. The different plastic deformation and fracture behavior between these two kinds of multilayered nanofilms was attributed to several factors: crystallographic orientation relationship between constituents, constraints of layer thickness, layer interface on dislocation motions as well as the columnar grain boundaries. Zhang and his co-workers further confirmed that the length scale of individual layers could affect the fracture behavior of nanostructured multilayered films in terms of transition of facture mode from brittle opening fracture to shear facture with decreasing layer thickness, after systematically examining the fractography of tensile tested Cu/Zr and Cu/Nb multilayers. The authors emphasized that the constraints from the Cu (ductile) layers on the propagation of micro-cracks played the dominant role in the control of fracture behavior. Considering the extensive industrial applications of multilayered nanofilms for the future, their reliability and durability, which are closely related to their failure, undoubtedly worth further investigations.

Owing to the much reduced size of multilayered nanofilms, it is very difficult to conduct dynamic and cyclic loading experiments on them. A historical attempt to

experimentally measure the fatigue properties of self-supported nanoscale multilayers was made by Wang et al. [85]. They developed a high frequency fatigue testing technique named as “resonant frequency method” which utilized a bimorph piezoelectric plate-like actuator to apply excitations on the cantilever beam fabricated from the 40 nm Cu/ 40 nm Nb specimen. According to the obtained S-N curves, the Cu/Nb multilayer exhibited a fatigue limit around 450 MPa. However, the fundamental deformation mechanisms associated with the crack initiation during tension-compression cyclic loading have not been completely determined.

Creep response commonly refers to the time-dependent plastic deformation under high stresses or elevated temperatures and has been frequently observed in metallic nanoscale multilayers. The nanoindentation creep test, in which the changes of indentation depth as a function of time are tracked during the holding period, renders a direct and simple way to investigate the creep phenomena of multilayered nanofilms [65, 86]. The mechanisms correlating to the creep behavior have been widely discussed on the basis of experimentally observed varying creep rates at different scales of layer thickness but are still in dispute. For example, Kang et al. argued that for the Ag/Ni multilayer system the grain boundary deformation became dominant at bilayer thicknesses below 8 nm since they noticed the increase of creep rate as the bilayer thickness decreased [86]. Conversely, in the inspection of creep properties of another iso-structural nano-multilayer system, Cu/Ni, Zhu et al. found the creep rate decreased with decreasing periodicity until the periodicity approaches 10.5 nm, and after that it surprisingly soared up around 3.5 nm periodicity [65]. Hence they suggested that the variation of the stress exponent (ranging from 2.2 to 6.7) with decreasing modulation periodicity was ascribed to a transition of the dominating rate

from climb-controlled to eventually glide-controlled events. A temperature-involved creep study of multilayer thin film at roughly micrometer scale was presented by Shen and Suresh. Different mechanisms (e.g. high temperature or low temperature power law and dislocation glide model) were proposed to describe the creep behavior of Al/Al_2O_3 multilayers at different levels of layer thickness via the influence on the extent of stress relaxation within the layers [87].

Apart from the mechanical properties mentioned above, there is another particular topic with regard to multilayer nanocomposites— radiation damage resistance, which has been investigated with great interest recently. Rather than a mechanical property on its own, radiation damage is actually a physical issue affecting almost all the mechanical properties by inducing point defect effects on the multilayers under ion/neutron irradiations. The experimental and atomistic modeling results for Cu/Nb and Ag/Ni multilayers indicate that they have a high level of radiation damage tolerance, enabling them to be competent for future nuclear applications [88-90].

1.2.3.2 Strengthening Mechanisms of Multilayered Nanofilms

At the microscopic level the deformation of crystalline materials is primarily fulfilled by the multiplication and movement of extensively existing line defects—dislocations. This is also true for metallic multilayers. The strengthening mechanisms that improve the strength and hardness of these materials generally involve retarding or inhibiting dislocation motions. For example, the solid solution hardening works by impeding gliding dislocations with solute atoms while the strain hardening makes use of the increased dislocation density and ensuing mutual entanglements to slow down the dislocations. However, the strengthening process for a specific material is much more

complicated than what we have portrayed since various strengthening mechanisms could activate simultaneously, instead of operating separately.

Multilayered nanofilms, which have been recognized for their inherently high surface area-to-volume ratio, are predominantly strengthened by the boundary-based mechanisms. Within the multilayers, both phase interfaces and grain boundaries, are deemed as effective barriers to prevent the transmission of dislocations. The strengthening process of a multilayered nanofilm may vary with layer thickness, and accordingly, different mechanisms would play the dominant role in enhancing the strength. Figure 1.6 displays a general trend of nanoindentation measured hardness as a function of individual layer thickness h extracted from the recorded experimental data of Cu/Cr, Cu/Nb, Cu/Ni and Cu/Ag multilayer systems. In this figure, when $h \geq 50$ nm the hardness exhibits a linear relationship with $h^{-0.5}$, pointing to the Hall-Petch relation. As h decreases from a few tens nanometers to several nanometers, the increase of hardness slows down, and Orowan strengthening replaces Hall-Petch law as the controlling mechanism for the strength of multilayer films. A plateau of hardness, or even some softening, appears with the continuous decrease of h to 1-2 nm, which indicates the dislocations finally pass through the phase interface and propagate in the adjacent layer [71, 91].

The composition choice of constituent layers, which is intimately linked to the type of layer interface, can have remarkable impacts on the strength level of the resulting multilayer. In the case of a coherent interface, the coherency stress makes a significant contribution to the final strength. Whereas a semicoherent multilayer system has a certain extent of lattice mismatching, and the misfit dislocations deposited at the interface are still able to drag glide dislocations, in a manner similar to strain hardening, and thus partly

improve the strength. Again, the image stress proposed by Koehler with regard to nanoscale multilayers is another important source of strength because it arises from the disparity in dislocation energies that a moving dislocation must overcome before entering the layer with higher elastic modulus.

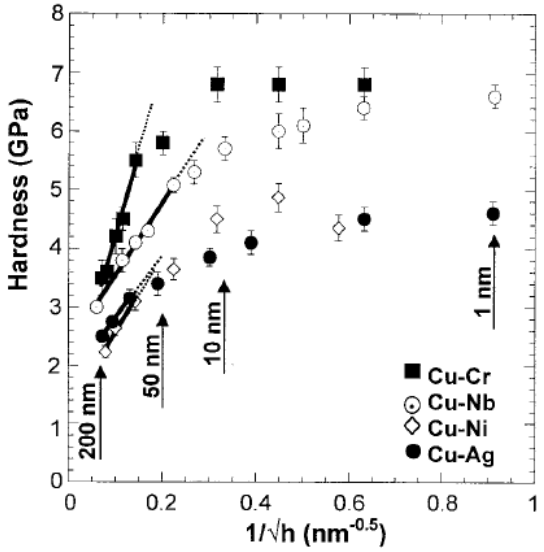

Figure 1.6: Plots of hardness as a function of $h^{-0.5}$ in several Cu-based multilayers [91].

For all of the above, it is clearly seen that the strengthening of multilayers is more complex than that of bulk materials due to the higher density of interfaces involved. To make full use of the aforementioned strengthening mechanisms and exploit the strength of multilayer thin films to a maximum, great details about them will be provided in the following sections on the basis of dislocation motions at different layer periodicity conditions. The effects of twinning on the deformation of multilayered nanofilms will be discussed separately at the end of this section.

(1) Hall-Petch relation

As the “golden rule” describing the dependence of yield stress on the grain size in polycrystalline materials, the Hall-Petch relation was early demonstrated in Hall’s publication which attempted to interpret the initial yielding of mild steel [92]. Almost at the same time, another English material scientist, Petch, claimed that the cleavage strength of polycrystals had the same tendency as yield strength with regard to grain size [93]. The Hall-Petch relation named after the two contributors can be expressed as

$$\sigma_y = \sigma_0 + kd^{-0.5} \tag{1}$$

where σ_y is the yield strength, σ_0 is the friction stress without grain boundaries and d represents the grain size. k is a constant that has usually been called the “Hall-Petch slope”.

In the past sixty years, the validity of the Hall-Petch relation in predicting the yield stress at millimeter and micrometer grain size levels has been experimentally proved. A physical explanation for this relation at the microscopic level is: the shorter the mean slip distance is, the more the dislocations pile up against the grain boundary and in turn the larger a stress concentration can be induced in the active grain [94]. Unfortunately, there has not yet been any directly experimental observation of dislocation pile-ups at boundaries. Several other models therefore have been proposed to account for the Hall-Petch effect, including grain boundaries as dislocation sources and sinks [95], geometrically necessary dislocations for plastic compatibility at the grain boundaries [96], avalanche behavior of dislocations [97], and so on.

Specific to multilayered nanofilms, the Hall-Petch relation is still applicable, most of the time with the parameter d in Equation (1) being simply replaced by the individual layer thickness h. This is possible because the spacing between layer interfaces is usually less than the spacing between grain boundaries. However, what will happen if the grain

size is comparable to the layer thickness? To answer this question, Misra et al. theoretically derived a deformation map illustrating the operative mechanisms at varying length scales, which agreed well with the experimental results of several polycrystalline metallic multilayers with different combinations of layer thickness and in-plane grain size values [20].

Although an increase of yield stress should be expected with decreasing grain size according to the Hall-Petch relation, recently more and more experimental results show its failure in predicting the strength of nanocrystalline materials [98-101]. For instance, Chokshi et al. who were the first to report the negative Hall-Petch slope during the mechanical examination of Cu and Pd nanocrystalline samples, ascribed it to the enhanced coble creep [101]. The grain boundary shearing (sliding) which can accelerate the plastic flow of nanocrystals, or even produce the superplasticity, has been proposed as another possible mechanism for the abnormal strength response [102]. Nevertheless, we should note that the breakdown of the conventional Hall-Petch relation observed in multilayered nanofilms, particularly when their layer thickness falls into the regime of several nanometers [77, 103], is not exactly the same as the “inverse Hall-Petch effect” described above. Diffusional creep behavior is likely to be a major factor resulting in the strength loss of multilayered nanofilms.

(2) Orowan strengthening (Confined Layer Slip model)

The dislocation pile-up-based Hall-Petch scaling law becomes effective only when the dislocation can be treated as a continuum, or in other words, the number of dislocations is large enough. As suggested by Anderson and Li, strong deviations from the Hall-Petch prediction may occur if there are merely one or two dislocations contained in a pile-up

because of the small layer thickness [104]. Assuming the plastic flow in fine scale lamellar structures takes place by the motion of single dislocations rather than dislocation arrays, Embury and Hirth calculated the stress required to propel the dislocation (Orowan-type loop) confined within a layer [105]. In such a confined layer slip (CLS) model, the relation between critical shear stress τ_{CLS} and individual layer thickness h is usually derived from an energetic viewpoint [106]. A typical expression of τ_{CLS} for 60˚ dislocations in Cu was derived by Misra and his co-workers [71] as

$$\tau_{\mathrm{CLS}} = \frac{\mu b}{8\pi h'}\left(\frac{4-\nu}{1-\nu}\right)\left[\ln\frac{\alpha h'}{b}\right] \tag{2}$$

where μ and ν are the shear modulus and Poisson's ratio, respectively; b is the magnitude of Burgers vector; $h = h'/\sin\varphi$ is the layer thickness measured parallel to the glide plane while φ is the angle between the glide plane and the interface; α represents the core cutoff parameter.

In contrast to the Hall-Petch relation, the CLS model presents a good fit to the trend of hardness over the range of $h \sim 5-50$ nm as shown in Figure 1.6. In practice, the calculating equation for τ_{CLS} might be slightly altered for different multilayer systems to improve the fitting (refer to the work of Philips et al. [107] and Misra et al. [91]). For convenience, the dependence of shear stress on the layer thickness depicted in CLS model is usually expressed as $\sigma = \ln h / h$. Before applying the CLS model to interpret the experimental results, it is necessary to note that the influences from the image stress and Koehler stress on the strength have been reduced to a nearly negligible level, as what had been supposed all through the derivation of Equation (2) .

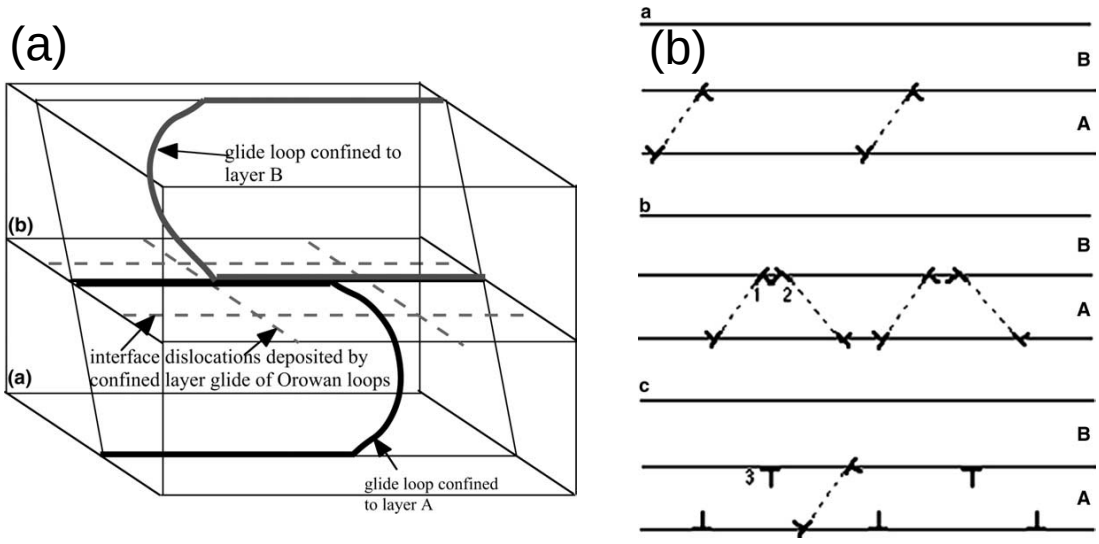

Figure 1.7: Schematic illustrations of the formation of interface dislocations in nanoscale multilayers with a (a) 3D view [108] and (b) 2D view [71].

(3) Refined CLS model

In the study of length-scale-dependent deformation behavior of Cu/Nb multilayered composites, Misra et al. found that the original CLS model significantly overestimates the flow stress at small layer thickness ($h \leq 15$ nm). Hence, he considered three refinements onto it and developed a refined CLS model which can correctly predict the strength increase when h was a few nanometers to a few tens nanometers [71]. So far this refined CLS model has been proven applicable to many other incoherent multilayer systems [84, 109] and several coherent systems [65].

According to Misra's work, the first refinement stems from the atomistic modeling by Hoagland et al., which indicated the Cu/Nb interface could shear in response to the approach of a glide dislocation and lead to its spreading within the interface plane. Thus it is inappropriate to take the parameter α in Equation (2) as unity since the dislocation core

is actually not compact. In the second refinement, the interface stress arising from the elastic deformation of the interfacial region was taken into account. When subjected a compressive loading, the existing interface stress is able to assist the applied stress during the deformation. A term of " f / h " with negative sign, where f represents the interface energy, needs to be added to Equation (2) because the experimental strength was measured by nanoindentation. At last, the resistive force resulted from the interaction between the gliding dislocation loop and the array of dislocation segments deposited on the interface was considered. Figure 1.7(a) and (b) illustrate how the interface dislocations are formed by the previous Orowan bowing loops in 3D and 2D views, respectively. In the case of a semi-coherent interface, the misfit dislocations act as a ready source for interface dislocations and would facilitate or hinder glide dislocations. With all these factors incorporated, Equation (2) is now transformed to Equation (3)

$$\sigma_{\mathrm{CLS}} = M \frac{\mu b}{8\pi h'}\left(\frac{4-\nu}{1-\nu}\right)\left[\ln\frac{\alpha h'}{b}\right] - \frac{f}{h} + \frac{\mu b}{\lambda(1-\nu)} \tag{3}$$

where the last term corresponds to the strength contribution from dislocation-dislocation interactions occurring at the interface, and λ is the spacing of the interface dislocation array.

(4) Interface boundary

When the applied stress surpassed a critical value, the glide dislocation confined within a single layer was able to cross the interface and enter into the adjacent layer. Misra et al. argued that, for an incoherent metallic multilayer, the peak strength is obtained at this point. The peak strength could be directly read out from the experimental results of nanoindentation or tensile tests (Figure 1.6). For the theoretical estimation of interface

barrier strength, Misra et al. equated it to τ^*, the shear stress needed to emit a glide dislocation on the other side of the boundary

$$\tau^* = \frac{k^2 \pi (1-\nu)}{\mu b} \tag{4}$$

where each symbol retains the same meaning as described before. The peak strength predicted by Equation (4) turns out to be surprisingly consistent with the measured one for Cu/Nb multilayered composites. It has also been suggested that the interface barrier strength of a multilayer composite is an intrinsic property, mainly determined by the interface structure and independent of the layer thickness.

The dislocation related mechanisms for multilayer strength which are operative at different length scales have been schematically summarized in Figure 1.8, including the dislocation pile-up based Hall-Petch law ($\sigma \sim h^{-0.5}$) at sub-micron to micron layer thickness levels, single dislocation based confined layer slip model ($\sigma \sim \ln(h/b)/h$) at a few nanometers to a few tens nanometers layer thickness and interface crossing ($\sigma \neq f(h)$) at 1-2 nm thickness level.

(5) Koehler strengthening (image stress)

Figure 1.8 provides a guideline to the general case of metallic multilayers but the potential strength increase arising from the difference in modulus between constituent layers has not yet been included. The omission of image stress (Koehler stress) is acceptable for the Cu/Nb multilayer system because the elastic modulus of the constituents is similar to each other (e.g. E_{Cu}=110 GPa, E_{Nb}=105 GPa). However, this kind of treatment is perhaps not suitable for other multilayer nanocomposites, especially for those composed of one soft and one hard metal.

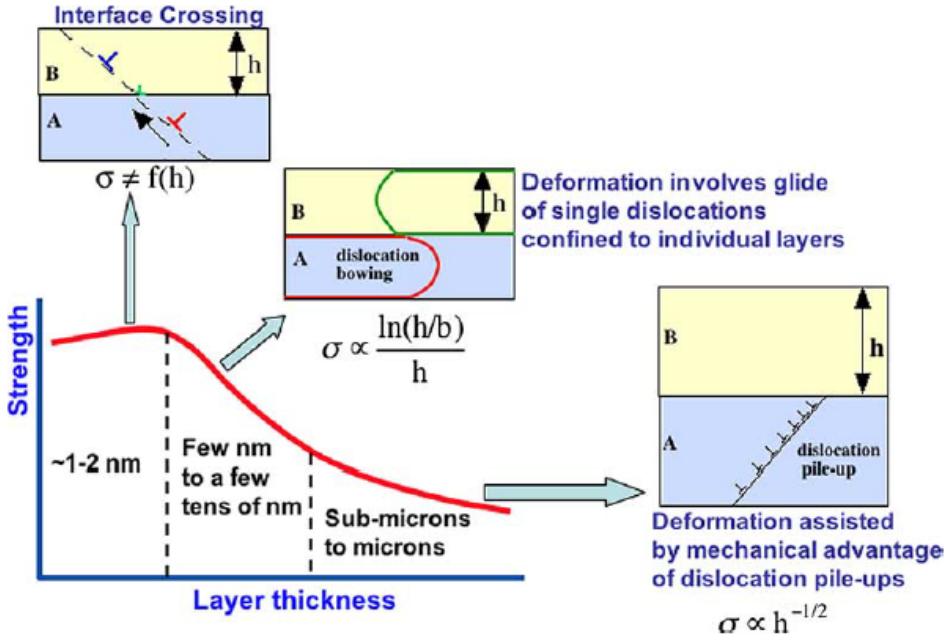

Figure 1.8: Schematic illustrations of the dislocation mechanisms of multilayer strength operative at different length scales [71].

As previously mentioned, the image stress is the resistant force that a glide dislocation must overcome when moving from the soft layer to the hard layer. Based on the isotropic-elastic theory and boundary conditions, Koehler derived the quantitative expression for image stress (in the form of shear stress) [44]

$$\tau_{\text{image}} = \frac{\mu_2 - \mu_1}{\mu_2 + \mu_1} \cdot \frac{\mu_1 b \sin\theta}{4\pi h} \tag{5}$$

where $\mu_1(\mu_2)$ is the shear modulus of soft (hard) layer component and θ is the smallest angle between the interface plane and glide plane of the softer component. He demonstrated that the maximum image stress would be achieved when the distance between the dislocation and interface is equal to core radius ($r_0 \cong 2b$), and is estimated by

$$\tau_{\text{image}}^{\max} = \frac{\mu_2 - \mu_1}{\mu_2 + \mu_1} \cdot \frac{\mu_1 \sin\theta}{8\pi} \tag{6}$$

The Koehler strengthening model was first experimentally confirmed by Lehoczky [110] who found that the strength increase of Al/Cu laminates was in good agreement with Koehler's theoretical predication. For anyone who is attempting to use the Koehler strengthening model, there is an important assumption with respect to its applicability—the thickness of each layer must be small enough to suppress the generation of new dislocations within the layers.

(6) Coherency stress

At the interface, either between the deposited material and the substrate in a single-phase film, or between the constituents in a multilayer film, the alternating compression-to-tension coherency strain exists in two adjacent lattices due to the disparity of lattice constants and gives rise to the coherency stress. Whereas another description of coherency stress is the slope of in-plane force that is varying linearly with the layer thickness when a new layer coherently grows upon the underlayer [111].

Coherency stress has been predominantly detected in iso-structural multilayers since it appears not only in perfectly coherent multilayers but also in the semicoherent multilayers whose interfacial region between misfit dislocations is still coherent and has a coherent elastic stress field. As suggested by Hoagland, et al., the coherency stress for a FCC-based metallic multilayer can be measured as follows [112]

$$\sigma_{\text{coh}} = \frac{C_A C_B}{C_A + C_B} \cdot \frac{a_B - a_A}{2\left(a_B + a_A\right)} \tag{7}$$

where A and B represent the metals contained in the multilayer system. C is the effective biaxial elastic constant and equals $C_{11} + C_{12} - 2C_{12}^2 / C_{11}$, a is the in-plane lattice parameter ($a_2 > a_1$).

They also demonstrated that the coherency stress was the biggest contributor to the slip resistance against dislocations gliding across the coherent interface, based on the peak strength of the Cu/Ni coherent multilayer, ~2.2 GPa calculated by Equation (7). This theoretically predicted strength was slightly larger than the experimentally obtained value of 1.7 GPa owing to the assumption of a perfectly coherent interface adopted in the model. Noteworthy, however, is that Equation (7) is not applicable to iso-structural multilayers with a comparatively large misfit strain, e.g. the Cu/Ag multilayer ($\varepsilon_{\text{misfit}}$ ~12.5%), since the spacing between the misfit dislocations becomes too small to make the dislocation cores separate [112].

As seen from the above strengthening mechanisms, metallic multilayers can be substantially strengthened by trapping the gliding dislocations with phase interfaces, grain boundaries and the mismatch of elastic or lattice constants between constituents, etc. Now it is natural for us to consider the strengthening influence due to twinning, which is another important mode of plastic deformation of metallic multilayers, besides dislocation slips.

Twins have been directly observed in many metallic multilayers via experimental techniques. For instance, Zhang and coworkers found a high density of growth twins and stacking faults in as-deposited polycrystalline Cu/austenitic 330 stainless steel (SS) multilayered films [76]. The growth twins have also been identified by TEM in Cu/Ni [103], Cu/Nb [113], Cu/Cr and Cu/Zr [114] multilayered nanocomposites. From a thermodynamic viewpoint, Zhang et al. claimed that a low twin boundary energy, or a high deposition rate, would facilitate the formation of nanoscale twinning in vapor deposited films [76].

For conventional metals and alloys, the twinning boundary (a coherent interface across which the atomic configuration is symmetric) is believed to be an effective internal obstacle to the transmission of dislocations, akin to grain boundaries. Hence, metallic materials that have a high density of twins usually exhibit ultra-high strength. For example, a tensile yield strength of 900 MPa was achieved in the nanocrystalline Cu samples with a large amount of nanotwins, compared to ~400 MPa for those without nanotwins [115]. The twins in metallic multilayered nanofilms are supposed to improve the strength in the same way. Liu et al. mentioned that the strengthening effects of nanotwins are also reflected by delaying the onset of softening. This was observed when they compared the hardness of (111) textured Cu/Ni multilayer (containing a large number of twins) with the (100) textured Cu/Ni multilayer at various individual layer thicknesses [103].

An earlier simulation work from Rao and Hazzledine revealed that the blocking strength of a (111) twinned interface to the glide of dislocations in Cu/Ni multilayer could reach 0.03μ in magnitude [116]. In this sense, the stress enhancement coming from twinning is too remarkable to be neglected, especially for the multilayered nanofilms containing metallic components with relatively low stacking fault energy such as copper. The study regarding the size-dependent mechanical behavior of Cu/Cr and Cu/Zr multilayers from Niu et al. indicates that only the inclusion of the twining strengthening effects to the refined CLS model, could give a good fit to the experimental results [114].

Shear banding, a narrow region of intense shearing, has been detected in a series of microcompression tests on Cu/Nb nanoscale multilayer samples [117, 118]. As an essential plastic deformation mode for materials lacking dislocations, like amorphous metals, as well as a dominant deformation mechanism for some metals under dynamic

loading (e.g. adiabatic shear bands in ultrafine-grained Fe processed by severe plastic deformation method in Wei's work [119]), shear banding arouses interests in the materials community. As for the formation of shear bands in metallic multilayers, microstructural and loading factors have been taken into account. Mara claimed that the appearance of shear bands in 40 nm Cu/Nb multilayer micropillars is attributed to the weak interfacial strength in such an incoherent system [118]. On another side, Li and Zhang suggested that the interface instability developed in the shear bands is dependent on the length scale of the layers, and that shearing failure is more likely to take place in the Au/Cu multilayer with nanoscale individual layer thickness [120]. This standpoint was supported by Dayal et al. who further proposed the deformation transition from dislocation controlled plasticity at large bilayer thickness to grain boundary mediated shear at small bilayer thickness after examining the deformation morphology of Al/Pd micropillars with bilayer thicknesses of 2, 20 and 80 nm [121].

In addition, some experimental results [118, 122] suggest that the shear banding is a possible cause of the strain softening of multilayers. However, any quantitative estimation of the softening effects from shear banding has not been convincingly established yet. Considering that the deformability of nanostructured multilayers can be modulated by controlling the loading geometry, and thus affecting shear band formation, the research work on this subject is still very valuable in the future.

1.3 Hexagonal Close-packed (HCP) Metals

This thesis will focus on the multilayered nanofilms composed of metals with HCP structures. In comparison with the cubic metals, HCP metals such as magnesium (Mg), titanium (Ti), zirconium (Zr), cobalt (Co) and zinc (Zn), etc., have their own characteristic

crystal structure and consequently the distinctive plastic deformation modes. We will review these fundamentals of HCP metals in this part to better understand the microstructure and mechanical behavior of HCP-based metallic multilayers.

1.3.1 Crystal Structure and General Features

In an HCP unit cell (Figure 1.9), there are six atoms on the basal planes (top and bottom faces) to form a perfect hexagon with another atom at the center. A mid-plane containing three atoms exists between the top and bottom faces as shown in the image. The side length of the hexagon (a) and the distance from the bottom face to the top face (c) are two essential lattice parameters to describe the HCP lattice. For an ideal closed-packed HCP lattice made of hard-sphere model with the coordination number of 12, the c/a ratio is 1.633. Nevertheless, the c/a ratio of most commonly observed HCP metals is less than 1.633. For example, the c/a value of pure Mg is 1.623 while that of α-Ti is merely 1.587. Due to this particular structural feature, the most densely packed plane varies for different HCP metals, and thus there is not a unified slip system. For the same reason, the plastic properties of HCP metals are highly anisotropic, exhibiting pronounced sensitivity to the angle between the **c**-axis of the unit cell and the stress axis. Some HCP metals are also highly anisotropic elastically. For example, it is found that the elastic modulus of α-Ti can vary from 100 GPa (stress axis perpendicular to **c**-axis) to 145 GPa (stress axis parallel to **c**-axis) [123].

It is worth noting that, throughout this dissertation, we use the four-index miller indices to represent the crystallographic planes and directions of HCP metals. The axes $\mathbf{a_1}$, $\mathbf{a_2}$, $\mathbf{a_3}$ and **c** are shown in Figure 1.10. In such a coordinate system, the basal plane is symbolized as (0001), on which the $<11\bar{2}0>$ direction has been sketched out.

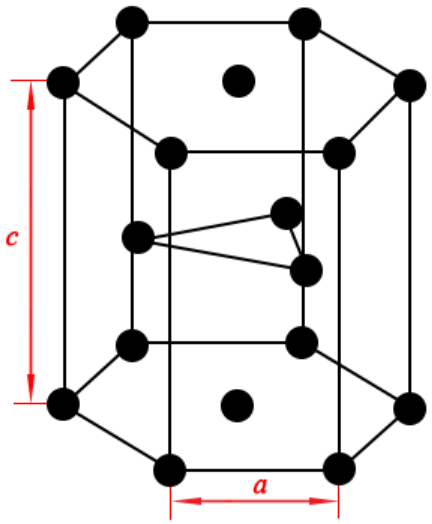

Figure 1.9: The lattice structure of hexagonal close-packed unit cell.

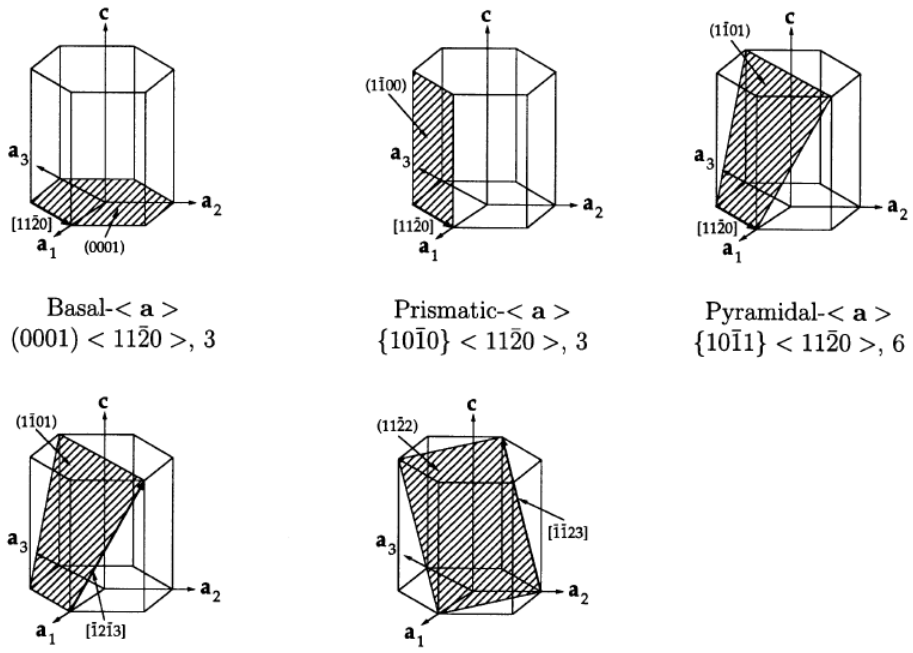

Figure 1.10: Typical slip systems in HCP metals [124].

1.3.2 Deformation Modes in HCP Metals

Now we start reviewing the deformation modes of HCP metals on the basis of documented experimental data. Figure 1.10 displays the typical slip systems summarized for various HCP metals, including <**a**>-type basal slip ($\{0001\}<11\bar{2}0>$), <**a**>-type prismatic slip ($\{10\bar{1}0\}<11\bar{2}0>$), <**a**>-type pyramidal slip ($\{10\bar{1}1\}<11\bar{2}0>$), <**c**+**a**>-type pyramidal slip ($\{10\bar{1}1\}<11\bar{2}3>$) and <**c**+**a**>-type secondary pyramidal slip ($\{11\bar{2}2\}<11\bar{2}3>$). As we have mentioned, the dominating slip system could be totally different for HCP metals with different c/a ratios. Yoo and Wei proposed that the basal slip is prevalent in the HCP metals with $c/a \geq 1.633$, whereas the prismatic slip becomes dominant for those with $c/a < 1.633$ (except beryllium), after calculating the ease of gliding in each slip system [124]. In what follows, we will concentrate on the deformation behavior of Mg, α-Ti and Zr, which are the three HCP metals used to fabricate the HCP-based multilayered nanofilms in this study.

The predominance of basal slip in single-crystal and polycrystalline magnesium at room temperature has been confirmed by a large number of tensile and compression tests [125]. Prismatic slip is relatively difficult to activate since its critical resolved shear stress (CRSS, ~50 MPa) is almost two orders of magnitude larger than that of basal slip (less than 1 MPa) [126]. The operation of pyramidal slips requires even higher applied stresses. However, non-basal slip systems have still been observed in Mg metals and alloys under some special loading conditions or with special microstructures and chemical compositions. For instance, <**a**>-type pyramidal slip was detected in a $<10\bar{1}0>$-oriented Mg crystal under tensile deformation [127]; multiple slip systems were found active on the pyramidal

planes of a single-crystal Mg micropillar (10 μm in diameter and 20 μm in length) compressed along c-axis [128]. In addition, Koike et al. argued that the non-basal slip systems in fine-grained AZ31B alloy (Mg-3Al-1Zn-0.2Mn in wt.%) were activated to reconcile the plastic compatibility stress arising at grain boundaries [129]. In particular, it has been demonstrated that the extent of non-basal slip increases with increasing temperature [130, 131]. The increased activity of prismatic slip in warm-rolled AZ31 alloy as reported by Chun and Davis is a good example [132].

According to the Von Mises criterion, at least five independent slip systems are needed to maintain homogeneous deformation for a polycrystal assembly. Unfortunately, most HCP metals cannot meet this requirement without the operation of secondary pyramidal slip or twinning. Thus twinning becomes an important deformation mode for HCP metals and contributes to the overall strain. In an early study from Yoshinaga and Horiuchi, twinning was demonstrated to be the unique mechanism responsible for the deformation of Mg single crystals compressed in the direction parallel to hexagonal axis [133]. Twins along $\{10\bar{1}1\}$, $\{30\bar{3}4\}$, $\{10\bar{1}3\}$ and $\{10\bar{1}5\}$ planes had been marked out by conducting trace analysis on the surface of deformed specimens. Recent progress in atomistic simulation studies of twinning deformation in pure Mg and Mg alloys, however, indicates $\{10\bar{1}2\}<10\bar{1}1>$ twinning is most common [134]. By changing the energy path of twinning via doping 10 at.% Ti into Mg, the deformation twinning $\{10\bar{1}1\}<10\bar{1}2>$, which ought to be rare in nanocrystalline HCP metals, was surprisingly detected in ball-milled Mg-Ti alloy with an average grain size of 33 nm [135], consistent with the MD simulation result from Li and Ma [136].

As we know, pure titanium experiences the α→β phase transformation at 882 °C where the high temperature stabilized β phase has BCC crystal structure. In what follows, we will concentrate on α-Ti and mainly discuss the deformation behavior of Ti at relatively low temperature, without any phase transformation issues included.

Unlike Mg, Ti and its alloys primarily deform by <**a**>-type prismatic slip. As reflected by the gliding resistance to each slip system [137], pure Ti is much stiffer than pure Mg. Nevertheless, the documented CRSS values of slip systems in Ti vary greatly with temperature and content of impurities. For example, the CRSS of prismatic slip measured by Levine [138] at room temperature was about 20 MPa which was later verified by Akhtar and Teghtsoonian [139], whereas the CRSS of basal slip in pure Ti roughly reached 80 MPa [140]. With a small amount of Al alloying (~6.6 wt.%), room temperature CRSS values of basal slip, prismatic slip and 1st order pyramidal slip in these Ti-Al single crystals increase to 190, 440 and 950 MPa, respectively [141]. The effects of temperature on the CRSS of slip in Ti are remarkable when the testing temperature is below 550 K. Generally the CRSS decreases with increasing temperature [131, 139].

The size effects on the measured CRSS must be noted if the Ti samples with micro- or nanoscale dimensions are of interest. It is quite striking to observe the CRSS of prismatic slip soared from 144 MPa for 10 μm wide α-Ti single crystal micro-cantilevers to 560 MPa for 1 μm wide micro-cantilevers [142]. Sun et al. examined the compressive strength of Ti micropillars oriented for prismatic slips, and found the CRSS is inversely proportional to sample size, in accord with dislocation source nucleation-controlled plasticity [143].

Although prismatic and basal slips are energetically favorable in Ti, pyramidal slips and twinning involving <**c**+**a**>-type dislocations need to be operative during the

deformation so as to accommodate the straining along *c*-axis and maintain the macroscopic ductility. At low temperatures, twinning plays a more important role than slips in the plastic deformation of Ti when the stress axis is parallel to the c-axis. In response to different loading conditions, tensile or compressive, different twinning systems will be activated. For example, $\{10\bar{1}2\}$ and $\{11\bar{2}1\}$ twinning usually appeared under tensile conditions while $\{11\bar{2}2\}$ twinning was frequently observed under compressive applied stress [137]. Unfortunately, the mechanisms related to the nucleation and growth of twins as well as the dislocation-twin or twin-twin interactions in HCP metals are not yet completely understood, with only a small number of publications covering these topics [131, 134, 144-147].

The deformation behavior of Zr is analogous to that of Ti, which is possibly attributed to their approximately identical c/a ratios (1.593 of Zr *vs*. 1.587 of Ti). At microscopic level, Zr is also inclined to deform by non-basal slips. Early on, Akhtar and co-workers performed plenty of mechanical tests on Zr single crystals over a wide range of temperatures and strain rates, which revealed that the prismatic slip is the easiest mode to be activated in all conditions [148-150]. They also found that the ease of basal slip increased with temperature [151].

As an important deformation mode of Zr, twinning has been experimentally observed for a long time. Now the contribution of various twins to the plastic strain can be quantitatively estimated by using the advanced electron backscattered diffraction (EBSD) technique [152-154]. According to such an analysis from McCabe et al., $\{11\bar{2}2\}$ compression twinning is assumed to accommodate roughly one third of the total plastic strain of Zr compressed at 76 K along the *c*-axis [155]. Not only responsible for the plastic deformation, twins are also directly related to the work hardening behavior of Zr in terms

of impeding the propagation of dislocations and other twins. Kaschner et al. even suggested that twinning played the dominant role in hardening while dislocations only had a second order effect based on their examination of mechanical performance of the pre-deformed, textured Zr samples (loaded and then annealed to preserve the twin structure) during reloading process [156].

The deformation mode of polycrystalline HCP metals with randomly oriented grains is much more complicated than that of single crystals or highly textured ones. If the grain orientation is unfavorable for a given loading direction, dislocation glide on the easy slip systems might not be able to take place due to the vanishing Schmid factor, which means little or no resolved shear stress will be distributed for these slips. The characteristic mechanical anisotropy, in conjunction with the possible reorientation of grains during the deformation process, makes the prediction of plastic yielding and flow in polycrystalline HCP metals very difficult.

So far, we have reviewed the major deformation mechanisms of Mg, Ti and Zr. These mechanisms are actually representative of most HCP metals though not all of them. More information about the deformation mechanisms of other HCP metals can be found in several excellent review papers [124, 131, 145].

1.4 Objectives of This Dissertation

A quick survey of the literature shows that most experimental efforts in the study of metallic multilayer nanofilms have focused on those composed of cubic components, for example, FCC/BCC and FCC/FCC types (please refer to Table 1). Recently cubic/hexagonal close packed systems, such as Cu/Zr (FCC/HCP) and Mg/Nb (HCP/BCC) have started to draw attention from investigators [80, 122]. However, taking into account

the increasing technological and scientific importance of many metals with HCP lattice structure such as magnesium, titanium, zirconium and beryllium, greater efforts are called for to exploit the unique characteristics of such metals, particularly in the context of multilayer systems.

First of all, unlike cubic metals which are usually ductile due to the profuse slip systems available, HCP metals have much fewer slip systems. In the case where the number of easy slip systems is restricted, twinning will alternatively become the dominant deformation mode for HCP metals, which has been rarely seen in cubic metals. Multilayered thin films provide a perfect platform to investigate the distinctive deformation mechanisms of HCP metals because of the accurate modulation control enabled by advanced synthesis techniques, even down to the nanometer length scale. And more importantly, it makes the combination of mutually immiscible elements possible, as seen in Cu/Nb multilayers.

Furthermore, taking advantages of their light weight or even ultra-light weight (the mass density of Mg is only 1.74 gm/cm^3, compared to 7.9 gm/cm^3 for steels) and impressive mechanical stiffness, HCP metals become promising materials for use in the automotive and aerospace industry where high weight-to-thrust ratio is necessary. Hence, extending the applications of these metals into the field of multilayered nanofilms and obtaining a full knowledge of their mechanical performance is truly worthwhile.

To the best of our knowledge, there has been no work reporting the synthesis, microstructure and mechanical properties of metallic multilayers between HCP metals. Pd-capped Mg/Ti multilayers were deposited by DC and RF magnetron sputtering, but the focus was on the capacity and kinetics of hydrogen storage of such multilayers and the

maximum thickness of the coating was only ~60 nm [157]. It might be argued that some of the multilayered composites reported in the literature consist of one HCP component [80, 122]. However, a multilayered nanofilm composed of monolithic and stable HCP crystals has not been reported yet in the context of microstructure-mechanical properties relationships.

The dissertation aims to fill this gap by presenting a comprehensive study on HCP-based metallic multilayered nanofilms. Two nanostructured multilayer systems, Mg/Ti and Mg/Zr, are prepared with varying individual layer thickness and subsequently investigated in terms of microstructural evolution and mechanical behavior. In both systems, the constituents are mutually immiscible, which will lead to a high thermal and compositional stability. Figure 1.11 is the phase diagram of Mg-Ti binary system, indicating the components have considerably low mutual solubility. The mechanical responses of HCP-based metallic multilayered nanofilms in nanoindentation and microcompression experiments are carefully examined and compared in order to explore the strengthening mechanisms involved.

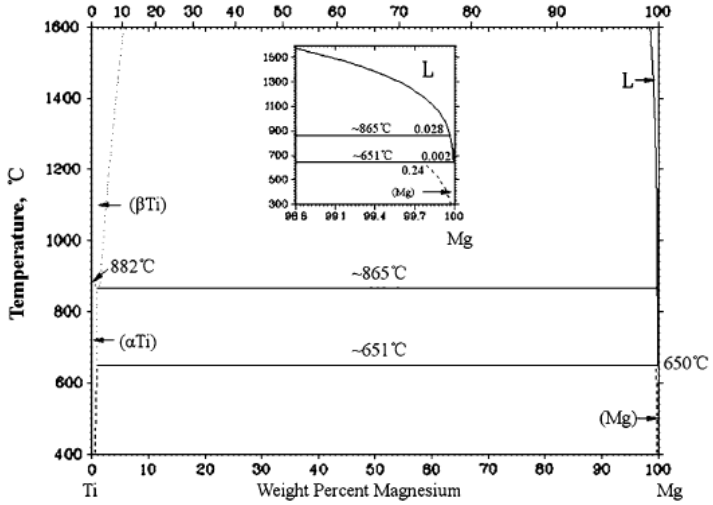

Figure 1.11: The phase diagram of Mg-Ti binary system [158].

CHAPTER 2: EXPERIMENTAL PROCEDURE

In this chapter, we will present a detailed description of experimental methods that have been used to investigate HCP-based multilayered nanofilms, including magnetron sputtering for material preparation, the X-ray based techniques and TEM for microstructural characterization, and nanoindentation and microcompression tests for mechanical property evaluation.

2.1 Preparation of Multilayered Nanofilms

Magnetron sputtering is an efficient physical vapor deposition method to prepare high-precision thin films. Figure 2.1 schematically illustrates a typical process of magnetron sputtering. At first, the Ar gas within the chamber is ionized under an applied high voltage. The Ar ions are then attracted by the negatively charged target (cathode) and fly toward it in acceleration. With the hit of ions, the target atoms (the material to be sputtered) are ejected out and subsequently deposited onto the substrate at the bottom. In such a sputtering system, the magnetic field (at the top of the figure) is installed to trap electrons around the target and enhance the efficiency of ionization. As a result, the efficiency of the whole deposition process has been greatly improved. The films prepared by this coating technique usually have excellent layer uniformity and smooth surface.

The deposition chamber of the magnetron sputtering system used in the present work is an ATC 1800-F by AJA International Inc. It is capable of housing four sputtering

targets, with computer controlled shutters for all the targets. For Mg/Ti multilayers, high purity Mg (99.98%) and Ti (99.99%) were deposited alternately onto Si (100) substrates with nearly identical layer thickness *h*, ranging from 2.5 to 200 nm. Before every deposition, the substrate surface was cleaned by plasma for over 10 min to fully remove the contaminants or perhaps the silicon dioxide on it. The deposition rates of Ti and Mg under ~1.0 mTorr Argon pressure were 0.136 nm/s and 0.417 nm/s, respectively.

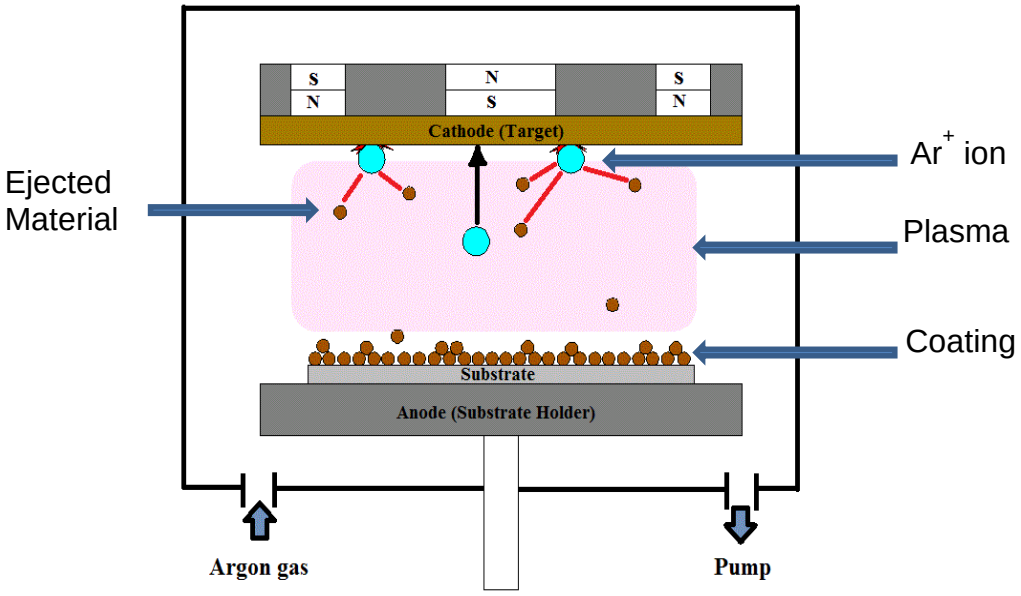

Figure 2.1: The schematic diagram of magnetron sputtering process.

Through the control of bilayer periodicity, the total multilayer thickness of each sample was kept at approximately 1.0 μm when the individual layer thickness is no more than 100 nm. For the sample with thicker layers (200 nm), the total thickness was around 5.0 μm. In all the specimens, a 2 nm-thick Ti layer was first deposited on the silicon substrate because Si and Ti have relatively strong chemical bonding. Since Mg is very reactive, the top layer of all the multilayer films is Ti, in order to avoid sample degradation

with time after retrieval from the chamber. Table 2 presents the periodicity information of all seven Mg/Ti multilayers.

The preparation of Mg/Zr multilayered films followed the same route as that for Mg/Ti samples, except the deposition rates of Zr and Mg under ~1.0 mTorr Argon pressure, which were 0.134 nm/s and 0.368 nm/s, respectively. For all the depositions, the substrate was kept at room temperature.

Table 2: Periodicity of as-deposited Mg/Ti multilayered nanofilms.

No	Thickness per layer (nm)	Period of bi-layer	Thickness of additional Ti cover layer (nm)	Thickness of interface Ti layer (nm)	Total thickness (μm)
1	2.5	200	2.5	2	~1.0
2	5	100	5	2	~1.0
3	10	50	10	2	~1.0
4	20	25	20	2	~1.0
5	50	10	50	2	~1.0
6	100	5	--	2	~1.0
7	200	12	--	2	~5.0

2.2 Microstructural Characterization

One of the principal goals of studying thin films is to thoroughly understand their microstructure-mechanical property relationship. Therefore, the very first step to investigate the freshly prepared multilayer nanofilms is characterizing the microstructure. Two major methodologies, X-ray tests and transmission electron microscopy (TEM), have been employed here to examine the microstructural and crystallographic evolution of HCP-based multilayered nanofilms with varying layer thickness.

2.2.1 X-ray Related Tests

Since its advent, X-ray diffraction (XRD) has been a useful tool to reveal the inner structure of objects that would be impossible to discern with naked eyes. The wavelength of X-rays (0.1—100 Å) is much shorter than the visible spectrum, thus it has more energy to penetrate into the surface and subsequently interact with atoms inside [159]. In the materials community, X-ray crystallography has been used prevalently to determine the atomic arrangement of specimens (single crystal, polycrystalline or amorphous) based on the diffraction pattern of X-ray beams that pass through the closely spaced atoms. If the inspected material is crystalline, the regular arrays of atoms will lead X-ray beams to diffract at specific incident angle θ, as shown in Figure 2.2. The crystallographic information of this material can be derived by Bragg's law

$$2d\sin\theta = n\zeta \tag{8}$$

where d is the planar spacing and ζ is the wavelength of applied X-ray, and n is an integer denoting the order of diffraction, which usually equals 1 for XRD.

One of the basic functions of the XRD is to identify the phases involved in the tested materials. Whereas amorphous materials do not have sharp peaks in their diffraction patterns due to the random distribution of atoms, the diffraction pattern of crystalline specimens usually contain characteristic peaks whose angular positions are related to certain phases according to Equation (8). Meanwhile, the intensity of these peaks reflects the preference of crystallite or grain orientation. Highly textured materials generally exhibit one or two prominent peaks whose intensity is high enough to mask other diffraction peaks on the pattern.

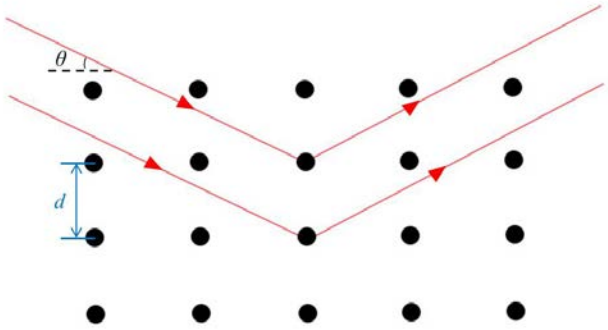

Figure 2.2: A schematic illustration of Bragg's law.

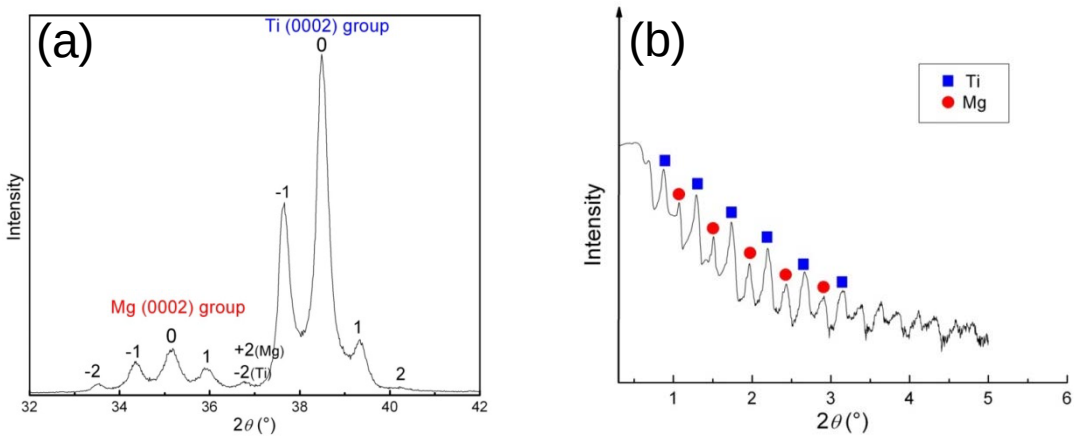

Figure 2.3: Representative results from X-ray diffraction (XRD) and X-ray reflection (XRR) tests on Mg/Ti multilayer nanofilms. (a) Magnified XRD pattern of the nanofilm with *h*=5 nm. (b) XRR pattern of the nanofilm with *h*=50 nm.

In addition to the identification of phases and preferred orientation as described above, XRD can be used to determine the lattice mismatch between film and substrate, measure residual strain and stress, and calculate the layer thickness for thin film materials [160, 161]. The last function is what we are most interested in with regard to the X-ray diffraction measurements on multilayered nanofilms, because it provides an efficient way to testify the precise deposition of layers on the substrate. In what follows, we will give a

brief description about how to measure the individual layer thickness of our HCP-based multilayers by means of X-ray related tests.

XRD traditionally refers to the high-angle X-ray test where the scanning angle θ satisfies $2\theta \geq 15^{\circ}$ while the X-ray test with $2\theta < 15^{\circ}$ is named as X-ray reflectivity (XRR). Both of them can be used to determine the modulation period Λ of multilayered composites. Consider binary multilayers of equal thickness as our HCP-based metallic multilayered nanofilms, there are always equally spaced satellite peaks surrounding the ordinary and primary Bragg peaks (Figure 2.3(a)) because of the similar out-of-plane lattice spacing. The position θ of the *m*-th order satellite peaks satisfies

$$\sin\theta_{\pm} = \sin\theta_B \pm \frac{m\zeta}{2\Lambda} \tag{9}$$

where θ_B is the position of the ordinary Bragg peak.

XRR provides an alternative approach for the measurement of the bilayer period of multilayer films through the reflection of incident X-rays off the interfaces between the layers. Several periodic peaks could be detected at small angles, such as those displayed in Figure 2.3(b). The bilayer period Λ is then calculated by a modified Bragg's law as follows

$$\sin^2\theta = \left(\frac{m\zeta}{2\Lambda}\right)^2 + 2\delta \tag{10}$$

where *m* is the order of reflection; δ is generally on the order of $1\text{x}10^{-5}$ and can be neglected [157]. From a liner plot of $\sin^2\theta/\zeta^2$ versus m^2, the value of the interlayer thickness (or periodicity) Λ can be accurately determined.

In this work, both XRR and XRD have been carried out in Bruker AXS D8 Discover X-ray diffractometer to examine the bilayer period of the as-deposited HCP-based multilayered nanofilms. The wavelength of Cu-K_α radiation being used is 0.154 nm. The XRR and XRD results were also compared against each other to verify the appropriate modulation.

2.2.2 Transmission Electron Microscopy

The cross-sectional microstructure of Mg/Ti multilayer films were examined by transmission electron microscopy (TEM) and high resolution transmission electron microscopy (HRTEM) on the JEOL 2100 microscope operated at 200 kV. All the TEM samples were cut, milled and finished by Focused Ion Beam (FIB) technique on an FEI Nova 600i dual beam FIB system (US Army Research Laboratory).

2.3 Evaluation of Mechanical Behavior

2.3.1 Nanoindentaion Experiment

To investigate the mechanical behavior of materials with relatively small dimensions on the order of micrometers or less, nanoindention is probably the most popular testing technique that has been applied. It is a miniature indentation test commonly equipped with a small indenting tip and a highly sensitive loading frame (sub-micron newton resolution). The fundamental theories and working principles of the nanoindentation testing system will be introduced in detail in this section since we employed the instrumented nanoindenter as the primary means to probe the mechanical properties of as-deposited and annealed multilayered nanofilms in this study.

Currently, instrumented nanoindenter systems still follow their conventional macro- or micro- counterparts to obtain the hardness *H* of tested materials by utilizing Equation (11)

$$H = \frac{P_{\max}}{A} \tag{11}$$

where $P_{\max}$ is the peak load as measured and *A* is the projected area of impression. With advanced loading transducers, the applied force can be accurately measured during the tests. However, the direct measurement of indentation area has always been conducted in traditional experiments by imaging the indentation with optical microscopy, and is impractical in nanoindentation tests due to the nearly invisible indentation created by such a small tip. In order to solve this problem, microscopes with higher magnifications such as scanning electron microscopes (SEM) and atomic force microscopes (AFM) were applied to inspect the indentation after loading [162]. The calibration of the projected area performed using these microscopes is, unfortunately, still too troublesome and time-consuming to offer a convenient and easily operated nanoindentation test.

A significant development concerning this issue was made by relating the contact area to contact depth h_c of the indentation (Figure 2.4(a)) via the area function $A = F(h_c)$. For a Berkovich indenter, the area function could be described as

$$A = 24.5h_c^2 + C_1h_c^2 + C_2h_c^{1/2} + ... + C_8h_c^{1/128} \tag{12}$$

where C_1 through C_8 are constants to be verified before the test. The contact depth is generally inferred from the indenting load-displacement curve as shown in Figure 2.4(b) by

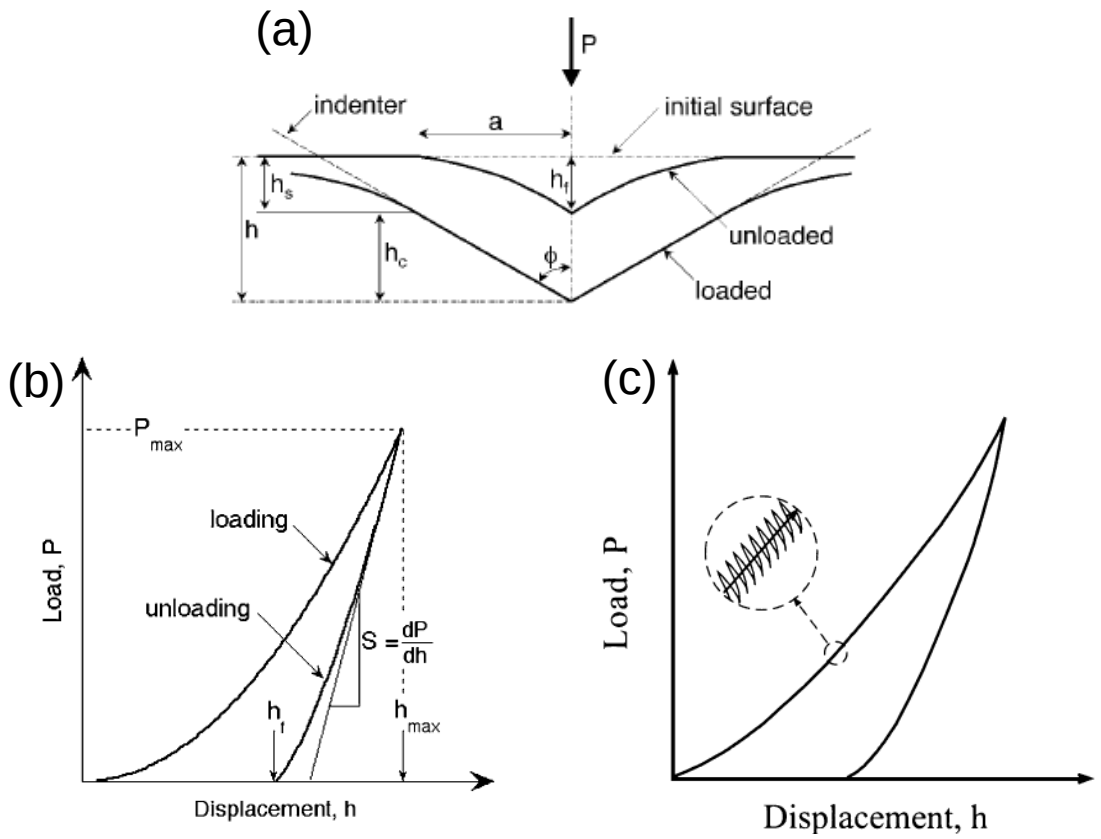

Figure 2.4: Schematic illustrations of (a) the unloading process showing parameters characterizing the contact geometry [163]; (b) the indentation load–displacement data showing important measured parameters [163]; (c) the CSM loading cycle [164].

$$h_c = h_{\max} - \varepsilon \frac{P_{\max}}{S} \tag{13}$$

where S is the contact stiffness, a key parameter in nanoindentation tests and will be discussed later. $h_{\max}$ is the maximum indenting depth while the geometric constant ε in Equation (13) is 0.75 for a Berkovich indenter.

Another important mechanical property of the specimen that has been frequently measured in nanoindentation tests is the elastic modulus E. It can be quantitatively determined by Equation (14) as follows

$$E_r = \frac{1-\nu^2}{E} + \frac{1-\nu_i^2}{E_i} \tag{14}$$

where ν and ν_i are the Poisson's ratios of the tested material and the indenter material, respectively. E_i is the elastic modulus of indenter while E_r is the reduced modulus in conjunction with the contact stiffness S and contact area A

$$E_r = \frac{S}{2\beta}\sqrt{\frac{\pi}{A}} \tag{15}$$

where β is a constant that depends on the indenter geometry and equals 1.034 with respect to the Berkovich tip.

As seen from the above equations, contact stiffness S is the only parameter that has not been determined yet in our calculation of hardness and elastic modulus. Figure 2.4(b) presents a basic method to obtain S, through differentiating the load with the displacement at h_{max} on the unloading portion of the experimental load-displacement curve. However, in our tests the continuous stiffness measurement (CSM) method developed by Oliver and Pharr was adopted. By imposing a small dynamic oscillator on the force signal as depicted in Figure 2.4(c) and then tracing the phase or amplitude changes of the signal with a frequency-specific amplifier, the contact stiffness can be identified instantaneously and continuously as a function of the indenting depth even during the loading process. Thus there is no need for multiple loading and unloading cycles in a single indentation test. Because of its advantages, the CSM technique has been deemed as an ideal testing method of mechanical properties for multilayered nanofilms and other graded materials of small volume, and its importance has been widely recognized during the last two decades [164, 165]. Additionally, in the CSM method, the effects from thermal drift and time-dependent

plasticity are primarily estimated by holding a low level of load for certain time period and excluded from the load-displacement data so as to achieve accurate measurements.

Unlike bulk materials or thicker free-standing films, the calibrated displacement of thin films under the indenter tip inevitably comprises both the contribution from the deformed substrates, especially the soft ones as well as the film. Hence, it becomes difficult to figure out the intrinsic deformation characteristics of the film materials and would be detrimental to the accuracy of evaluating mechanical performance of the films by indentation tests. After conducting numerous nanoindentation tests on a wide variety of film/substrate combinations, Saha and Nix demonstrated that, in the case of a soft film on a hard substrate, the substrate had negligible effects on the measured hardness of the thin film since the plastic deformation induced by the indenter was contained within the film unless the indenter had penetrated the substrate. For the hard film on a soft substrate, an indenting depth less than 10% of the total thickness of the tested film could also diminish the substrate effect to the negligible level [166]. Following these findings, along with the rule proposed by Buckle [167], the maximum indenting depth for all the nanoindentation experiments performed in this study was monitored in the range of 10-15% of the film thickness.

With all these considerations incorporated, the nanoindentation tests were carried out on the MTS (now Agilent) NanoIndenter G200 with a Berkovich diamond indenter tip. The load and displacement resolutions of this system are about 1 nN and 0.0002 nm, respectively. The CSM method was applied to measure the hardness H and Young's modulus E of the HCP-based multilayered nanofilms at a constant strain rate of 0.05 s^{-1} (without specific indication, hardness or flow strength mentioned in the following were

acquired at this strain rate, and the issue of strain rate sensitivity will be addressed separately later on). The hardness value reached a plateau and became stable when the indentation depth exceeded 50 nm in our tests before significant substrate effect kicks in. The nanoindentation data was collected with a maximum indenting depth about 10-15% of the whole thickness for each film in order to reduce the effects from the silicon substrate and to obtain accurate results of *H* and *E*.

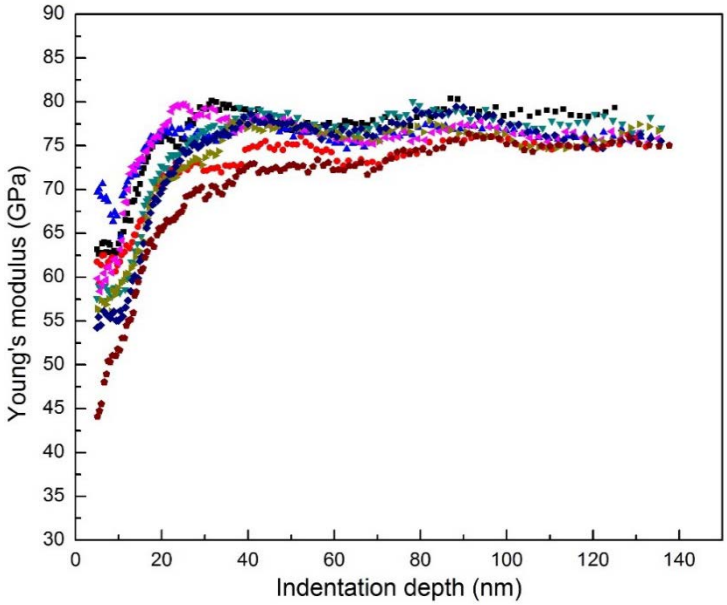

Figure 2.5: A typical indentation depth *vs.* Young's modulus relation of Mg/Ti multilayered nanofilms obtained from nanoindentation experiments.

2.3.2 Microcompression Experiment

The microcompression test is a new, but fast growing methodology to measure the direct response of stress-strain behavior of nearly any inorganic material of small dimensions. About ten years ago, Nix, Uchic and their coworkers first developed this mechanical testing system and provided us a ready path to explore the plastic deformation of materials even with a size of several micrometers [168]. So far the microcompression

test has been applied to the mechanics study of metallic glass, single crystals, multilayered thin film, nanocrystalline, nanoporous metals, etc. [69, 143, 169-171].

Figure 2.6 schematically shows the geometry of a microcompression testing system. At the bottom, we can see a cylindrical (or cuboid) sample pillar aligned perpendicular to the bulk surface, with one end integrally attached to the bulk specimen. The pillar normally has a diameter of 0.5 to 40 μm and is usually fabricated by the focused ion beam (FIB) milling technique. Above the pillar is the loading frame which is actually a simple extension of the nanoindentation instrument but has the sharp Berkovich indentation tip truncated into a flat-punch shape. Because of the extremely high resolution in loading and displacement measurements, the nanoindentation loading system is believed to be the most efficient one to evaluate the mechanical behavior of tested materials at the micro- or nano-scale.

In a single microcompression test, as the flat tip presses on the top of the pillar and continues moving down, instantaneous load and displacement can be precisely recorded during the loading process and then converted to the true stress (σ_T)-true strain (ε_T) curves according to the standard Equations (16) and (17)

$$\sigma_T = \frac{F}{A_0}\left(1-\frac{\Delta l}{l_0}\right) \tag{16}$$

$$\varepsilon_T = \ln\left(1-\frac{\Delta l}{l_0}\right) \tag{17}$$

where F is the measured loading force while Δl (positive) is the displacement; A_0 and l_0 are the initial cross-sectional area and length of the undeformed pillar, respectively. Figure

2.7 is the scanning electron microscope (SEM) image of a microcompression pillar fabricated from our as-deposited Mg/Ti nanofilm with an individual layer thickness of 100 nm, just before the loading process.

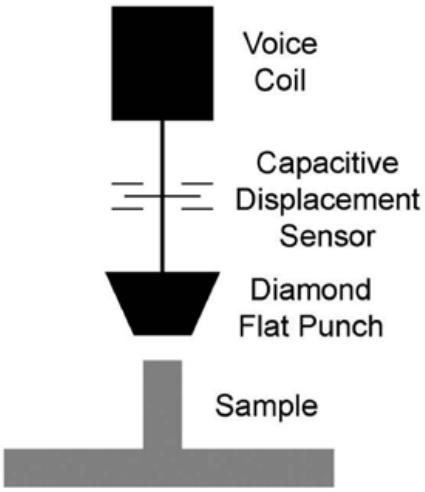

Figure 2.6: A schematic illustration of the geometry of microcompression testing system.

Microcompression tests hold almost the same working principles as those in conventional compression tests which are commonly performed at macro-scale, except for the small size scale of specimens and unnecessary micromanipulations of specimens to install them in the testing frame. However, like other miniature mechanical testing experiments, caution is required to perform the microcompression tests accurately and interpret the experimental results correctly. The geometric concerns of the miniaturized micropillars and their influences on the final stress-strain responses are the primary considerations, and such issues include: the size effect, aspect ratio (length-to-diameter ratio), misalignment and tapering. These factors might induce incorrect estimations regarding the mechanical behavior of specimens [172], and must be tackled carefully.

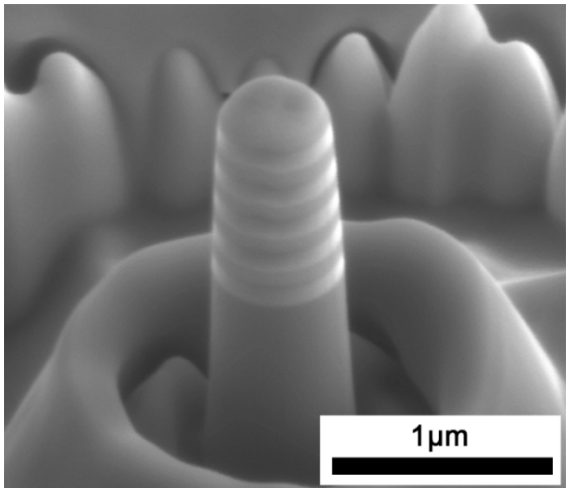

Figure 2.7: The SEM image of a micropillar fabricated from our as-deposited Mg/Ti nanofilm with an individual layer thickness of 100 nm.

Size effects have been detected in microcompression tests and other micro-mechanical tests on single crystal specimens where the measured strength increases with the decrease of sample size ("smaller is stronger"). From Uchic's work, this size-dependent strengthening phenomenon of FCC metals in the microcompression experiments can be described by an empirical power-law equation between the flow stress σ and pillar diameter d as followed

$$\sigma = Ad^{-n} \tag{18}$$

where A is a coefficient related to the shear modulus and Burgers vector of the tested material. He also showed a good match of the equation to the experimental data for various FCC metals when n was selected as 0.6 [168, 173]. The effects of aspect ratio on the flow strength have been systematically investigated in the work of Zhang and co-workers by utilizing 2D and 3D finite element modeling [174]. Based on their findings, the aspect ratio of the tested pillar was recommended to be 2—3 in order to suppress the potential buckling and augmented but spurious strain hardening. Tapering is a kind of fabrication inaccuracy

introduced during the preparation of pillars, especially when the FIB milling is perpendicular to the sample surface. The tapered sample would produce a non-uniform stress distribution within the pillar and would consequently yield adverse effects on the measurements of flow stress, as indicated in the relevant studies from Zhang and Shan [174, 175]. However, any quantitative correction with respect to this problem has not been solidly established.

Besides the geometrical concerns listed above, other factors emerging in the loading procedure are also possibly harmful to the fidelity of microcompression experiments. For example, the friction between the flat tip and post pillar would lead to the overestimation of measured flow strength; the misalignment between the end surface normal of the tip and the pillar axis could bring about deviations of the elastic part of the eventual stress-strain curve and consequently an overall underestimated elastic modulus. Even the intrinsic strain hardening behavior of the tested material is able to affect the experimental accuracy. The simulation works from Zhang indicates that the microcompression technique is more appropriate for testing materials with a lower strain hardening. With regards to all the error sources mentioned above, the data obtained from microcompression tests should be evaluated carefully and critically.

Theoretically, the uniaxial tensile test is preferred for its advantageously uniform stress distribution at the gage section but the complex preparation and manipulation of tensile specimens with a size of several microns or less prevents it from extensive applications in micro-mechanical research. That is why the microcompression experiment has become more popular for the investigations of mechanical properties and deformation mechanisms in the regime of multilayered nanofilms. From the literature,

microcompression experiments have already been successfully executed to obtain the straightforward mechanical responses of Cu/Nb, Al/Nb, Al/Al_3Sc and Cu/Zr nanostructured multilayers [67-69, 118, 122]. In addition, Carpenter and his colleagues performed the microcompression tests with repeated jumps in strain rate (10^{-3}—10^{-5} s^{-1}) to measure the strain rate sensitivity and activation volume of Cu/Ni metallic multilayer thin films [176].

In this study, we first used FIB technique to fabricate micropillars of the Mg/Ti multilayers with various individual layer thicknesses. An approximate aspect ratio of pillar height:diameter of 2:1 was chosen. The microcompression experiments were then performed on a Nanoindenter XP I with a flat punch of diamond pressing against the pillar top at a nominal strain rate of 10^{-5} s^{-1}. Pre-loading and post-loading examinations of the pillars were carried out within the dual beam system (FEI Nova 600i) after the tests. For each pillar sample, the essential parameters l_0 and A_0 used to calculate strain and stress were measured directly from the SEM images.

2.3.3 Strain Rate Sensitivity Measurement

Since strain rate sensitivity (SRS) is an important finger-print for the plastic deformation mechanisms of materials [177, 178], we evaluated the strain rate sensitivity of the multilayers using instrumented nanoindentation. In this case, the hardness of the specimens was measured at different strain rates defined by

$$\dot{\varepsilon} = \frac{\dot{P}}{2P} \tag{19}$$

where P is the load and $\dot{P} = dP/\mathrm{d}t$ is the rate at which the load is applied. In this study, the nanoindentation tests were intentionally carried out at various strain rates of 0.005, 0.01,

0.05 and 0.1 s^{-1} on the Mg/Ti and Mg/Zr multilayered nanofilms. The strain rate sensitivity *m*, in terms of hardness, is defined by

$$m = \frac{\partial \log H}{\partial \log \dot{\varepsilon}} \tag{20}$$

To maintain the consistency with the flow strength (obtained by dividing the hardness by a factor of 2.7 on the basis of Tabor relation [179]), the activation volume associated with the plastic deformation is then calculated as

$$V^* = \frac{2.7 \times \sqrt{3} kT}{H \cdot m} \tag{21}$$

In Equation (21), k is the Boltzmann constant and T is the absolute temperature (in Kelvin). If the values of the activation volume are measured, important information can be derived regarding the mechanisms of the plastic deformation of the samples. Recently there have been efforts on this issue from different groups [114, 176] in the context of metallic multilayer systems.

2.4 Heat Treatment

As-deposited Mg/Ti multilayered nanofilms were annealed at various temperatures and time periods to investigate their thermal stability. Since the layer constituents, Mg and Ti, are vulnerable to oxygen, water and other possible contaminants, we wrapped the multilayer specimens tightly in Al foils and placed into the Barnstead-Thermolyne Model FA 1500 furnace to conduct all the heat treatments. Argon gas were introduced into the furnace throughout the annealing process to reduce the oxidation and corrosion to a negligible level. The annealing temperatures were kept as 50, 100, 150 and 200˚C, while the annealing time varied from 0.5 to 2 hours.

CHAPTER 3: MAGNESIUM/TITANIUM MULTILAYERED NANOFILMS

In this chapter, we will firstly describe the experimental results of the Mg/Ti multilayered nanofilms in terms of crystallography, microstructure and mechanical performance, and then we will explicitly discuss the microstructural evolution and mechanical properties of the Mg/Ti multilayers as a function of the individual layer thickness. At last, the thermal stability of these Mg/Ti multilayered nanofilms will be analyzed in detail.

3.1 Crystallography and Microstructure

Figure 3.1 shows the XRD results of Mg/Ti multilayered nanofilms with various individual layer thicknesses. It is clearly seen that the constituents are highly textured along the Mg (0002) and Ti (0002), since those two peaks exhibit the strongest intensity. Very weak intensity is observed from Ti $(10\bar{1}0)$ reflections for individual layer thickness h=100 nm and h=200 nm, respectively. However, this peak ($(10\bar{1}0)$) is disappearing from the XRD pattern of nanofilms with smaller individual layer thickness, implying a stronger preferentiality in orientation as the layer thickness is decreased. Due to the superlattice structure, satellite peaks start to emerge symmetrically about the Bragg peaks of Mg (0002) and Ti (0002) reflections, when the layer thickness is less than 20 nm. Higher-order satellite peaks become visible when the XRD pattern is amplified about the major Bragg peaks, as shown in Figure 2.3(a) for h=5 nm.

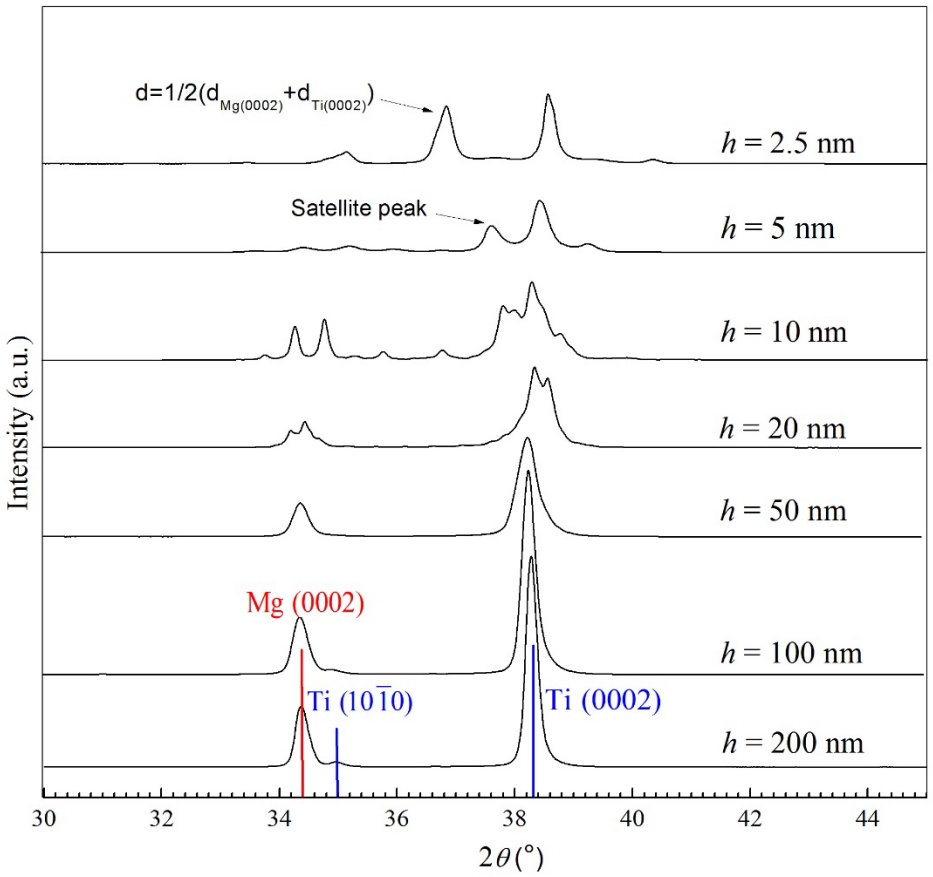

Figure 3.1: X-ray diffraction results of as-deposited Mg/Ti multilayered nanofilms with various individual layer thicknesses *h* (from *h*=2.5 nm to *h*=200 nm).

From the XRD spectra, the majority of constituents, both Mg and Ti, are growing preferentially in the direction perpendicular to the basal plane (or in the *c*-axis direction). It provides indirect evidence for the paralleling growth mode or inter-epitaxial growth between Mg and Ti in the Mg/Ti multilayered nanofilms, particularly for those with small individual layer thickness. Epitaxial growth between the nanolayers has also been observed in other deposited multilayer films [180, 181]. Additionally, in Figure 3.1, the Bragg peaks of Mg and Ti shift to larger θ direction gradually with the decrease of *h*, which usually results from the lattice distortion or residual stress introduced during deposition. We thus measured the change of θ and calculated the maximum lattice strains of Mg and Ti to be

2.14% and 0.40%, respectively. Compared with the high strength of these multilayers to be shown in follows, the possible residual stress is one order less in magnitude and almost negligible.

As mentioned in Chapter 2, the bilayer period Λ ($\Lambda = h_{\mathrm{Ti}} + h_{\mathrm{Mg}}$) of multilayered thin films can be determined from their XRD data following Equation (9). The results for the various specimens are summarized in Table 3. The very small discrepancy between XRD results and the designed bilayer periodicity indicates that the XRD measurements of periodicity in the multilayers based on the position of satellite peaks are quite reliable. It also suggests that relatively accurate modulation and control of Mg and Ti laminates have been achieved in our study.

Table 3: The values of bilayer period Λ measured by low angle X-ray reflection (XRR) and high angle X-ray diffraction (XRD) for the Mg/Ti multilayered nanofilms.

Designed bilayer period Λ $\Lambda = h_{\mathrm{Ti}} + h_{\mathrm{Mg}}$/nm	Λ measured from XRR /nm		Λ measured from XRD/nm	
	Average	Error	Average	Error
10 (5+5)	11.27	0.52	11.22	0.05
20 (10+10)	19.31	0.79	18.27	0.05
40 (20+20)	37.7	1.8	37.11	0.07
100 (50+50)	93.6	9.1	--	--
200 (100+100)	197	28	--	--

Another interesting feature as seen in Figure 3.1 is the existence of a peak ($\theta_{\mathrm{center}} = 36.86$) situating between the characteristic Mg (0002) and Ti (0002) peaks ($\theta_{\mathrm{Mg}} = 35.16$ and $\theta_{\mathrm{Ti}} = 38.58$) on the *h*=2.5 nm curve. As suggested by Schuller [182], a central peak with position angle equal to the numerical average of Bragg peak of constituents in a binary layer system (e.g. Cu/Nb) would appear when the individual layer

thickness is small enough (about 1—2 nm). This kind of lattice constraint generally indicates the increase of coherency along the interface and has also been observed in some incoherent multilayer composites, such as Cu/V [72] and Ag/Ni [79].

Since Mg and Ti nanolaminates were deposited alternately to build up the whole multilayer specimen, their corresponding peaks on the XRR patterns also appear in an alternate manner. An example is provided in Figure 2.3(b), which is the XRR result of the 50 nm Mg/50 nm Ti multilayer in the small scanning angle regime. The peaks of Mg and Ti are equally spaced, and their positions have a nearly proportional relationship with the order of reflection as referred in Equation (10). Based on the XRR results, we derived the average bilayer thicknesses for the specimens, with the results also given in Table 3. We can obviously see that the results from XRR are in very good agreement with those from XRD.

Figure 3.2(a) is the bright-field TEM image illustrating the cross-sectional microstructure of the Mg/Ti multilayered nanofilm with an individual layer thickness of 10 nm. The clear and sharp interfaces reveal there is not significant intermixing between constituents. Despite the uniform lamellar morphology across the whole cross-sectional view, two major orientation relationships (OR) have been identified between Mg and Ti which are labeled as OR.1 and OR.2 (two boxed regions in the Figure 3.2(a)), respectively. Selected-area diffraction (SAD) patterns corresponding to OR.1 and OR.2 are displayed in Figure 3.2(b) and Figure 3.2(c) separately. OR.1 refers to the orientation relationship of Mg $\{0002\}$ // Ti $\{0002\}$ and Mg $< 01\bar{1}0 >$ // Ti $< 01\bar{1}0 >$, indicating the epitaxial growth between the two HCP components, as has been testified already by XRD. In the second orientation relationship, Mg lattice maintains the same growing direction as that in OR.1,

but the Ti lattice switches to develop along the axis perpendicular to the prismatic planes, whose reflections was also detected in XRD results. This therefore leads to OR.2, which is Mg $\{0002\}$ // Ti $\{01\bar{1}0\}$ and Mg $<2\bar{1}\bar{1}0>$ // Ti $<0001>$. As a matter of fact, the distributions of OR.1 and OR.2 seem to be totally random, and it is hard to relate these crystallographic orientation relationships to specific locations within this 10 nm Mg /10 nm Ti multilayer sample.

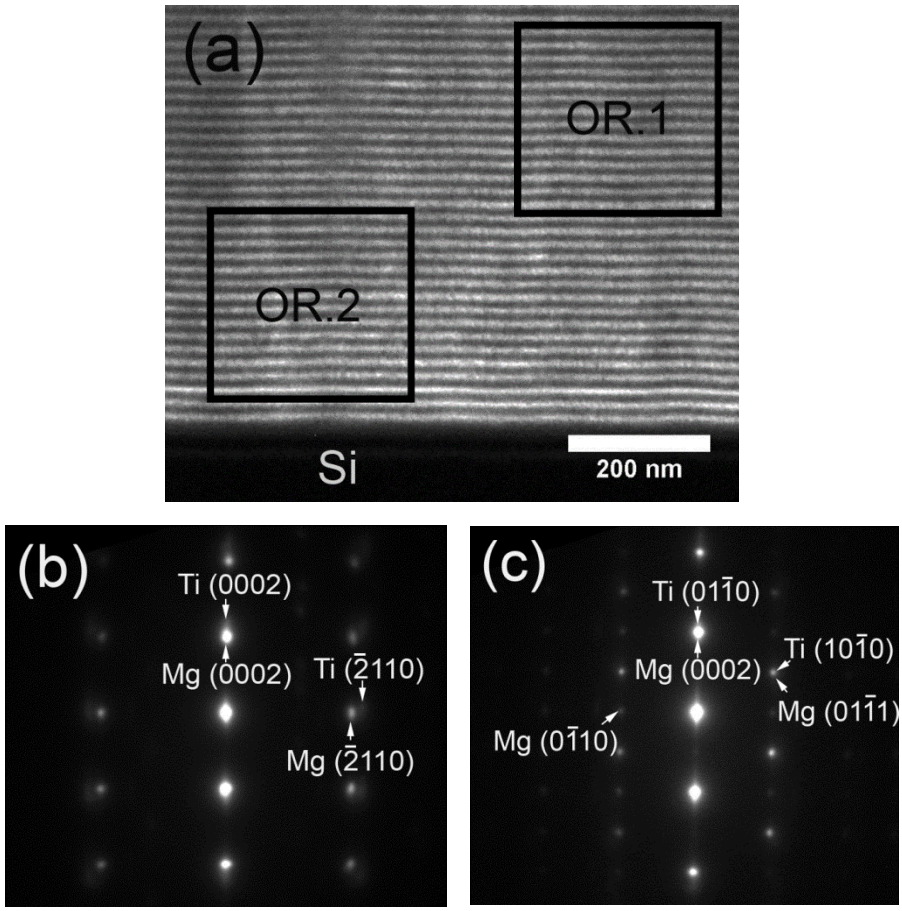

Figure 3.2: (a) The bright-field TEM micrograph of the cross-sectional area of the Mg/Ti multilayered nanofilm with *h*=10 nm. The two boxed regions in this image correspond to the diffraction patterns of (b) and (c), respectively. The orientation relationship between Ti and Mg corresponding to (b) is OR.1, and to (c) is OR.2.

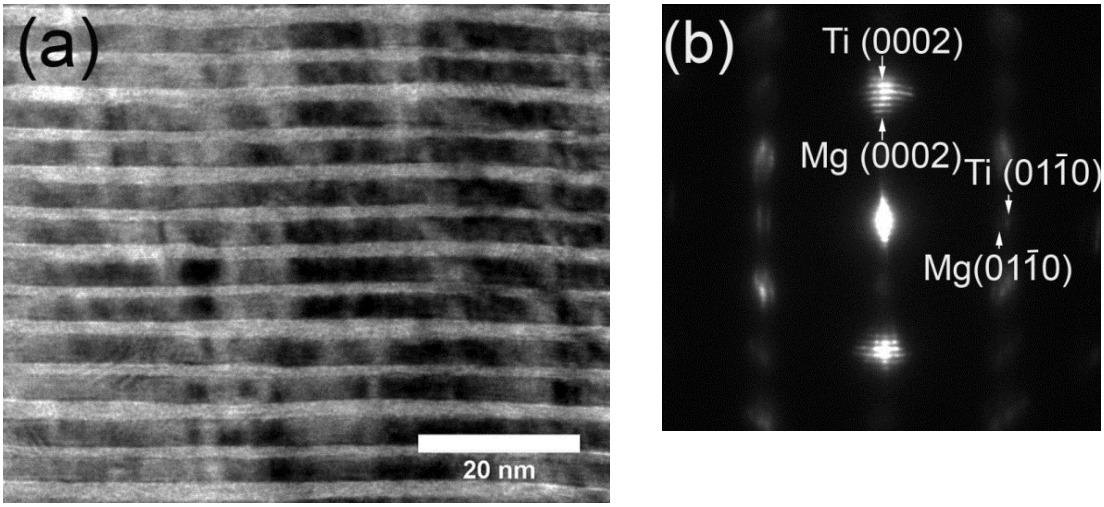

Figure 3.3: (a) The bright-field TEM micrograph of the cross-sectional area of the Mg/Ti multilayered nanofilm with *h*=2.5 nm. (b) The diffraction pattern of orientation relationship OR.1' (Mg $\{0002\}$ // Ti $\{0002\}$ and Mg $<2\bar{1}\bar{1}0>$ // Ti $<2\bar{1}\bar{1}0>$) identified in *h*=2.5 nm Mg/Ti sample.

However, OR.2 could hardly be detected by examining the whole cross-sectional microstructure of the specimen with an individual layer thickness of 2.5 nm. Figure 3.3(a) shows a bright field TEM image of the multilayer structure in this specimen. Besides OR.1, there is another orientation relationship OR.1': Mg $\{0002\}$ // Ti $\{0002\}$ and Mg $<2\bar{1}\bar{1}0>$ // Ti $<2\bar{1}\bar{1}0>$ identified from this nanofilm, as shown in Figure 3.3(b). This relationship also reflects the epitaxial growth between Mg and Ti layers while the in-plane rotation of crystals contributes to its minor difference from OR.1 (Figure 3.4). From the SAD pattern in Figure 3.3(b), the spots are seen to split into several strings because of the extremely fine lamellar structure, which is called streaking [183]. For this very nanofilm with the finest layers (*h*=2.5), the constituent components, Mg and Ti, exclusively follow the orientation relationship of Mg $\{0002\}$ // Ti $\{0002\}$. This is further confirmed by direct observations of the atomic arrangement of each layer via high-resolution TEM imaging. A

representative HRTEM image is provided in Figure 3.5, where the orientation relationship has been marked out. The average spacing between two adjacent Mg atomic layers along the direction normal to the Mg/Ti interface is measured to be 2.58 Å, which is very close to half of the lattice parameter in the *c*-axis of HCP Mg, i.e., c_{Mg} =5.21 Å. The Ti layers exhibit similar characters. Along (0002) orientation as has been sketched out in Figure 3.5, all the Mg and Ti atoms are stacking with a perfect ABAB…sequence of HCP structure within the layers. When the last "A" atomic layer of Mg is finished, the following deposited Ti atoms prefer occupying atomic positions identical to "B" layer of Mg above the last "A" layer. As compared to the perfect HCP crystal, a small distortion of lattice at the vicinity of Mg/Ti interface has been observed in Figure 3.5 attributing to the discrepancy in lattice parameter between constituents. The in-plane lattice mismatch between Mg ($a_{\text{hcp-Mg}}$ =3.21 Å) and Ti ($a_{\text{hcp-Ti}}$ =2.95 Å) is about 8.6% ($2(a_{\text{hcp-Mg}} - a_{\text{hcp-Ti}})/(a_{\text{hcp-Mg}} + a_{\text{hcp-Ti}})$), and thus refers to a semi-coherent interface, where there is a partial lattice matching accompanied by the formation of misfit dislocations.

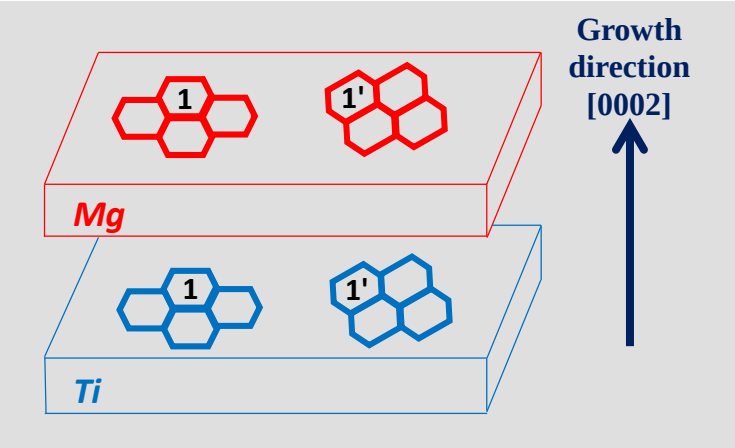

Figure 3.4: A schematic diagram illustrating the difference between OR.1 and OR.1'.

In summary, with a dependence on the individual layer thickness, two major types of orientation relationship have been identified in the Mg/Ti multilayered nanofilms. For very small individual layer thickness ($h \leq 2.5$ nm), inter-epitaxial deposition between Ti and Mg matching the basal plane is the prevalent growth mode in spite of the relatively large lattice mismatch between Mg and Ti, resulting in an orientation relationship of Mg $\{0002\}$ // Ti $\{0002\}$ and Mg $<01\bar{1}0>$ // Ti $<01\bar{1}0>$ (or Mg $<2\bar{1}\bar{1}0>$ // Ti $<2\bar{1}\bar{1}0>$ with in-plane rotation of crystals). When the individual layer thickness is increased, another orientation relationship, Mg $\{0002\}$ // Ti $\{01\bar{1}0\}$ and Mg $<2\bar{1}\bar{1}0>$ // Ti $<0001>$ starts to emerge, presumably to accommodate the internal stress in the films.

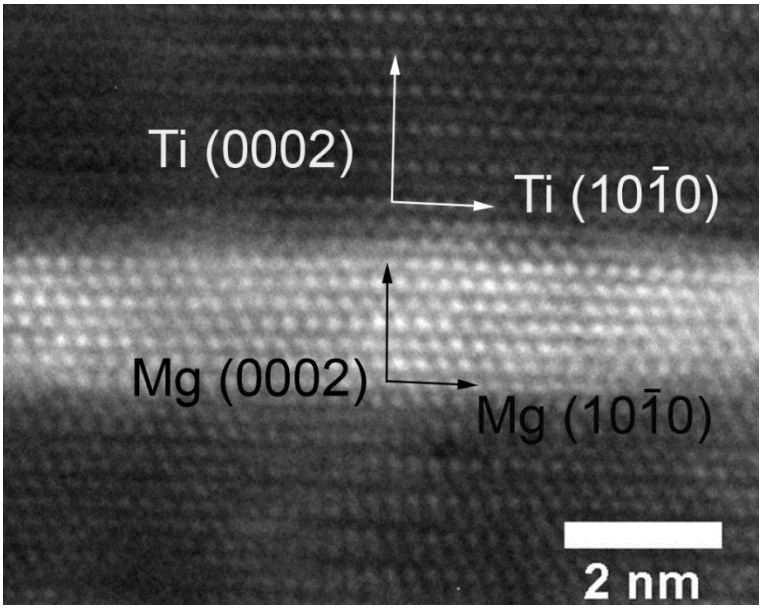

Figure 3.5: A high-resolution TEM image of the Mg and Ti layers of the multilayer specimen with h=2.5 nm, showing epitaxial growth between Mg and Ti.

3.2 Mechanical Properties

From the instrumented nanoindentation experiments following the methods of Oliver and Pharr [184], we obtained the Young's modulus *E* and average hardness *H* of the as-deposited Mg/Ti multilayered nanofilms. We have found that, regardless of the various individual layer thicknesses, the measured Young's modulus are consistently in the range of 78 6 GPa. Considering the room temperature Young's moduli of pure Mg and α-Ti are 44 and 116 GPa, respectively, this result suggests that the "rule of mixture" applies to the Young's modulus of the Mg/Ti multilayers. Namely, the Young's modulus of the multilayer specimen is the weighted mean of the Young's moduli of the constituent components.

The hardness of Mg/Ti multilayers exhibits an obvious increasing trend as the individual layer thickness decreases. Figure 3.6 displays the nano-hardness results of the Mg/Ti multilayers. We can see that the maximum hardness with a magnitude of ~4.2 GPa is obtained in the Mg/Ti multilayer specimen possessing an individual layer thickness of 2.5 nm. To provide a more straightforward illustration of the deformation mechanisms in these HCP/HCP multilayers that we will revisit in the next section, we have plotted the flow strength σ (hardness H divided by a Tabor coefficient of 2.7) as a function of the inverse square-root of the individual layer thickness ($h^{-0.5}$) in Figure 3.6. This plot is reminiscent of strength—layer thickness plots of many other multilayer systems in the literature [71, 72, 74]. In other words, when the individual layer thickness is large ($h \geq 50$ nm), there is a nearly linear effect of $h^{-0.5}$ on strength of the multilayers, following the classical Hall-Petch relation. However, when the individual layer thickness is further reduced, its effect on the specimen strength levels off, until a decrease in strength is

observed, which is popularly called the inverse Hall-Petch effect as observed in bulk nanocrystalline metals [185]. However, a clear trend of inverse Hall-Petch effect cannot be securely established for the Mg/Ti multilayer system since the maximum hardness is obtained at the smallest individual layer thickness (h=2.5 nm). For comparison, in Figure 3.6, the hardness data of Mg/Nb multilayers extracted from the work of Ham and Zhang has also been plotted [80]. We see that the hardness of this heterogeneous system has been surpassed by the homogeneous HCP/HCP system of Mg/Ti.

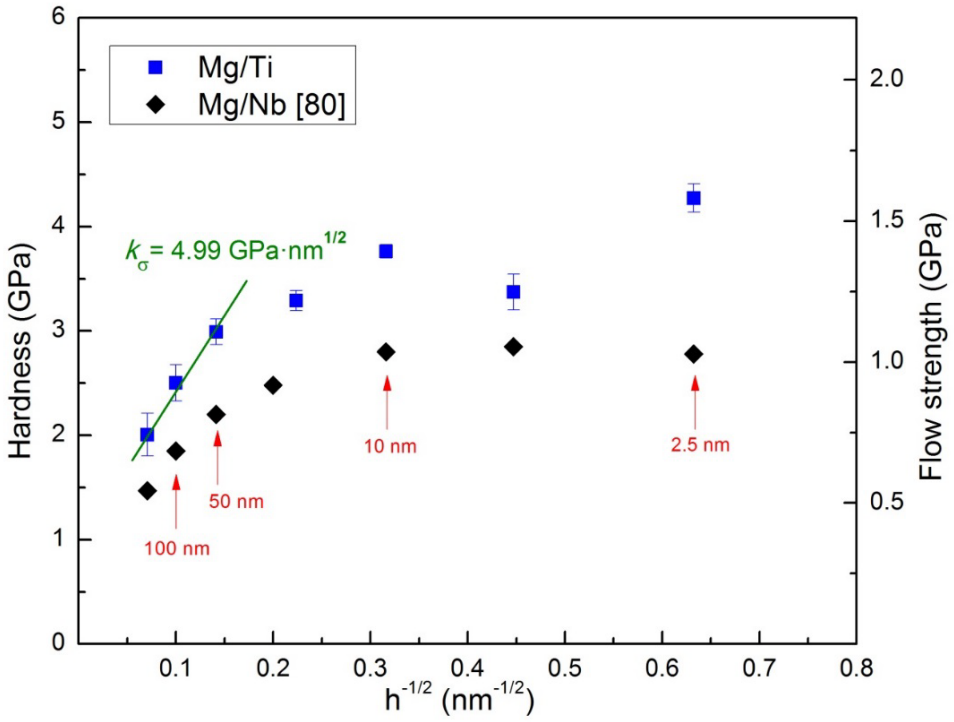

Figure 3.6: The plot of nanoindentation hardness H and flow strength σ as a function of $h^{-0.5}$ for the Mg/Ti multilayer specimens. The experimental data of Mg/Nb multilayered from Ref. [80] has also been plotted for comparison.

In Figure 3.6, a straight line reflecting the Hall-Petch law is sketched out in green to fit the linear relationship of $\sigma \sim h^{-0.5}$. The Hall-Petch slope k_σ is derived to be 4.99

$GPa \cdot nm^{1/2}$. As we have mentioned, with further reduction in the individual layer thickness below 50 nm, the strength of the multilayers continues to increase but the "Hall-Petch slope" has been diminished compared to 4.99 $GPa \cdot nm^{1/2}$. We have also observed a dip in the strength versus $h^{-0.5}$ plot in the small individual thickness regime that occurs at h=5 nm. Afterwards, the strength increase resumes and the maximum flow strength, about 1.56 GPa, is reached in the film with the thinnest individual layers (about 2.5 nm in thickness). The commonly observed plateau of strength or softening at the level of several nanometers has not been detected in this study.

To further examine the strengthening and flow behavior of the Mg/Ti multilayers in nanoscale, we have also performed microcompression experiments on pillars machined from the as-deposited Mg/Ti multilayered nanofilms using FIB. Figure 2.5(b) displays a representative image of such a micro-pillar. To maintain the optimal height: diameter ratio of 2:1 [174], all the Mg/Ti cylinder pillars have an average diameter around 0.5 μm, except the h=200 nm specimens whose total film thickness is larger than others and thus possess a diameter around 2.5 μm. For pillars of such dimensions, tapering becomes an unavoidable issue [186, 187], which may introduce spurious strain hardening according to the work of Zhang and co-workers [174]. However, it will not bring about strong impact on the accuracy of the strength measurement. Since machine and substrate compliance cannot be removed for this non-standard measurement and the strain is based on the apparent displacement of the flat punch recorded by the nanoindentation system, we have not attempted to derive the elastic modulus of the samples.

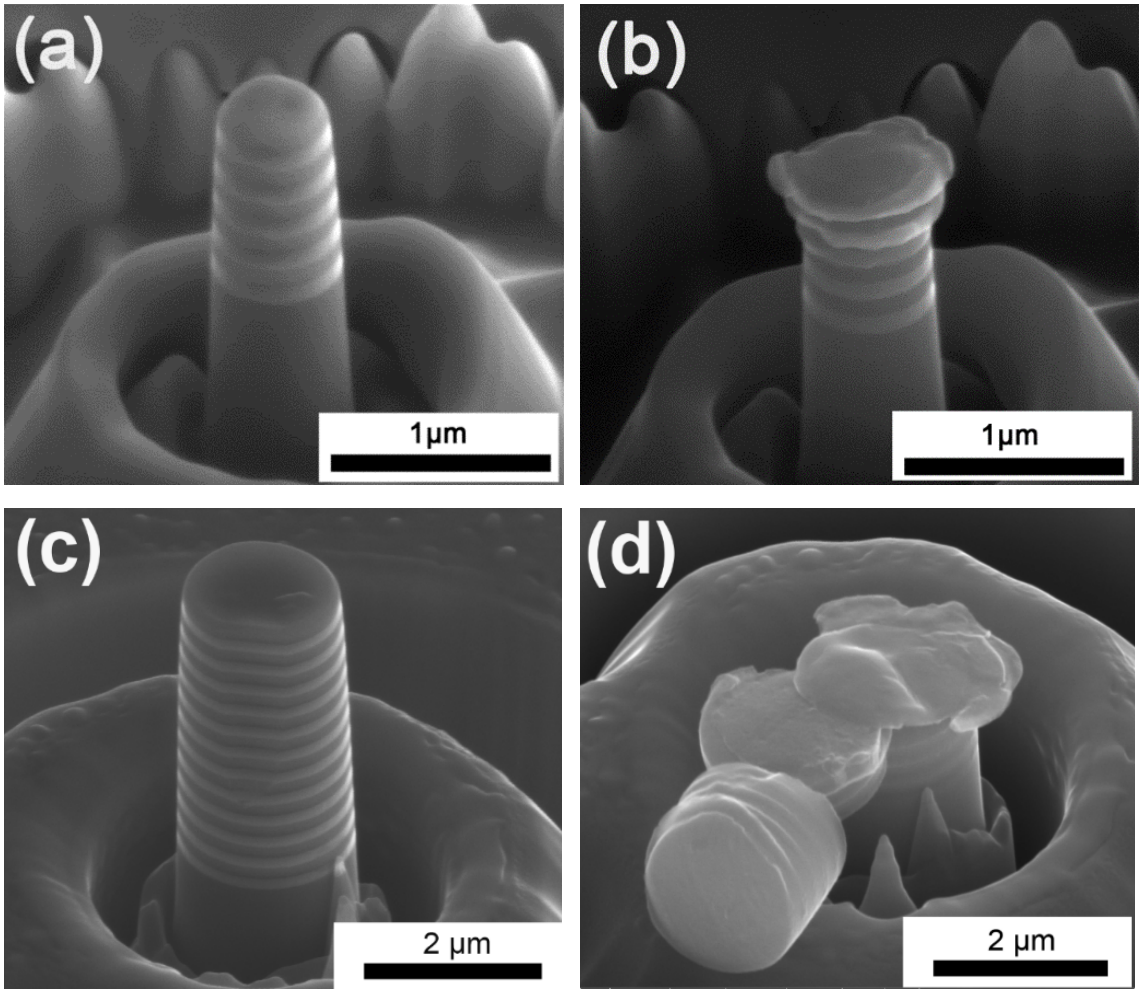

Figure 3.7: The SEM images of an Mg/Ti multilayer pillar with *h*=100 nm before (a) and after (b) uniaxial compression; with *h*=200 nm before (c) and after (d) uniaxial compression.

Figures 3.7(a) and (b) display the SEM images of an Mg/Ti multilayer pillar with individual layer thickness of 100 nm before and after microcompression test, respectively. Since the top layer is always Ti, the layer with brighter contrast in the images is Mg. The post-loading image (Figure 3.7(b)) suggests that under compression, plastic deformation proceeds from the pillar top. Moreover, we can see the soft Mg layers, especially the top ones, have been extruded out whereas the Ti layers are not heavily deformed. Similar deformation morphology has been observed in the multilayer pillars with *h*=20, 50, 200

nm. The dominating role of Mg in the plastic deformation of these specimens is thus inferred. Figure 3.8 demonstrates the representative true stress-strain curves derived from their straightforward microcompression load-displacement results. The dot lines on the right side of the figure designate the nanoindentation measured flow strength (σ_i), which is calculated by dividing hardness *H* with a factor of 2.7 (Tabor's law). We can see, at sub-micron scale *h*, σ_i agrees well with the maximum flow stress achieved in the microcompression experiments (σ_m), as evidenced by the discrepancy less than 0.1 GPa. The detailed σ_i and σ_m values of Mg/Ti multilayer films are summarized in Table 3. A further compressive loading on the Mg/Ti micropillars with $h \geq 50$ nm induces conspicuous shearing out of constituent layers and eventual collapse. Figure 3.8(d) shows the post-loading image of an h=200nm Mg/Ti pillar subject to a strain of 30%, in which the trace of unstable shearing failure is obvious. It is also worth noting that there is no shear band found on the deformed pillars at this size level ($h \geq 50$ nm).

Figure 3.9 gives an example of pre-loading ((a)) and post-loading ((b)) images of Mg/Ti multilayers where h=2.5 nm. Due to the extremely small *h*, the individual layers cannot be distinguished from the image. However, the boundary between the multilayer and the silicon substrate can still be observed. The plastic deformation of h=5 nm multilayer pillars is analogous to h=2.5 nm ones, as illustrated in Figure 3.10. In these micropillars characterized with nanoscale *h*, although several small cracks emerged at the edge of deformed portion (the arrows in Figure 3.9(b) and (d)), no fracture was discerned even up to a true strain of ~25%. Again, since the Mg and Ti layers become extremely thin, it is very difficult to tell whether Mg extrudes at first, merely from the ex-situ examination of deformed pillars. Nevertheless, the absence of shearing failure (refer to Figure 3.7(d))

confirms the deformation mechanism of Mg/Ti metallic multilayers depends on the length scale of individual layer thickness. While we can expect the increase of interface area accompanied with decreasing *h* partially accounts for the enhanced constraints on Mg layers from shearing out, the alteration of crystallographic relationship between Ti and Mg is probably another reason for the transition of deformation modes in Mg/Ti multilayers and we will discuss it later. Interestingly, the catastrophic shear band found in Cu/Nb [67], Al/Nb [68] and Cu/Zr [188] multilayer micropillars at this intrinsic size level does not appear here, implying the homogeneous plastic deformation in our nanostructured HCP-based multilayers (Mg/Ti).

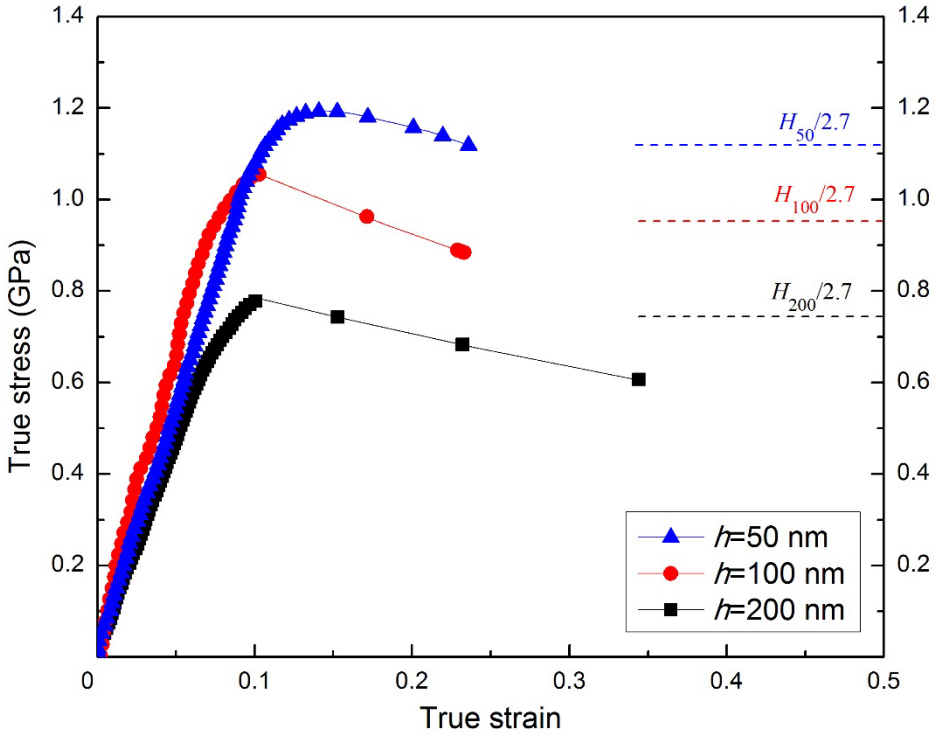

Figure 3.8: True stress-strain curves of the Mg/Ti multilayer specimens with *h*=50, 100 and 200 nm, respectively.

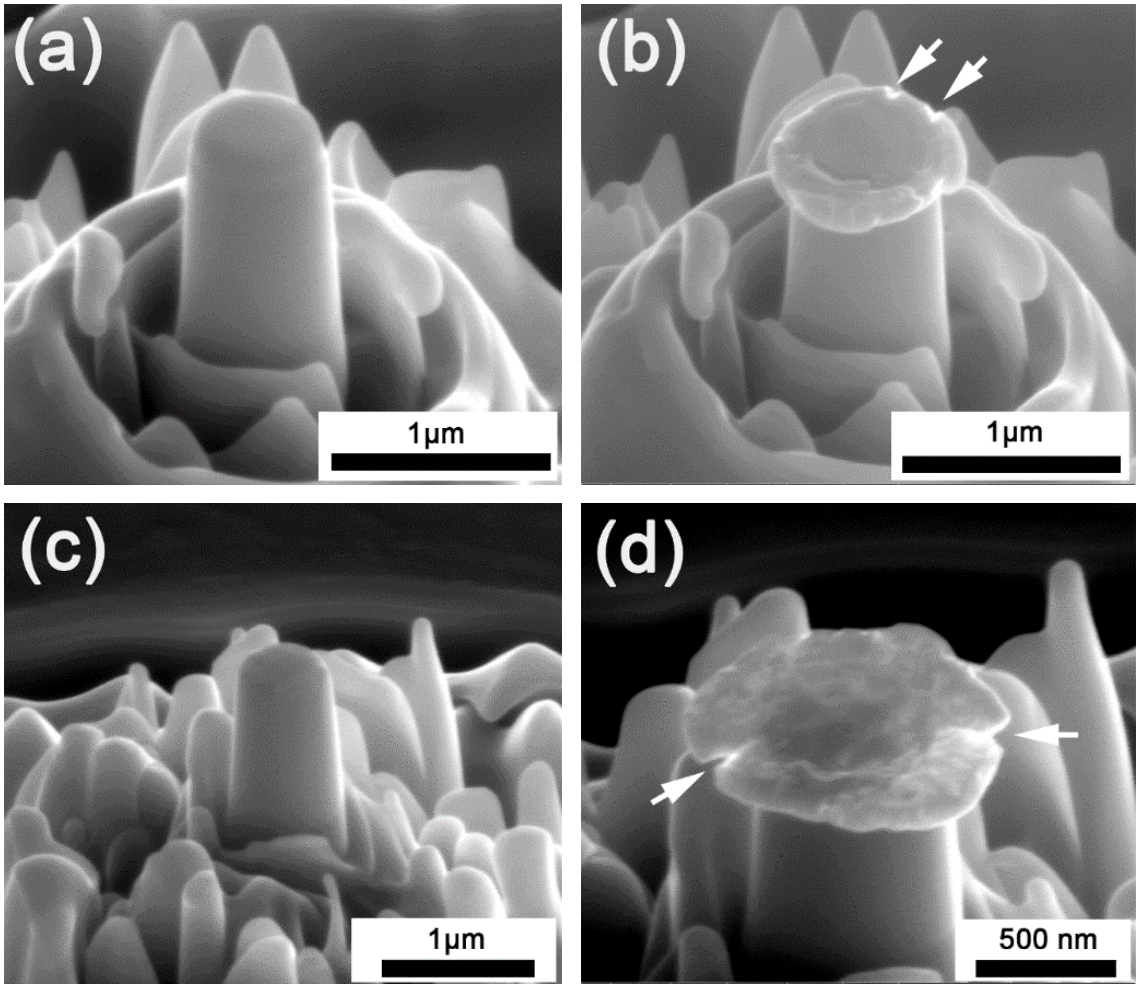

Figure 3.9: The SEM images of an Mg/Ti multilayer micropillar with *h*=2.5 nm before (a) and after (b) uniaxial compression; *h*=5 nm before (c) and after (d) uniaxial compression.

Table 4: The nanoindentation-measured and microcompression-measured flow strength of Mg/Ti metallic multilayers with various individual layer thicknesses.

Individual layer thickness *h*, nm	Nanoindentation measured hardness *H*, GPa [16]	Nanoindentation measured flow strength σ_i (=*H*/2.7), GPa	Microcompression measured flow strength σ_m, GPa
200	2.01	0.74	0.78
100	2.57	0.95	1.05
50	2.99	1.11	1.19
20	3.29	1.22	1.12
10	3.76	1.39	1.42
5	3.40	1.26	2.04
2.5	4.21	1.56	2.35

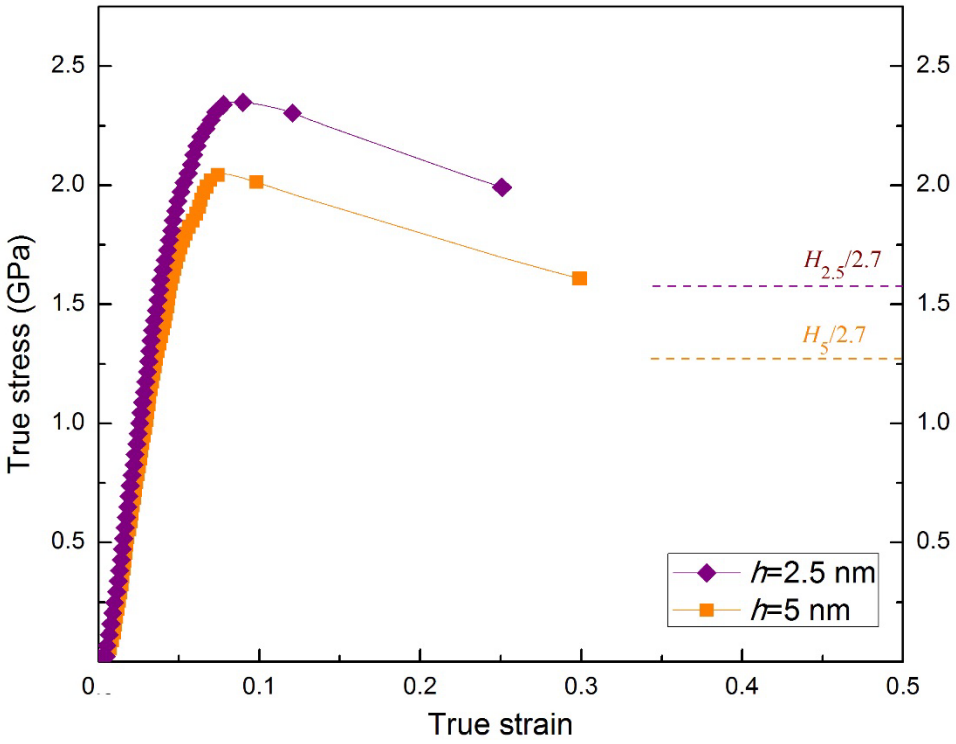

Figure 3.10: True stress-strain curves of the Mg/Ti multilayer specimens with *h*=2.5 and 5 nm, respectively.

In addition to the change of deformation morphology, the influence of *h* on the mechanical response of Mg/Ti multilayer micropillars is also reflected through the breakdown of aforementioned consistency between nanoindentation and microcompression experiments in measuring flow strength. Figure 3.10 presents the representative true stress-strain curves of *h*=2.5 and 5 nm Mg/Ti multilayer pillars. We can see, σ_m is now considerably larger than σ_i (=*H*/2.7). As summarized in Table 4, the maximum flow strength of Mg/Ti multilayers measured by nanoindetation is ~1.56 GPa while the counterpart from microcompression is ~2.35 GPa. Both of them are achieved at *h*=2.5 nm. In following discussion section, we will give an explicit interpretation about

such a discrepancy on strength evaluation that might be a unique character for HCP-based multilayer nanofilms.

Learned from the true stress-strain curves in Figure 3.8 and 3.9, the Mg/Ti multilayer micropillars exhibit a general trend of strain softening beyond the strain of ~10%, regardless of the individual layer thickness. However, the mechanisms responsible for the lack of strain hardening ability might vary with the size level of *h*.

Finally, we present the strain rate sensitivity results of the Mg/Ti multilayer samples based on instrumented nanoindentation experiments at different loading rates. The strain rate sensitivity of each specimen was calculated using Equation (20), while the activation volume was derived from Equation (21). Figure 3.11 shows the $\ln H$ *vs.* $\ln \dot{\varepsilon}$ plots of various Mg/Ti multilayer specimens. We can see that all the data points fall onto the respective straight lines. According to Equation (20), the slope of each straight line is the SRS of the corresponding specimen. The measured values of SRS (m) and activation volume (V^*) of various specimens are listed in Table 5. The values of m for the as-deposited Mg/Ti multilayers are exclusively falling in the range of 0.038—0.053 and in turn the activation volumes V^* are in the range of 3.7—8.0 b^3 (b is the magnitude of the Burgers vector). However, according to the results, it is quite difficult to extract a straightforward and clear trend of m, V^* with respect to the individual layer thickness h, as that reported for Cu/Cr and Cu/Zr multilayers by Niu and coworkers [114]. Neither can a definitive relation between SRS, V^*, and h be established for these Mg/Ti multilayer specimens in a way similar to the relationship between SRS and grain size d for bulk FCC and BCC metals [177]. If we compare the SRS data of Mg/Ti multilayered nanofilms with those of the monolithic constituents [189-193] as shown in Table 6, no clear correlation can be

identified either. We can see that the strength of Mg/Ti multilayers is not as sensitive to the strain rate as nanocrystalline Mg, even when the layer thickness *h* is approaching to the grain size *d* (*m*=0.0524 at *h*=50 nm of this work *vs.* *m*=0.6 at *d*=45 nm from Ref. [191]). Unlike the remarkable change of SRS with grain size in pure monolithic Mg, the Mg/Ti multilayers in this study do not show significant change in SRS when *h* is varied. This is also true for the activation volumes as suggested by the data in Table 6.

Table 5: Strain rate sensitivity *m* and activation volume V^* of Mg/Ti multilayered nanofilms with various individual layer thicknesses *h*.

h (nm)	2.5	5	10	20	50	100	200
m	0.0471	0.0387	0.0487	0.0402	0.0524	0.0478	0.0460
V^*	3.713 b^3	5.280 b^3	3.860 b^3	5.515 b^3	4.688 b^3	6.063 b^3	7.978 b^3

Notes: the parameter *b* here indicates the average length of Burgers vector of Mg and Ti.

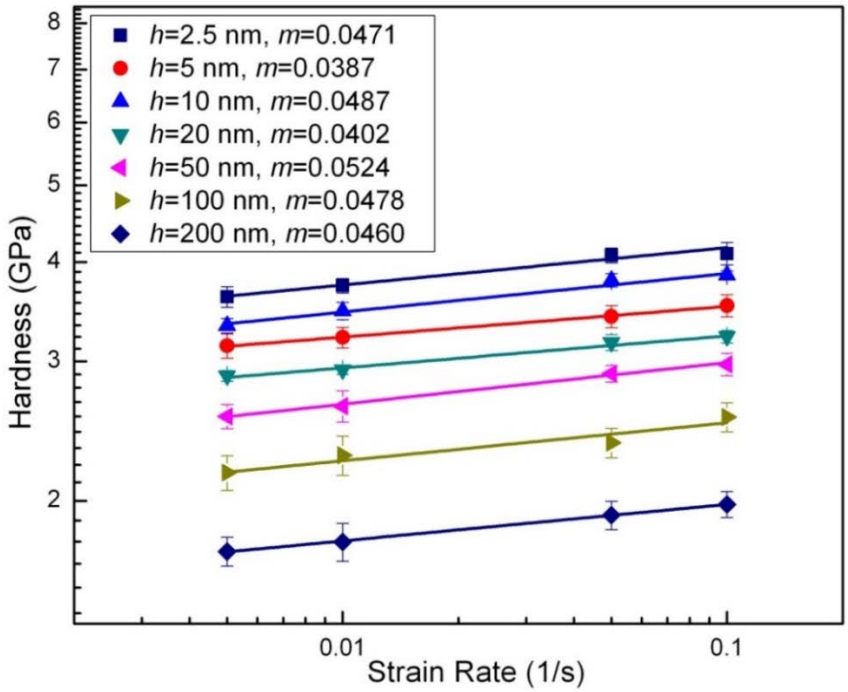

Figure 3.11: Experimental results of strain rate sensitivity (SRS) of the Mg/Ti multilayered specimens with different individual layer thicknesses.

Table 6: The comparison of *m* in Mg/Ti multilayered nanofilms with their constituents.

Material	*m*
Single Crystal Mg [189]	0.041
Polycrystalline Mg with *d*~100 nm [190]	0.31
Polycrystalline Mg with *d*~45 nm [191]	0.6
Polycrystalline Ti with *d*~0.05 mm [192]	0.025
Polycrystalline Ti with *d*~260 nm [193]	0.04
Mg/Ti multilayered nanofilms	0.038-0.053

Notes: *d* is the average grain size.

When people are considering the possible mechanisms behind SRS, the cutting forest dislocation model in the condition of large activation volume or the coble creep and grain boundary sliding models at low activation volume are involved. All of them might have considerably limited effects on the plastic deformation in Mg/Ti multilayered nanofilms due to the scarcity of grains (XRD and TEM) and dislocations. Carpenter once suggested layer interfaces could have the same influences as the grain boundaries to dislocations, e.g. primary sources and sinks, but a further verification is in need to understand the rate controlling process for HCP/HCP multilayers [176].

In summary, we have observed that the hardness of the Mg/Ti multilayer specimens follows the conventional Hall-Petch relation for $h \geq 50$ nm. The Hall-Petch strengthening levels off at smaller individual layer thickness. A dip in the hardness—$h^{-0.5}$ curve is observed at h=5 nm. However, with further decrease in h, the hardness starts to increase again, and the highest hardness is obtained at the smallest h (2.5 nm) of this work. Microcompression experiments results also indicate the layer thickness-flow strength relation of Mg/Ti multilayers follows the “smaller is stronger” pattern. However, the flow strength measured by microcompression deviates from that derived from nanoindentation on the basis of Tabor’s law. Strain softening is prevalent in the Mg/Ti micropillars at all

length scales of *h*. No certain trend has been established for the strain rate sensitivity but the activation volume is smaller than 10 b^3 for all the specimens.

3.3 Discussions

3.3.1 Microstructural Evolution of Mg/Ti Multilayers

In addition to the significant difference in melting points between Mg and Ti ($T_{m\text{-}Mg}$=923K *vs.* $T_{m\text{-}Ti}$=1943K), these two metals have very limited solubility (~2 at.%) to each other. The enthalpy of mixing between Mg and Ti is positive, and that is why it is understandable that no intermetallic compounds has been found between Ti and Mg from the phase diagram (Figure 1.11) of this binary system [194]. This also means that at equilibrium, the inter-diffusivity between Ti and Mg is vanishingly small [195]. Therefore, it should be extremely difficult to combine them together to form an alloy by regular preparing techniques. Asano et al. [196] reported the synthesis of Mg_xTi_{100-x} alloys by milling Mg and Ti powders for 50-200 hours. They found that a high content of metastable phases with body-centered cubic or face-centered cubic structure had been introduced into these far-from equilibrium alloys. Although in the work of Asano et al. the crystallite size of the ball-milled Mg_xTi_{100-x} non-equilibrium alloys had been reduced to ~10 nm, further reduction in grain size with uniform grain size distribution had been proved to be out of the question. In contrast, the deposition of Mg and Ti by magnetron sputtering reported in the present work offers an effective way to produce Mg-Ti composites with high thermal stabilities as well as accurate controls of specimen size. The very limited inter-mixing between Ti and Mg adds one more advantage in that we should expect clean Mg/Ti interfaces, which simplifies the problem and allows us to explore the dislocation mechanisms responsible for the strengthening effects as a function of individual layer

thickness. The thermal and structural stability of Mg and Ti in the multilayers renders this binary system a good model system for the study of the microstructure and mechanical properties of HCP/HCP multilayered nanofilms.

Based on our XRD and TEM experimental results, there are three features worth noting about the microstructure of this typical HCP-based (Mg/Ti) multilayered nanofilm. First, no phase transformation or induced change of lattice type has been detected in Mg/Ti multilayers. For nanostructured multilayers made up of metallic constituents with different atomic configurations at interface, one component is prone to transfer into the same crystal structure as another to accommodate the significant lattice mismatch introduced. This phenomenon has been widely observed [113], especially when HCP metals are involved. For instance, a metastable Mg with BCC structure was reported by Ham et al. in the sputter-deposited Mg/Nb multilayers with individual layer thickness of 5 nm or less [80]. Similarly, Zr has also been found undergoing HCP-to-BCC structural transition during the room-temperature deposition process of Nb/Zr multilayered thin films, as described in Lowe's work [197]. The Mg/Ti multilayer system in this study, however, keeps HCP crystal structure at various length scales of layers which is attributed to the identical lattice type of both constituents.

Second, in contrast to most reported metallic multilayer systems, there is more than one orientation relationship identified between the layer constituents in Mg/Ti multilayered nanofilms when h>2.5 nm. According to the literature, FCC/BCC multilayered thin films generally follow the Kurdjumov-Sachs (K-S) orientation relationship [11, 68], in addition to occasional observation of the Nishiyama-Wasserman (N-W) relationship [198]. The FCC/FCC multilayers are featured by cubic-on-cubic crystallographic relationship

commonly with (111) fiber texture, of which Cu/Ag, Ag/Ni and Cu/330 stainless steel are examples [74, 76, 79]. Consider that Mg and Ti are both HCP metals with a moderate lattice parameter mismatch between them, the HCP-on-HCP orientation (OR.1) should be favored for Mg/Ti multilayers. Moreover, the smaller lattice mismatch of OR.1 (8.6% misfit), compared to that of OR.2 (37.3% misfit), brings about the energetic advantages of OR.1 because the elastic strain energy of interface increases with the lattice mismatch. The prevalence of (0002) texture and OR.1 in Mg/Ti multilayered nanofilms is thus understandable. For Mg-Ti composites, the predominant paralleling growth pattern between Mg and Ti crystals along (0002) orientation as observed in this work is not unique. Zheng and co-workers have also observed it in the vapor quenched Ti-29wt% Mg alloy [199]. For now we invoke the work of Wei and Misra [200], who observed layer curvature manifested as the wavy morphology of the layers. Such curved layers may disrupt the orientation relationship such as OR.2 identified here with relatively large *h*. However, the formation of layer curvature is a complicate dynamic process influenced by thermal equilibrium during deposition, growth defects, surface diffusion, and so on. It is therefore difficult to accurately predict the growth mechanisms of the Mg/Ti multilayers.

Third, the moderate lattice mismatch between HCP Ti and Mg indicates that the interface of the Mg/Ti multilayers should be semi-coherent at best. At the Ti/Mg interface, dis-registry of atoms can be periodically taken up by misfit dislocations. It is well known that the interface characteristics play a vital role in the deformation mechanisms of multilayered materials. The effects of partially relieved coherency strain and misfit dislocations at the Mg/Ti interface on the mechanical behavior of Mg/Ti multilayers will be discussed with details in the following section.

We should point out that the epitaxial growth between the Ti and the Mg layers needs further elaboration because of the relatively large lattice mismatch between the two HCP metals. The degree of epitaxy depends on a number of factors. As such a critical thickness can be derived for different systems. In the Mg/Ti heterogeneous system, we can use the following formula to estimate the critical thickness h_{cr} of epitaxial growth [129, 201, 202],

$$h_{cr} = \frac{b}{2\pi\varepsilon_m} \ln\left(\frac{\sqrt{2}h_{cr}}{b}\right) \tag{22}$$

where *b* is the length of Burgers vector and ε_m is the misfit strain of the film. The physical meaning of h_{cr} is that it gives the theoretical critical thickness for the formation of misfit dislocations to relax the misfit strains. When h_{cr} is too small, the energy from the constrained layers will be insufficient to provide the energy required to form the misfit dislocations.

Here, we assume only dislocations with ***a***-type Burgers vector are operating, and $\vec{b} = 1/3 < 11\bar{2}0 >$ while the misfit strain is 8.6%. According to Equation (22), the stable critical thickness of Mg/Ti epitaxial growth is only 0.6 nm and comparable to several atomic monolayers. In other words, the appearance of misfit dislocations is inevitable in our as-deposited Mg/Ti multilayered nanofilms to accommodate the large lattice mismatch. The distance *s* between adjacent misfit dislocations is

$$s = \frac{b}{\varepsilon_m} \tag{23}$$

For Mg/Ti multilayers, $s_{\text{Mg-Ti}}$ is about 3.55 nm. It agrees well with the HRTEM image of 2.5 nm Mg/ 2.5nm Ti specimen (Figure 3.5), where perfect epitaxial growth can be clearly seen in the Mg/Ti interfacial region with a width of at least 3.0 nm.

As suggested by Matthews [203], in practice, the critical thickness h_{cr} for epitaxial growth could be pretty larger than the value calculated by Equation (22) since other strain relaxing factors such as the elastic strain in the lattices or difficulties associated with the formation of misfit dislocations are involved. Taking the shearing taking place in the first two Ti atomic layers deposited right above Mg for example, these stacking-fault-alike distortions as shown in Figure 3.5 could be responsible for relaxing strains of the films to a certain level and potentially extend the critical thickness for epitaxial growth.

When h is large, other orientation relationships such as OR.2 start to evolve. Based on this relationship, it is realized that the Ti crystals orient themselves with the dominant slip plane Ti $\{01\bar{1}0\}$ paralleling to Mg $\{0002\}$ which is the dominant slip plane of Mg at the interface, as h is increased. By reducing the angle between the dislocation glide plane and the interface, this kind of arrangement is favored for the dislocations to glide across the interface and consequently weakens the strengthening effects from the interface barriers. It is energetically favorable for OR.2 to emerge when h is large enough, while a smaller length scale of the layer thickness might restrict this transformation and keep the epitaxial growth. It is at least a possible explanation for the appearance of OR.2. However, other fundamental mechanisms for its presence need further elaboration. For example, the entropic reasons or strain energy reduction at large h should be carefully examined to show the effect, or the lack thereof.

3.3.2 The Influence of Individual Layer Thickness on Strength

First of all, one can easily notice that the Mg/Ti multilayered nanofilms exhibit much higher strength than the bulk counterpart of their constituents. For example, the ultimate tensile strength of pure Ti is about 550 MPa [204], about one third of the maximum strength obtained from our Mg/Ti nanofilms. Even cryo-milled commercial purity titanium with a high content of impurity atoms has a yield strength only at the level of ~900 MPa [205]. As a matter of fact, the strength of the Mg/Ti multilayer films with fine lamellar structure is so impressive that it even surpasses the strong commercial Ti-6Al-4V alloy (yield strength ~880 MPa). This is even more so if we look at the micro-compression results. As for pure magnesium, the yield and ultimate tensile strength values in the sand-cast condition are only ~21 MPa and ~90 MPa, respectively [125, 206]. Considering these factors, we believe it is necessary to provide an in-depth discussion about the extraordinarily high strength observed in the Mg/Ti multilayers.

The semi-coherent interface between the two HCP metals is partly responsible for the high strength of these Mg/Ti multilayered nanofilms, especially when we make comparison with the mechanical properties of sputter-deposited Mg/Nb multilayer films reported by Ham, et al. [80] (the Mg/Nb results are also plotted in Figure 3.6 for comparison). The measured peak hardness of the Mg/Nb system is only ~2.8 GPa, which is also achieved at h=2.5 nm, much lower than the hardness of ~4.2 GPa of the Mg/Ti multilayer specimen with the same h. Meanwhile, the measured Hall-Petch slope of the Mg/Nb system is slightly smaller than that of the Mg/Ti system. Since the Hall-Petch slope represents the strength of interface barrier related to slip transmission, the peak strength of multilayers can be estimated from the measured slope by Equation (4)

$$\tau^* = \frac{k^2\pi(1-\nu)}{\mu b} \tag{4}$$

The value of parameter k in Equation (4) under shear loading is obtained by dividing k_σ with a Taylor factor of ~3.1. Similar to Mg/Nb, the substitution of relevant parameters of Mg into Equation (4) will lead to an overestimation of the strength for the Mg/Ti multilayer composites. Here, we used ν=0.32, μ=44 GPa and b=0.29 nm, all of which are from the stiffer component, Ti, into the equation and obtained τ^*=0.44 GPa. By multiplying τ^* with the Taylor factor back, we can obtain a theoretical estimate of the ultimate peak strength of the Mg/Ti multilayers, ~1.35 GPa, in a reasonable agreement with the experimental peak strength of ~1.56 GPa (see Figure 3.5).

The above estimation of interface boundary strength (IBS) is mainly based on the dislocation pile-up against the interface. We can also attempt to predict the peak strength alternately by considering the intrinsic properties of Mg/Ti interface. As we mentioned in Chapter 1, for metallic multilayers, the dislocation moving from soft layer to hard layer must overcome a repulsive force (so-called image stress or Koehler stress) due to the different shear moduli across the interface. The upper bound of image stress in the Mg/Ti multilayers can be calculated according to Equation (6)

$$\tau_{\text{image}} = \frac{\mu_{\text{Ti}} - \mu_{\text{Mg}}}{\mu_{\text{Ti}} + \mu_{\text{Mg}}} \cdot \frac{\mu_{\text{Mg}} \sin\theta}{8\pi} \tag{6}$$

where θ is the smallest angle between the interface and the glide planes of the crystal and is assumed to be 60° for Mg/Ti multilayers. We can then calculate the image stress to be τ_{image} ~0.26 GPa. In addition, the arrays of misfit dislocations deposited on this semi-coherent interface can also impede the slip transmission of dislocations, which is [103, 116]

$$\tau_{\text{misfit}} = \alpha\mu\left(\xi - \frac{b}{2h}\right) \tag{24}$$

where α is the Saada's constant and approximates 0.5, ξ is the misfit strain (8.6%). At h=2.5 nm, τ_{misfit} is calculated to be 0.19 GPa.

The applied stress required for the glide of dislocations across the interface mainly comes from these two parts, and therefore

$$\sigma_{\text{IBS}} \approx M\left(\tau_{\text{image}} + \tau_{\text{misfit}}\right) \tag{25}$$

The theoretical peak strength for Mg/Ti interface is therefore ~1.40 GPa, in reasonable agreement with the experimental result of ~1.56 GPa. The small discrepancy may be attributed to the coherency stress of the Mg/Ti interface, since the interface might not be thoroughly relaxed. Rao and Hazzledine claimed that the coherency stress is capable of enhancing the Koehler barrier somewhat by changing the elastic constants of constituent components and dislocation core width [116].

We have seen that the Hall-Petch law does give a good fitting to the strength of Mg/Ti multilayered nanofilms scaling with layer thickness when $h \geq 50$ nm. However, it significantly overestimates the flow strength as h is less than 20 nm. The failure of Hall-Petch law in this regime is probably because of the incapability of dislocations pile-up against the layer interface. For example, in the case of double-ended pile-up, there should be at least three dislocations to make the pile-up model valid. However, when h is below 50 nm, the number of dislocations that can survive the tiny space can be vanishing. As a consequence, the plastic deformation of Mg/Ti multilayers at this scale level is mainly mediated by the glide of dislocation loops confined within softer layers. As such, the Orowan bowing mechanism is suggested to describe the strength behavior in terms of

$\sigma \propto \ln\left(h'/b\right)/h'$ [103, 105, 107, 207], where h' is the layer thickness measured parallel to the glide plane and is taken as $2h/\sqrt{3}$, assuming pyramidal slip under indentation. This confined layer slip (CLS) model fits the experimental data well at the vicinity of *h*=20 nm But it a greatly overestimates the flow strength for $h \leq 10$ nm.

Here, we follow a refined CLS model proposed by Misra et al. [71] to better interpret the trend of flow strength with *h* spanning from 2.5 to 20 nm. The stress required to activate this mechanism is given by Equation (3) as

$$\sigma_{\mathrm{CLS}} = M\frac{\mu b}{8\pi h'}\left(\frac{4-\nu}{1-\nu}\right)\left[\ln\frac{\alpha h'}{b}\right] - \frac{f}{h} + \frac{\mu b}{\lambda\left(1-\nu\right)} \tag{3}$$

The first term in Equation (3) represents the normal stress needed to propagate the glide loop trapped between adjacent interfaces. It is directly derived from the original CLS model but includes possible change in dislocation core width. Due to the prevailing HCP-on-HCP orientation in the Mg/Ti multilayers accompanied and basal slip as the dominant slip plane in Mg with its basal plane parallel to the interface, the absorption of glide dislocation will occur at the interface. Instead of a compact core ($\alpha = 1$), an expanded dislocation core is therefore preferred in the case of Mg/Ti interface. The second term in Equation (3) is the blocking strength from the interaction of a single glide dislocation with the dislocations that reside on the interface. In Misra's work, the dislocation segments on the interface are deposited by previous glide loops. Nevertheless, these glide loops could not only create dislocations on the interface but also annihilate the misfit dislocations that has already been formed by the lattice mismatch. As a result, the spacing of the in-plane dislocation segments might be larger than that of misfit dislocations without rearrangements. The last term corresponds to the elastic interface stress which will facilitate the yielding of

multilayers under compression, while f is usually in the range of 2—3 J/m^2. With all the considerations mentioned above, we use α=0.6, f=3 J/m^2 and λ=9 nm. The strength based on the refined CLS model is calculated and presented in Figure 3.12. We see that the refined CLS model provides a good estimate for 2.5≤h≤20 nm.

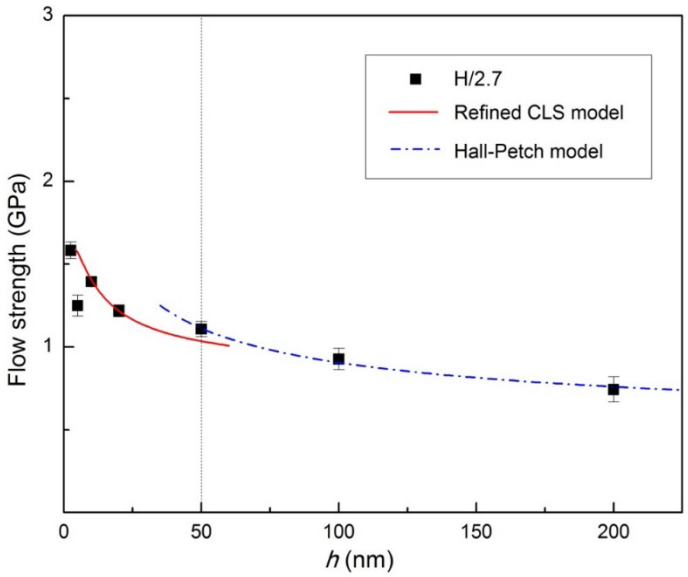

Figure 3.12: The fitting results of the indentation-based flow strength of the Mg/Ti multilayer specimens based on Hall-Petch relation (h≥50 nm) and the confined layer slip (CLS) model (h<50 nm).

Now a few final words about the physical significance of the strain rate sensitivity and activation volumes of the Mg/Ti multilayer specimens. Though not much can be inferred from the experimental results (Figure 3.11 and Table 5) regarding the definite effect of h on those two parameters, the order of magnitude of the activation volumes suggests that some local dislocation activities with small sampling volume (~7b^3) are responsible for the plastic deformation of the films. This is consistent with the above discussion. It is also seen from Table 5 that, particularly when h is relatively large, there is

a trend that the activation volume generally increases with *h*. This is understandable as when *h* is large, the sampling length of the dislocation activities should be large accordingly.

3.3.3 Discrepancy in Strength Measurement

As we have noticed, the Mg/Ti multilayer specimen with the smallest individual layer thickness exhibit a strength level on the order of 2.4 GPa under microcompression. As for Mg/Ti binary system, it should be a reasonable assumption that the shear moduli of the multilayer specimens also follow the rule of mixture. This leads to a shear modulus of these films in the amount of ~30 GPa. Therefore, the *h*=2.5nm multilayer specimen has nearly reached the theoretical or ideal strength of the constituent components combined. This has also been reported in other multilayer systems [20].

According to the nanoindentation and microcompression experimental results (Table 4), σ_m deviates from σ_i (nanoindentation hardness divided with a factor of 2.7) in *h*=2.5 and 5 nm Mg/Ti multilayer specimens. In other words, the Tabor's law, $\sigma_i = H / \kappa$, where κ is commonly in the range of 2.5—3, does not hold for our Mg/Ti multilayers when *h* decreases to several nanometers. This kind of discrepancy was previously reported by Knorr et al. who argued a Tabor factor κ of ~2 would better describe the relation between hardness and flow strength in Cu/PdSi multilayers [208]. Although they inferred the different deformation modes under indentation and compression or residual stress in the multilayers to be the major reasons, a well-established mechanism was not reached.

After examining the deformation morphology of Mg/Ti multilayer pillars, we believe the apparent deviation of σ_m from σ_i occurring at smaller *h* is related to the characteristic plastic anisotropy of HCP structure and the different stress states under flat-

punch and Berkovich tips. To better interpret it, let us first revisit the plastic deformation mechanisms of single crystal titanium and magnesium.

The dominant slip system of single crystal α-Ti is the prismatic slip at relatively low temperatures such as room temperature and below [139, 209-211]. The prismatic slip systems are $<11\bar{2}0>\{10\bar{1}0\}$, with a Burgers vector of $1/3<11\bar{2}0>$. Other secondary slip systems have also been identified such as the basal slip ($<11\bar{2}0>\{0001\}$) and pyramidal slip ($<11\bar{2}0>\{10\bar{1}1\}$), whose Burgers vectors are all the same as $1/3<11\bar{2}0>$. For pure single crystal magnesium, the predominant slip system is the basal slip. It has been found that the critical resolved shear stress (CRSS) for basal, prismatic and pyramidal slips are ≤1.0 MPa, ~50 MPa and ~44 MPa, respectively [126] (and references therein). It has also been reported that the CRSS for twinning in single crystal Mg when loaded along the c-axis is ~90 MPa [212].

The geometry of indenter tip largely determines the distribution of compressive stress onto the tested material. Figure 3.13 schematically illustrates the stress fields in a $[0001]$-oriented HCP crystal compressed by Berkovich and flat-punch tips. The applied stress under a flat-punch tip is always perpendicular to the top surface of tested specimen, as shown in Figure 3.13(a). In contrast, Berkovich tip has a conical shape which generates a spatially radiant stress distribution (Figure 3.13(b)). Under nanoindentation, one should expect that shear and tensile stress components within the layer plane are present [213].

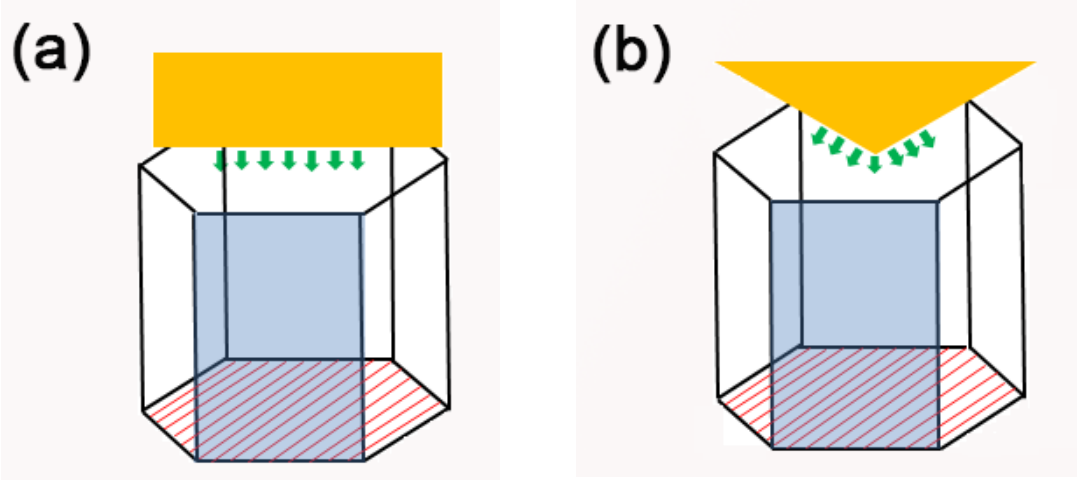

Figure 3.13: Schematic illustrations of the stress state within a [0001]-oriented HCP crystal compressed by (a) flat-punch tip and (b) Berkovich tip.

Our TEM and XRD results of Mg/Ti multilayers have revealed the constituent Mg grows along [0002] direction, aligning the basal plane parallel to the phase interface, regardless of *h*. With such a preferential orientation, the deformation of Mg layers in a perfect microcompression test becomes considerably difficult since there is few resolved shear stress exerted on the easiest operating slip system (vanishing Schmid factor, see Figure 3.13(a)). Whereas the radiant stress distribution under Berkovich tip gives rise to non-zero Schmid factor for basal slip of Mg, as displayed in Figure 3.13(b). As a result, the basal slip should be the dominant slip system of Mg in the nanoindentation tests on Mg/Ti multilayers. As evidenced by the extrusion of Mg in Figure 3.7(b) and eventual shearing failure in Figure 3.7(d), the Mg layers exhibit a strong tendency of rotating and sliding in response to the uniaxial loading on Mg/Ti micropillars with large *h*, which also brings about the dominant role of basal slip in the plasticity of Mg. Given the limited contribution of Ti to the global plastic strain of Mg/Ti multilayer micropillars when $h \geq 20$

nm, the popularity of basal slip in Mg during both nanoindentation and microcompression experiments will produce similar flow stress ($\sigma_m \approx \sigma_i$).

Along with the decrease of *h* to 5 nm or even less, the enlarged interface boundary prevents Mg layers from plastic deforming in advance. On other hand, compared to the two crystallographic relationships existing between Ti and Mg (Mg $\{0002\}$ // Ti $\{0002\}$ and Mg $<01\bar{1}0>$ // Ti $<01\bar{1}0>$; Mg $\{0002\}$ // Ti $\{01\bar{1}0\}$ and Mg $<2\bar{1}\bar{1}0>$ // Ti $<0001>$) in Mg/Ti multilayers with $h \geq 10$ nm, the unified epitaxial growth pattern (Mg $\{0002\}$ // Ti $\{0002\}$ and Mg $<01\bar{1}0>$ // Ti $<01\bar{1}0>$ or Mg $<2\bar{1}\bar{1}0>$ // Ti $<2\bar{1}\bar{1}0>$) at smaller *h* can effectively reduce the lattice mismatching at interface (lower strain energy), and thereby additionally impede the shearing out of Mg layers [214]. For these reasons, Mg and Ti will deform coordinately, to certain extent. Without the sliding and rotation of Mg layers to promote basal slip, other slip systems with larger CRSS, i.e. pyramidal slips, have to initiate in *c*-axis compression experiments and consequently yield a higher flow strength ($\sigma_m > \sigma_i$).

Noting the pillar size usually has insignificant influence on the mechanical properties of nanolayered composites [67, 215], the extrinsic size effects of Mg/Ti metallic multilayers have not been particularly studied in this work. Our *h*=200 Mg/Ti micropillar, the only sample whose dimension is nearly five times larger than other tested micropillars, obeys the consistency of $\sigma_m \approx \sigma_i$ very well, implicitly suggesting the trivial extrinsic size effects involved.

Besides, the contribution of twinning to the plasticity of such an HCP-based multilayer system is not fully understood. We are currently in the progress of trenching TEM specimens from deformed Mg/Ti micropillars to make further investigations. As a

matter of fact, even mechanical twinning has a strong size effect as reported recently by Yu and co-workers [216] on an HCP Ti-Al alloy via micro-compression and in situ nano-compression within a TEM. They observed that when the crystal size is below ~1.0 μm, twinning stops to operate and gives way to dislocation activities, while within the twinning regime, the critical stress needed to drive twinning increases sharply with decreasing pillar size.

3.3.4 Intrinsic Size-dependent Strain Softening

Most pure HCP metals exhibit outstanding strain hardening capability, both in bulk and at small size. For example, a recent work by Byer et al. indicates that the single-crystal Mg micropillars experienced significant stage II and slight stage III hardening when compressed along [0001] *c*-axis [128]. The dislocation interaction and activation of pyramidal slip systems were proposed to account for the increasing stress with strain after yielding. Similar results were obtained by Lilleodden in a parallel study [217].

However, the stress-strain curves of our Mg/Ti multilayer micropillars present a general trend of strain softening beyond the true strain of ~10%, which appears to be independent on the individual layer thickness. Again, according to the deformation morphology of Mg/Ti micropillars, there might be different mechanisms responsible for the softening phenomenon with respect to h. When $h \geq 50$ nm, the strain softening of Mg/Ti multilayers could mainly arise from geometrical effects, e.g. the shearing and rotation of constituent layers, as seen in Figure 3.7(b) and (d). The geometry-induced softening has been observed in Al/Al_3Sc [69] and Cu/Cr [218] multilayers before. The sharply reduced dislocation density within a single layer is likely to be the major reason leading to the deficiency of strain hardening at $h<10$ nm. Given the extremely tiny layer spacing, a

moving dislocation might annihilate at the interface before entangling with other dislocations, similar to the breakdown of dislocation pile-up theory which is commonly seen in the metallic multilayers at this size scale. As mentioned by Han et al. [69], the strain softening is closely related to the mushroom-shaped morphology at the top of the pillar. This is consistent with what we have observed in h=2.5 nm and 5 nm Mg/Ti specimens (Figure 3.9(b) and (d)). For the Mg/Ti multilayers with h spanning from 10 to 50 nm, the two mechanisms probably coexist and compete with each other to bring about the level-off of stress with increasing plastic strain.

Above all, the Mg/Ti multilayered thin films significantly differ from their bulk constituents in mechanical response. Introducing a large density of interfacial area turns out to be a potential way to alter the deformation modes of HCP metals, and therefore improve the strength and hardness.

3.4 Conclusions

In this chapter, we have presented a comprehensive investigation on Mg/Ti multilayer system. The Mg/Ti multilayer specimens were deposited onto single crystal silicon substrates using magnetron sputtering at room temperature with equal individual thickness of the Mg and Ti layers, but the individual thickness ranges from 2.5 nm to 200 nm. Based on the experimental results and discussions, we have reached the following conclusions.

When the individual layer thickness is small, both the XRD and TEM examinations suggest a single orientation relationship between the Mg and Ti layers. This relationship is Mg $\{0002\}$ // Ti $\{0002\}$ and Mg $<01\bar{1}0>$ // Ti $<01\bar{1}0>$ (or Mg $<2\bar{1}\bar{1}0>$ // Ti $<2\bar{1}\bar{1}0>$ with in-plane rotation of crystals). High resolution TEM also indicates inter-

epitaxial relationship between Ti and Mg layers at small individual layer thickness (~2.5 nm). When the individual layer thickness is large, another orientation relationship between Mg and Ti starts to emerge, which is Mg $\{0002\}$ // Ti $\{01\bar{1}0\}$ and Mg $<2\bar{1}\bar{1}0>$ // Ti $<0001>$.

Nanoindentation experiments on the Mg/Ti multilayer specimens show that at relatively large individual layer thickness ($h \geq 50$ nm), the hardness follows the Hall-Petch relation. At relatively small individual layer thickness, the Hall-Petch slope levels off. But a plateau has never been reached. The maximum hardness is obtained at the smallest individual layer thickness (h=2.5 nm). The flow strength of the multilayer specimens with $2.5 \leq h \leq 20$ nm can be predicted quite well by the confined layer slip (CLS) model.

There exists consistency between nanoindentation and microcompression experiments in measuring the flow strength of Mg/Ti multilayer specimens when h is about a few tens of nanometers or larger. However, when h decreases to several nanometers, the flow strength obtained from microcompression is much higher than that derived based on nanoindentation. The discrepancy between the indentation strength and the microcompression strength can be explained by the nearly vanishing Schmid factors of all the fundamental slip systems of both Mg and Ti layers under uniaxial compressive loading. No shear bands have been observed in the microcompression experiments. It appears that under uniaxial compression, plastic deformation proceeds from the top of the pillars. The Mg/Ti micropillars exhibit strain softening which is largely independent of individual layer thickness.

CHAPTER 4: ANNEALED MAGNESIUM/TITANIUM MULTILAYERED NANOFILMS

The impressive high strength of as-deposited multilayered nanofilms has always been the focus of research. However, their thermal stability, which indicates the capability of retaining microstructural and mechanical integrity at elevated temperatures, has not received equal attention. At least moderate thermal stability is what the industrial environment generally requires for the performance of thin films. Thus a full understanding of the microstructure and mechanical properties of Mg/Ti multilayered nanofilms after annealing is critical. Before investigating the effects of annealing temperature and time on Mg/Ti multilayers, we will give a brief review of previous works on the thermal stability of metallic multilayer films.

Heating treatments were usually performed to trigger specific reactions between original elements of metallic multilayers while the intermetallic or amorphous product would serve as a final constituent. For example, Weihs and coworkers used highly pure Cu and Zr to prepare Cu/amorphous Cu-Zr and Cu/$Cu_{51}Zr_{14}$ multilayers by monitoring the heating temperature of differential scanning calorimetry (DSC) [219]. Nevertheless, the unexpected formation of new phases is commonly deemed as an evidence of poor thermal stability because they are likely to bring about the disintegration of lamellar microstructure and sometimes the obvious degeneration of mechanical performance [220, 221]. The inter-diffusion phenomenon that has been detected in many miscible multilayer systems at high

temperatures could cause the same problems and therefore impair the thermal stability [222-225]. A study from Kucharska et al. revealed the appearance of surface discontinuities in the Cu (2 nm)/Ni (1.8 nm) multilayer annealed at 220 °C. With further increase of temperature, intensive delamination of this multilayer sample from the silicon substrate occurred [222].

For polycrystalline metallic multilayers, the increasing temperature often induces grain growth within individual layers. It was reported that the hardness of electro-deposited Cu/Ag multilayer films dropped significantly after a 150˚C anneal due to the spheroidization of grains [226]. Similarly, the coarsening of in-plane grains and the resultant strength loss have been observed in annealed Ni/Ru films with periodicity larger than 36 nm. Misra et al., however, declaimed that the multilayer spheroidization and pinch-off are more likely to take place in annealed Cu/Nb multilayers with small individual layer thickness (~15 nm), compared to those with h>35 nm. They attributed the excellent thermal stability of the films containing thicker Cu and Nb layers (up to 700 °C) to the development of zig-zag alignments of triple junctions, which effectively stabilized the lamellar microstructure. With regard to the varying individual layer thickness, the effect of heating on the morphological stability of metallic multilayers is much more complex than expected. In addition to the change of mechanical properties as mentioned above, the magnetic, optical and electrical properties of multilayers might also be affected by the elevated temperature.

Here the microstructure and mechanical behavior of Mg/Ti multilayers annealed over the temperature from 50 to 200 °C are of our particular interest. For such an HCP-based multilayer system, there are two features worth noting: (1) Mg and Ti are immiscible;

(2) the individual layers of as-deposited Mg/Ti films are highly textured. In what follows, the XRD spectrum of annealed Mg/Ti multilayer specimens will be analyzed at first to determine the involved phases and existence of preferential orientations, and then we will examine the retention of lamellar microstructure in these annealed multilayers by using TEM and HRTEM. Finally, their mechanical properties which are mainly evaluated via nanoindention, will be studied as a function of *h*.

4.1 Crystallography and Microstructure

Figure 4.1 demonstrates the X-ray diffraction results of Mg/Ti multilayers annealed at 200 °C for 2 h. As shown, Mg and Ti layers are still highly textured along *c*-axis after annealing, with a small amount of Ti $(10\bar{1}0)$ reflections at larger *h*. By comparison to the XRD spectra of the as-deposited Mg/Ti multilayers (Figure 3.1), the characteristic peaks move toward larger θ direction slightly. We measured the angle shift for each film and calculated the strain to be ~0.25%, close to the thermal strain $\Delta\alpha\Delta T$ at 200°C as given in Table 7, where $\Delta\alpha$ is the difference in thermal expansion coefficients between Mg and Ti. Thus the thermal expansion could be the predominant factor responsible for the deviation of reflections in annealed Mg/Ti specimens. However, the resultant thermal stress is pretty small with respect to the high strength of Mg/Ti multilayers and somewhat negligible. Consistent with that in the as-deposited Mg/Ti multilayers, the satellite peaks start appearing symmetrically around the Bragg peaks in Figure 4.1 when *h* decreases to 20 nm. The calculation following Equation (9) demonstrates that there is no significant difference in bilayer thickness between the as-deposited and the annealed specimens. In other words, Mg/Ti multilayered nanofilms exhibit excellent capacity in maintaining the

crystallography and lamellar microstructure over the range of annealing temperature from 50 to 200 °C and annealing time from 30 min to 2 h.

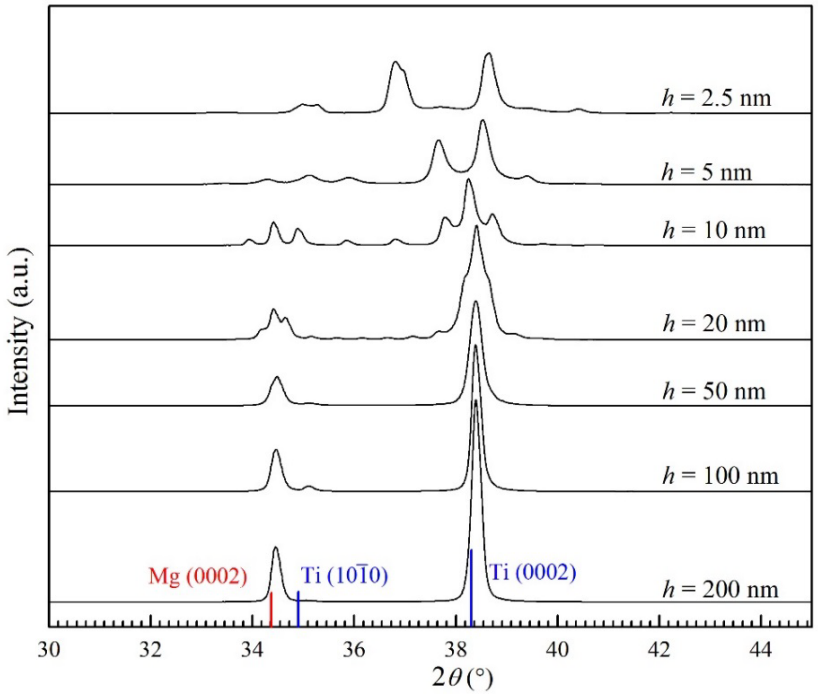

Figure 4.1: XRD patterns of the Mg/Ti multilayer nanofilms annealed at 200 °C for 2 h.

XRD patterns of *h*=2.5 nm Mg/Ti multilayers after annealing at various temperatures are displayed in Figure 4.2. It is interesting to see that, for the annealed specimens, the characteristic peak of Mg splits, suggesting that possible phase transformation of Mg might have taken place. Although both Mg and Ti are well known for their sensitivity to oxygen, no distinguished reflections of magnesia or titania (e.g. MgO (200) at ~44° and TiO_2 (004) at ~37°) have been detected from the XRD spectra. Our home-made annealing instrument is proved to be effective in annealing Mg/Ti multilayers. It might be argued that the annealing temperature of 200 °C is not high enough to test the thermal stability of Ti-based composites. Nevertheless, 200 °C approaches half of the

melting point of pure Mg in absolute temperature (473 K vs 923 K), which is able to induce substantial atomic diffusion in Mg layers.

Table 7: The thermal strain in Mg/Ti multilayers annealed at various temperatures.

Annealing temperature (°C)	Thermal strain between Mg and Ti (%)
50	0.04
100	0.12
150	0.20
200	0.28

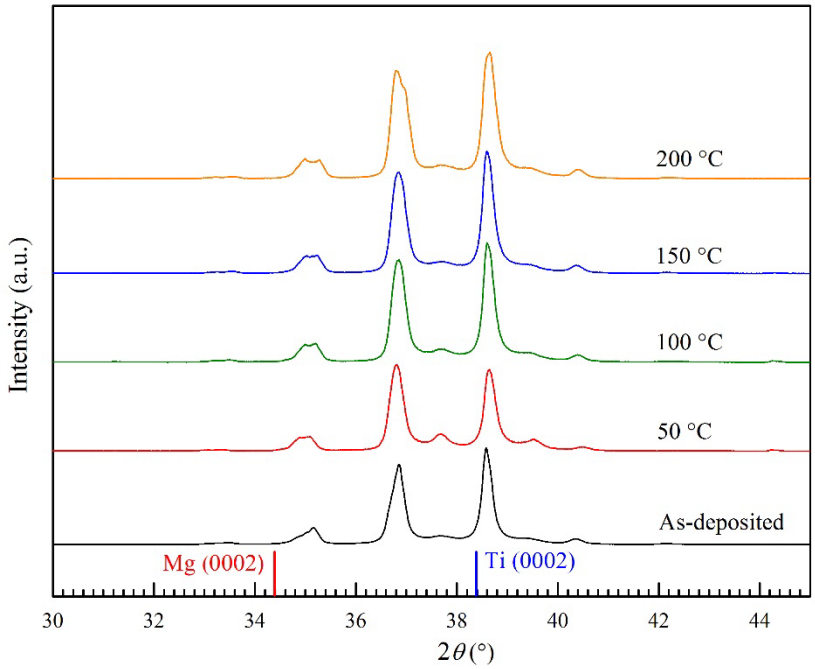

Figure 4.2: XRD patterns of as-deposited and annealed Mg/Ti multilayered nanofilms with h=2.5 nm.

The cross-sectional microstructure of the h=20 nm Mg/Ti multilayer following annealing at 200 °C for 2 h is shown via a bright-field TEM image in Figure 4.3(a). As evidenced by the sharp and continuous interface, Mg and Ti layers are relatively intact, without any pinch-off or breakdown that are frequently observed in polycrystalline multilayers at elevated temperatures. In addition to the predominant epitaxial growth of

Mg and Ti in this *h*=20 nm annealed specimen, the OR.2 (Mg $\{0002\}$ // Ti $\{01\bar{1}0\}$ and Mg $<2\bar{1}\bar{1}0>$ // Ti $<0001>$ as described in Chapter 3) has also been detected, with the corresponding diffraction pattern illustrated in Figure 4.3(b). Again, the experimental results of crystallography and microstructure obtained from TEM agree well with those derived from XRD for our annealed Mg/Ti multilayers.

In contrast to the well-ordered lamellar microstructure of annealed *h*=20 nm Mg/Ti multilayer, the columnar morphology prevails throughout the cross-sectional area of the *h*=2.5 nm Mg/Ti multilayer annealed at 200 °C for 2 h. Figure 4.4(a) is the typical TEM micrograph illustrating the microstructure of annealed *h*=2.5 nm Mg/Ti multilayer specimen, in which the column boundaries can be easily recognized. Within each column, Mg and Ti layers maintain the epitaxial growth pattern, mainly following the OR.1' relationship, as indicated by the selected-area DP in Figure 4.4(b). Most of these columns extend through the whole thickness of the film.

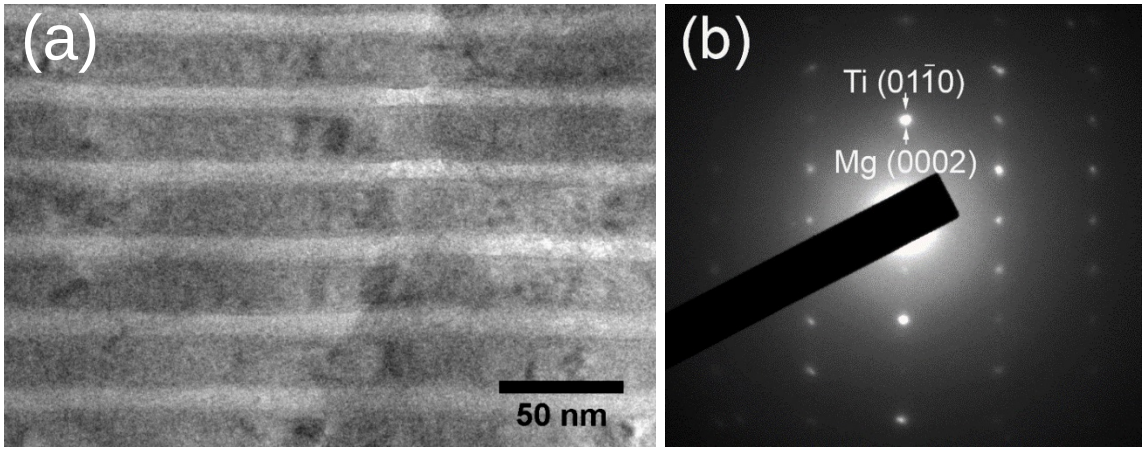

Figure 4.3: (a) The bright-field TEM micrograph illustrating the cross-sectional microstructure of the *h*=20 nm Mg/Ti multilayered nanofilm annealed at 200 °C for 2 h, with the corresponding DP in (b).

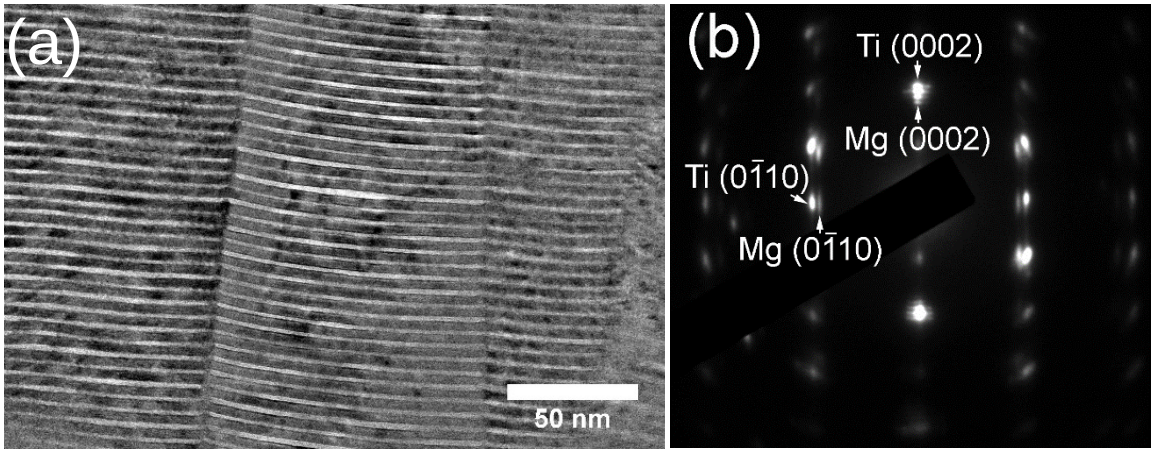

Figure 4.4: (a) The bright-field TEM micrograph illustrating the cross-sectional microstructure of the *h*=2.5 nm Mg/Ti multilayered nanofilm annealed at 200 °C for 2 h. (b) A typical selected-area diffraction pattern within each column illustrating the OR.1' relationship between Mg and Ti layers.

Columnar growth is very common in vapor-deposited films and is intimately related to the sputtering pressure and substrate temperature. It has been reported in Ag/Cu [227], Ni/Ru [228], Cu/Nb [229], Cu/V [72] and many other multilayered nanofilms. Compared with these polycrystalline multilayers where column boundaries usually coincide with in-plane grain boundaries, the column growth in Mg/Ti multilayers is less significant. As we can see in Figure 4.4, the mis-orientation between adjacent columns is pretty small. Hence, the annealed *h*=2.5 nm Mg/Ti multilayer remain highly textured, in consistency with the distinguished Mg (0002) and Ti (0002) reflections in Figure 4.1.

Unlike the continuous individual layers across the whole cross-sectional area of the as-deposited Mg/Ti film with *h*=2.5 nm, interrupted layers were observed at column boundaries in its annealed counterparts. Figure 4.5(a) is the HRTEM image illustrating such a lamellae destruction in the *h*=2.5 nm Mg/Ti multilayer after annealing. Previous studies on the immiscible multilayers subjected to high temperatures indicate that the unstable lamellar structure is usually accompanied with layer termination or grain

spheroidization [230]. However, none of them has been detected in our annealed Mg/Ti multilayers. Rather a great deal of lattice distortion can be clearly seen in the vicinity of layer pinch-off in Figure 4.5(a). To better understand the microstructural changes with annealing, we selected a representative area containing rearranged atoms (the yellow square in Figure 4.5(a)) and amplified it in Figure 4.5(b). The atomic configuration in Figure 4.5(b) is obviously different from that in regular layers (Mg and Ti lattice oriented with basal plane parallel to the interface, refer to Figure 3.5). The planar spacing d_1 and d_2 in Figure 4.5(b) are measured as ~0.25 and 0.30 nm, respectively. Figure 4.5(c) is the Fast Fourier Transformation (FFT) image corresponding to Figure 4.5(b), which is also distinct from that in Figure 4.4(b), indicating the formation of a metastable phase.

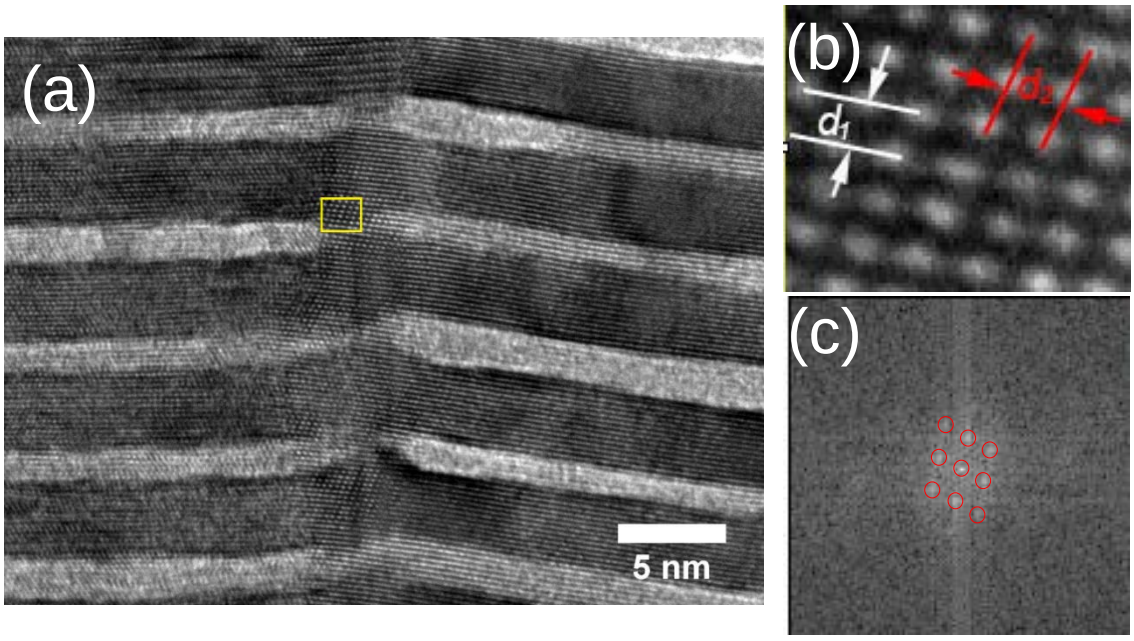

Figure 4.5: (a) A HRTEM image illustrating the breakdown of individual layers at column boundaries in the annealed Mg/Ti multilayered nanofilm with h=2.5 nm. (b) the enlarged HRTEM image to show the atomic arrangement, with the correspoding FFT image in (c).

Although the intermixing between constituents is not expected in such an immiscible multilayer system, it is difficult to discriminate Ti and Mg atoms located at the column boundaries since they have almost identical FFT images. Noteworthy, however, is that d_2 shrinks to ~0.28 nm when we examined the regions right above the yellow square in Figure 4.5(a). A discussion concerning the appearance of this particular atomic arrangement and its influence on the mechanical behavior of Mg/Ti multilayered nanofilms will be presented in what follows.

4.2 Mechanical Properties

Nanoindentation experiments were performed on the annealed Mg/Ti multilayers with various individual layer thicknesses to characterize their mechanical properties. We tuned the annealing time and annealing temperature to track the evolution of hardness, and in turn to investigate the capability of Mg/Ti multilayers in maintaining the high strength at elevated temperatures.

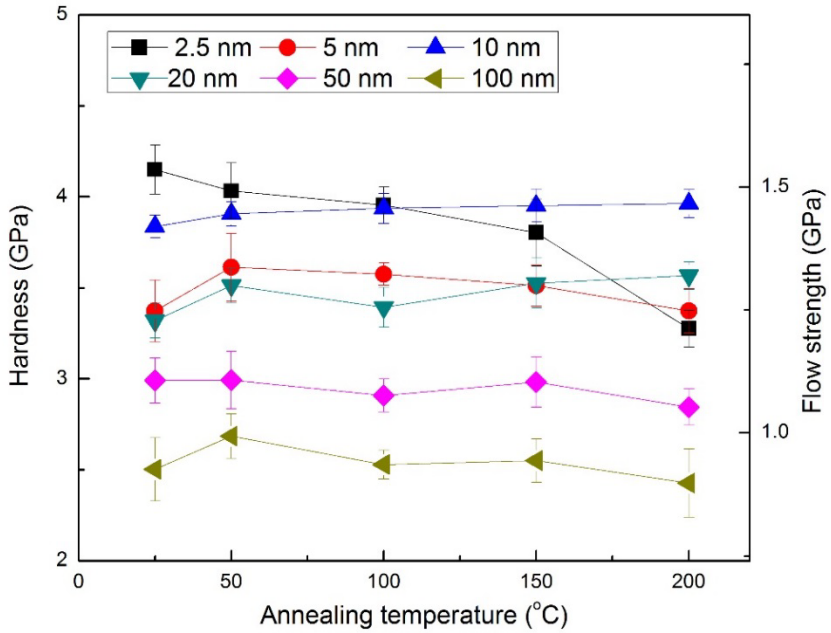

Figure 4.6: The hardness of Mg/Ti metallic multilayers annealed at various temperatures.

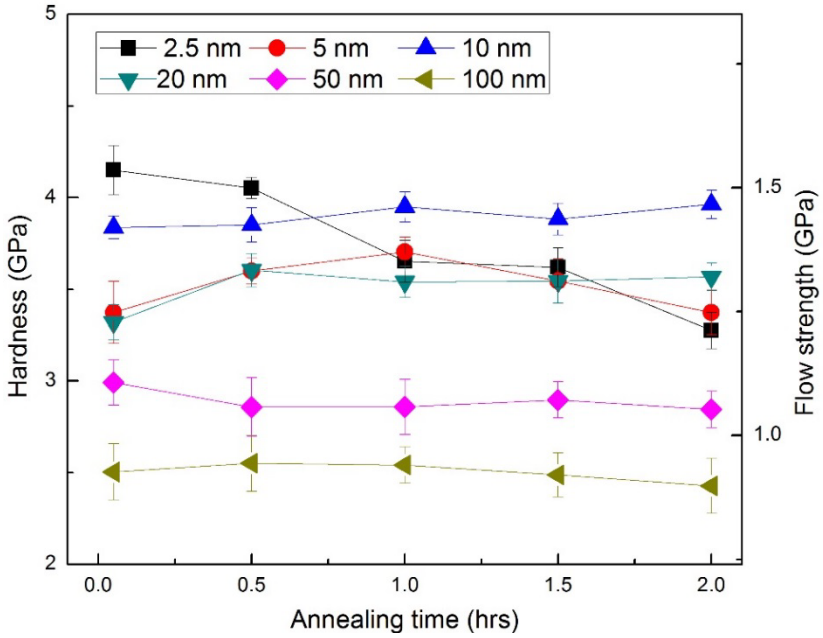

Figure 4.7: The hardness of Mg/Ti metallic multilayers annealed at 200 °C for various time periods.

The effect of annealing temperature on the hardness of Mg/Ti metallic multilayers is shown in Figure 4.6. The most left point on each curve represents the hardness of the as-deposited Mg/Ti films. Given the annealing time up to 2 hours, no significant change of hardness is noted in the Mg/Ti multilayers with $h \geq 5$ nm. However, the hardness of h=2.5 nm Mg/Ti multilayers exhibits a descending trend as the annealing temperature increases, eventually reaching the minimum ~3.30 GPa at 200 °C. According to the Tabor's law, the flow strength corresponding to the minimum hardness is roughly 1.22 GPa, which is still very impressive in the community of metallic multilayers.

Figure 4.7 illustrates the hardness of Mg/Ti multilayers after annealing at 200 °C for 0.5 to 2 h. Similar to the annealing temperature, the annealing time has limited impact on the strength of Mg/Ti multilayers when $h \geq 5$ nm. For the smallest h (2.5 nm) investigated

in our study, the increase of annealing time brings about an obvious reduction of hardness. Based on these experimental observations, a time-related process, such as diffusion, is suggested to account for the loss of strength in Mg/Ti multilayered nanofilms.

4.3 Discussions

The difference between the as-deposited and the annealed Mg/Ti multilayers in microstructure and mechanical properties indicates the significance of heat treatments, especially when the individual layer thickness decreases to several nanometers. In this section, we will explicitly discuss the thermal stabilities of Mg/Ti multilayer system in order to provide good predications on the performance of other HCP-based multilayer thin films upon annealing at elevated temperatures.

4.3.1 Morphological Stability

According to the phase diagram as shown in Figure 1.11, Mg and Ti have vanishingly small solubility to each other up to 1600 °C. No intermetallic compound or intermixing shall be expected in our annealed Mg/Ti multilayer thin films. Therefore, the inter-diffusion based mechanisms, which lead to the failure of Mo/V [225], Cu/Ni [222] and TiN/CrN [231] multilayers at elevated temperatures, might not be the primary reason for the deterioration of lamellar structure observed in the annealed Mg/Ti multilayer with h=2.5 nm (Figure 4.5(a)).

Compared with the homogenization occurring in miscible multilayers after annealing, the thermal grooving induced by grain boundary splitting is much more recognized as the instability mechanism of immiscible polycrystalline multilayers. Figure 4.8 schematically illustrates a typical grain-boundary grooving-driven instability in polycrystalline multilayers, where the in-plane grain boundaries of constituent A and B are

vertically matching [229]. The diffusive mass transport associated with increasing temperature would induce the recession of layers away from the grain boundaries (Figure 4.8(b)), and finally layer pinch-off (Figure 4.8(c)). The groove angle 2θ is largely determined by the ratio of grain boundary energy γ_{gb} to interface energy γ_{int}, following

$$\cos\theta = \gamma_{gb} / 2\gamma_{int} \tag{26}$$

A small groove angle normally denotes a deep groove developed in the layers. Consequently, the layers with higher grain boundary energy (γ_{gb}) will be less stable and prone to degrade in annealing.

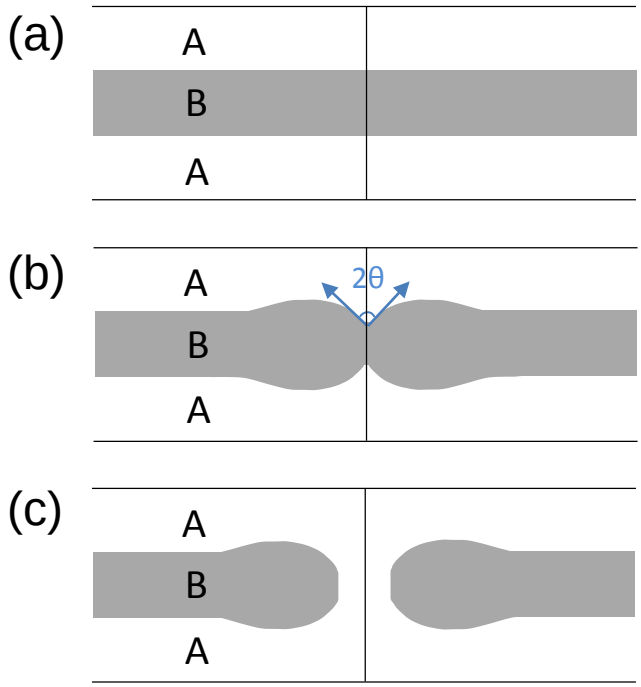

Figure 4.8: Schematic diagrams of a typical grain-boundary grooving-driven instability in polycrystalline multilayers.

Non-coincident grain boundaries are also very common in metallic multilayers. The triple-point junctions located at the intersection of a grain boundary and phase interface act

as the initial sites for thermal grooving. In this case, the grain boundaries are laterally offset and pinch-off takes place in both layers, followed by the spheroidization and discontinuous coarsening to decrease the overall interfacial energy of the multilayer.

There are several other instability mechanisms in lamellar microstructure, such as direct cylinderization, edge spheroidization and termination migration, which are mainly derived from the studies of thermal stability of eutectic or eutectoid composites, i.e. Ti/Al alloys [232]. Our microstructural investigation of annealed Mg/Ti multilayers reveals the absence of granular morphology, suggesting the deterioration of lamellar structure at h=2.5 nm is more likely to result from the boundary thermal grooving. However, consider the fact that Mg and Ti are highly textured and their grain boundaries could hardly be discerned except along column boundaries (Figure 3.3(a) and 4-4(a)), it may not be plausible to treat Mg/Ti multilayers as traditional “polycrystalline multilayers”. Here we propose a modified thermal grooving model to interpret the morphological instability of Mg/Ti multilayers. Since the thermally induced changes of lamellar microstructure were only detected in the film with h=2.5, the following discussions are primarily based on the microstructural evolution of Mg/Ti multilayers at this length scale.

Figure 4.9(a) schematically illustrates the microstructure of an as-deposited Mg/Ti multilayered nanofilm. It is well known that the morphology of thin films is considerably sensitive to the deposition conditions, e.g. deposition pressure and substrate temperature. Therefore, in spite of the prevailing continuity of Mg and Ti layers throughout the film, the appearance of tiny morphological perturbations in Mg/Ti multilayers is practically inevitable, which is possibly a result of the competition between instabilities arising from discrete atomic deposition and stabilizing influence of surface diffusion [233].

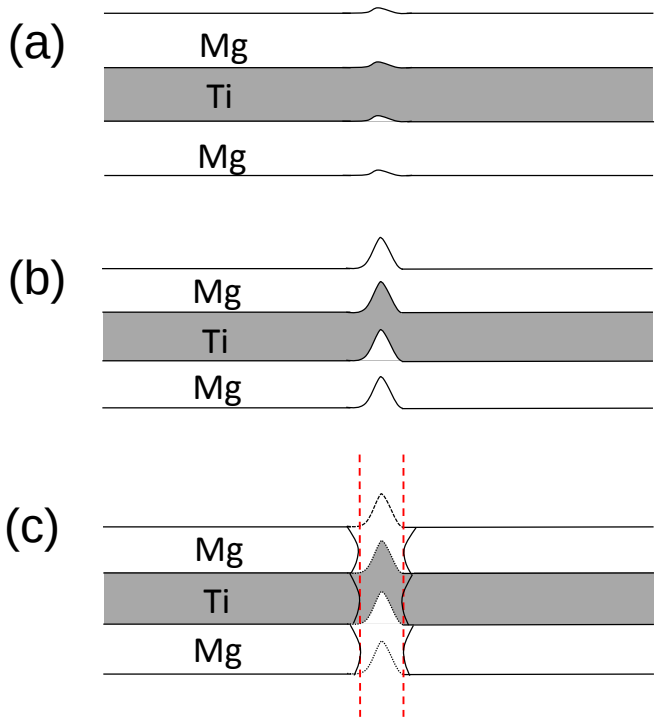

Figure 4.9: Schematic diagrams of the morphological instability in Mg/Ti multilayers.

Due to the curved interface geometry where chemical potential gradient lies in, the diffusive mass transportation accompanied with increasing temperature will intensify the grooving as shown in Figure 4.9(b). Relieving the stress caused by thermal strain might be another driving force for the deep grooves in annealed Mg/Ti multilayers. The schematic diagrams in Figure 4.9(a) and (b) explain the presence of thermal grooves in the highly textured multilayered nanofilms where grain boundaries are rarely seen.

Instead of the conspicuous layer recession described in Figure 4.8(c), the atomic diffusion gives rise to a transition zone (enclosed by the red dot lines in Figure 4.9(c)) on the microstructure in which the atomic arrangement of Mg and Ti is different from the HCP structure. Interestingly, as shown in Figure 4.9(c), the displaced Mg atoms in the transition

zone is located above the regular Mg layers, agreeing well with our morphological inspections on the annealed *h*=2.5 Mg/Ti film (Figure 4.5(b)). It is proposed that the morphological changes of Mg/Ti multilayered nanofilms during annealing is essentially accomplished by the thermally-activated diffusion.

As a matter of fact, both Mg and Ti have a strong propensity of phase transformation, particularly at high temperature, high pressure or other favorable experimental conditions. For example, pure Ti experiences a natural transition from α phase (HCP structure) to β phase (BCC structure) at approximately 1115 K. Alloying with beta stabilizers, i.e. Mo, Ta, Fe and Co, is able to lower the transition temperature. Increasing strains was reported to promote the α-to-β phase transition in a Ti alloy even at ambient temperature [234]. Nevertheless, the phase transition of Mg is more dependent on the pressure than on the temperature. The calculation results based on first-principles theory from Jona and Marcus revealed a martensitic transition of Mg from HCP structure to BCC structure at hydrostatic pressure lager than 500kbar [235]. Moreover, the metastable BCC Mg were experimentally observed in the magnetron sputtered Mg/Nb multilayers with individual layer thickness of 5 nm, while subsequent density functional theory calculations demonstrated that the stabilization of BCC Mg deposited on BCC Nb substrate is analogous to the stabilization of BCC Mg under high pressures because of the mechanical constraints imposed on Mg [80, 236]. If we take the mechanical synthesized Mg_xTi_{100-x} alloys into account, the analysis of involving crystal structures becomes very complicated, as reflected by the variation of phase structures and lattice parameters with the atomic weight variable *x* changing from 35 to 80 [196].

Our examinations of the atomic arrangement at column boundaries of the annealed Mg/Ti specimen with h=2.5 nm (Figure 4.5(a)-(c)) indicate that, although Mg lattice in the transition zone is no more with HCP structure, it is not a perfect BCC or FCC lattice. For example, the FFT image in Figure 4.5(c) is similar to the diffraction pattern of BCC crystals with [111] zone axis but still have small discrepancies from it, which essentially result from the difference between d_1 and d_2 in Figure 4.5(b). In this sense, it is a metastable Mg phase that possesses a transition lattice structure from HCP to BCC in the transition zone. This speculation is also applicable for Ti. However, since the transition zone takes a small volume of the annealed Mg/Ti nanofilm, the reflections of these metastable phases are too weak to be identified on the XRD patterns.

Additionally, we note the degradation of lamellar structure was only detected in annealed Mg/Ti multilayers with h=2.5 nm, rather than other Mg/Ti specimens. The dependence of morphological stability on the individual layer thickness h is thus inferred for the Mg/Ti multilayer system. Actually, the influence of grain aspect ratio d/h on the stability of lamellar structure has been recognized in a variety of multilayer systems [229, 237, 238]. Given a small h, the layer splitting is easier to occur because the diffusion distance is shortened. A critical d/h ratio associated with the grain-boundary energy of layer constituents was even proposed by Josell et al., below which the layer pinch-off is restricted [237]. Due to the ambiguous grain boundaries in Mg/Ti multilayers with large h, it is extremely difficult to determine the average value of d. Thereby, we do not attempt to quantitatively derive the critical d/h ratio for Mg/Ti multilayer system in this study. The zig-zag shape triple-point junctions, which are argued to improve the morphological stability of Cu/Nb multilayer films with h>35 nm at elevated temperatures, have not been

observed in our annealed Mg/Ti multilayers, owing to the preferential growth of Mg and Ti during deposition process.

4.3.2 Mechanical Stability

To a large extent, the mechanical stability of materials is controlled by their morphological stability. Take polycrystalline multilayers for example, grain growth and layer coarsening are two major factors affecting the mechanical properties at elevated temperatures. Since the individual layer thickness h is usually smaller than the average grain size d in as-deposited metallic multilayers, the contribution of d to the strength has always been assumed to be negligible in the literature. In the analysis of the hardness and flow strength of as-deposited Mg/Ti multilayers, we have illustrated an impressive consistency of the experimental results to the theoretical predictions of h-dependent strengthening mechanisms. It is reasonable to omit the effects of d on the strength in that case since there are few grain boundaries in the highly textured Mg/Ti multilayers.

The experimental results obtained from nanoindentation (Figure 4.6 and 4.7) demonstrate that, when $h \geq 5$ nm, there is insignificant change of hardness in Mg/Ti multilayers after annealing at 200 °C for 2 h. At this intrinsic size sale, Mg/Ti multilayer thin films indeed exhibit a high level of mechanical stability, in agreement with the sharp interface and stable lamellar microstructure as displayed in Figure 4.4(a). Nevertheless, a drop of hardness occurred in the annealed Mg/Ti multilayer specimens with the smallest h in this study (h=2.5 nm). In order to understand this mechanical behavior, we invoke a similar hardness reduction of Cu/Nb nanofilms reported by Misra et al. [230]. The authors correlated the decrease of hardness (~0.3 GPa) in h=75 nm Cu/Nb multilayers during a short term anneal at 700 °C to the apparent in-plane grain growth from ~75 nm to ~200 nm.

As for the h=15 nm Cu/Nb multilayers, a dramatic drop of hardness by a factor of two was noticed when the annealing temperature approached 600 °C, at which spheroidization of the lamellar microstructure began. The detrimental impacts of layer spheroidization to the mechanical integrity were also identified in Ni/Ru (at 600 °C) [228] and Cu/Ag multilayers (at 149 °C) [75]. Because of the moderate annealing temperature and time adopted, we did not detect any layer spheroidization in our annealed Mg/Ti multilayers. Together with the single-crystal-like microstructure features of as-deposited Mg/Ti multilayers, grain growth and layer spheroidization should not be the primary reasons for the decreased hardness of annealed h=2.5 nm Mg/Ti thin films. The thermally-induced transition zone observed in these annealed Mg/Ti nanofilms may contribute the most to the impaired mechanical integrity. It is suggested that, the appearance of transition zones, which intends to relieve the internal stress arising from the thermal strain and misfit strain, disrupted the well-order lamellar microstructure and weakened the impeding effect of layer interfaces toward the Orowan-type dislocation sliding as well as the subsequent dislocation transmission.

4.4 Conclusions

In this chapter, we have investigated the thermal stability of Mg/Ti multilayer films with varying individual layer thickness h by examining their microstructure and mechanical properties after a series of anneals. Overall the Mg/Ti multilayers exhibit excellent capabilities in maintaining the lamellar structure and high strength at elevated temperatures. In details, the following conclusions are reached.

There is no significant change in the crystallography and microstructure of Mg/Ti multilayers with $h \geq 5$ nm after annealing up to at 200 °C for 2 h. Both Mg and Ti layers are still highly textured along c-axis. The XRD results also reveal the absence of any

intermetallic or oxide in our annealed Mg/Ti specimens. The impressive morphological stability of Mg/Ti multilayers at relatively large h is also confirmed by the TEM examinations, which display the intact layers and sharp interface of annealed multilayers. However, for the Mg/Ti multilayers with h=2.5 nm, annealing at 200 °C for 2 hours enhances the columnar boundaries and consequently disrupts the regular lamellar morphology. A transition zone with rearranged Mg and Ti atoms has been observed at some columnar boundaries.

Nanoindentation measurements indicate that the hardness of Mg/Ti multilayers exhibit almost no change after annealing when $h \geq 5$ nm. A remarkable drop in hardness is revealed at h=2.5 nm, from ~4.2 GPa of the as-deposited Mg/Ti multilayers to ~3.3 GPa of the annealed ones. Such a strength loss is closely related to the obvious morphological changes at this intrinsic size level. Based on the microstructural and mechanical evolution of Mg/Ti multilayers over a variety of annealing temperature and annealing time, the dependence of thermal stability on the length scale of h is concluded.

CHAPTER 5: MAGNESIUM/ZIRCONIUM MULTILAYERED NANOFILMS

For multilayered nanofilms, the layer interfaces have been regarded as strong barriers to impede dislocation motions, contributing to the impressive high strength. However, there remains some important issues and concerns about the interaction between layer interfaces and gliding dislocations that have not been well understood. For example, one may ask: which type of interfaces will be more effective in enhancing the strength, and whether these interfaces could be manipulated via the choice of constituents or layer thickness.

Refer to the classification of interfaces depicted in Chapter 1, binary multilayer systems can be categorized into coherent, semi-coherent and incoherent ones based on the extent of lattice matching between layer constituents. Despite the almost universal high strength as experimentally measured in multilayered nanofilms, the atomistic simulations by Hoagland et al. suggest that the strengthening mechanisms might vary with the interface type, coherent or incoherent [112]. They found that the coherency strain imposed the dominant resistance to slip transmission across coherent interfaces, while the high resistance in incoherent systems originated from the low shear strength of interfaces and subsequent dislocation core spreading on them.

In Chapter 3, we analytically derived the peak strength of Mg/Ti multilayers by considering the intrinsic properties of interfaces, such as the modulus mismatch and lattice

mismatch between Mg and Ti. According to Equations (24) and (25), τ_{misfit}, the resistance arising from the arrays of misfit dislocations on the semi-coherent Mg/Ti interfaces, takes up as high as ~42% of the total stress required for the glide of dislocations across the interfaces. To further investigate the effect of lattice mismatch on the mechanical properties of HCP-based metallic multilayers, we additionally prepared Mg/Zr multilayered nanofilms, following the same methodology applied on Mg/Ti specimens. Table 8 lists the lattice parameters and elastic properties of pure Mg, Ti and Zr, based on which the lattice mismatch and elastic mismatch of Mg/Zr and Mg/Ti multilayers are calculated, as shown in Table 9. Similar to Mg/Ti, Mg/Zr system has a positive heat of mixing, and thus is immiscible. Nevertheless, the lattice mismatch at interfaces of Mg/Zr multilayers is much less than that of Mg/Ti multilayers. Mg/Zr multilayers are nominally characterized with coherent interfaces.

Table 8: The lattice parameters and elastic properties of three typical HCP metals.

Metal	Lattice parameter *a*, Å	Lattice parameter *c*, Å	Young's modulus *E*, GPa	Shear modulus μ, GPa
Mg	3.203	5.201	44	16
Ti	2.950	4.683	116	44
Zr	3.231	5.147	95	35

Table 9: Comparisons between Mg/Zr and Mg/Ti multilayers in lattice mismatch and modulus mismatch.

Multilayer system	Mutual solubility	Lattice mismatch	Elastic mismatch
Mg/Zr	Immiscible	0.87%	0.346
Mg/Ti	Immiscible	8.22%	0.443

Note:* The elastic mismatch is calculated via $(\mu_X - \mu_{Mg})/(\mu_X + \mu_{Mg})$, where X denotes Zr or Ti.

In following, we will present some preliminary experimental results about the microstructure and mechanical properties of as-deposited Mg/Zr thin films with varying individual layer thicknesses, and then discuss the dependence of strength on the interface type of multilayers composed with HCP metals.

5.1 Crystallography and Microstructure

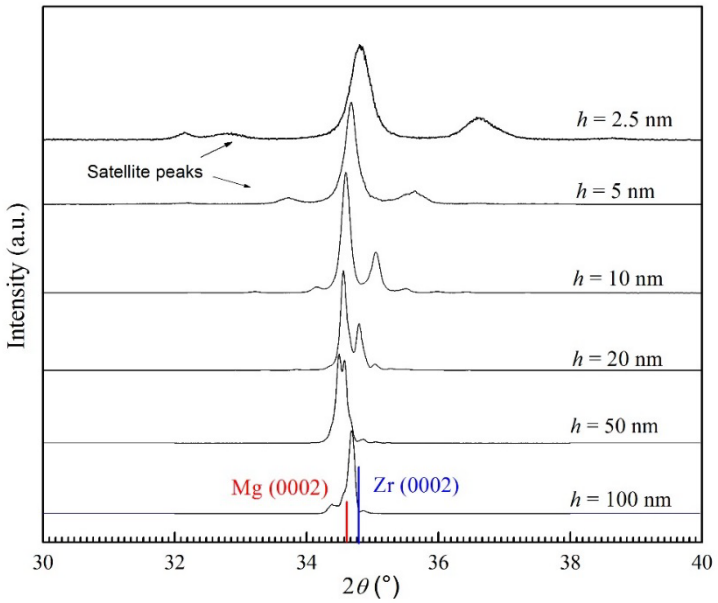

Figure 5.1: X-ray diffraction results of as-deposited Mg/Zr multilayered nanofilms with various individual layer thicknesses *h* from 2.5 nm to 100 nm.

Figure 5.1 displays the XRD spectra of Mg/Zr multilayered nanofilms at various individual layer thicknesses (h from 2.5 to100 nm). As we can see, regardless of h, Mg and Zr exhibit preferential growth along c-axis ([0002] direction), with the basal plane parallel to the phase interface. Since the lattice parameters of Zr are very close to those of Mg, as listed in Table 8, the characteristic peaks of Mg and Zr are overlapping to a large extent. It is extremely difficult to discriminate Mg (0002) reflection from Zr (0002) reflection on the XRD patterns. When h decreases to 20 nm or below, satellite peaks become noticeable in

Figure 5.1. Again, we measured their positions and calculated the bilayer thickness Λ of as-deposited Mg/Zr multilayers according to Equation (9), with the results summarized in Table 10.

Table 10: The values of bilayer period Λ measured by XRR and XRD for Mg/Zr multilayered nanofilms.

Designed bilayer period Λ $\Lambda = h_{Zr} + h_{Mg}$ /nm	Λ measured from XRR /nm		Λ measured from XRD/nm	
	Average	Error	Average	Error
5 (2.5+2.5)	--	--	4.80	0.05
10 (5+5)	--	--	9.58	0.02
20 (10+10)	21.94	1.64	19.90	0.15
40 (20+20)	37.54	2.20	40.62	0.32
100 (50+50)	93.58	8.44	--	--
200 (100+100)	193.10	--	--	--

Obviously, the bilayer period measured by XRD approaches to the designed value, indicating the accurate modulation of Mg/Zr multilayered nanofilms achieved in the deposition process. The XRR results of Λ are also included in Table 10, agreeing well with the XRD measurements. For *h*=2.5 nm and 5 nm Mg/Zr specimens, the absence of XRR result is attributed to the undistinguishable periodic peaks at nanoscale *h*.

In contrast to the appearance of Ti $(10\bar{1}0)$ reflections in the as-deposited Mg/Ti multilayers with relatively large *h* (Figure 3.1), only Mg (0002) and Zr (0002) reflections have been detected in Figure 5.1. The predominance of HCP-on-HCP epitaxial growth mode is thus inferred for Mg/Zr multilayers, which is largely independent on *h*. Noteworthy, however, is that it might be the first time to experimentally observe such a growth pattern in the community of metallic multilayers. Compared with the FCC/FCC multilayers where cubic-to-cubic relationship is most energetically favorable, HCP/HCP multilayers might alter the growth path of components in the cases of large lattice mismatch at interfaces.

5.2 Mechanical Properties

Figure 5.2 shows the nanoindentation hardness H and flow strength σ of Mg/Zr multilayer specimens as a function of $h^{-0.5}$. The hardness values of Mg/Ti multilayers have also been plotted in the figure for comparison. It is clearly seen that, for Mg/Zr multilayers at $h \geq 10$ nm, the hardness generally increases with decreasing layer periodicity even though the increment rate becomes smaller and smaller. A gradual decline of hardness is observed when h decreases from 10 nm to 2.5 nm. Unlike Mg/Ti multilayers, in which the maximum hardness was obtained at the smallest layer thickness of 2.5 nm, the peak hardness of Mg/Zr multilayers ~3.78 GPa appears in the specimen with h=10 nm. Compared with semi-coherent Mg/Ti interfaces, the fact that fewer misfit dislocations situating on the coherent Mg/Zr interfaces may account for the obvious softening at nanoscale h in Figure 5.2. A numerical analysis with regard to the difference in mechanical behavior between Mg/Ti and Mg/Zr multilayered nanofilms will be presented in next section.

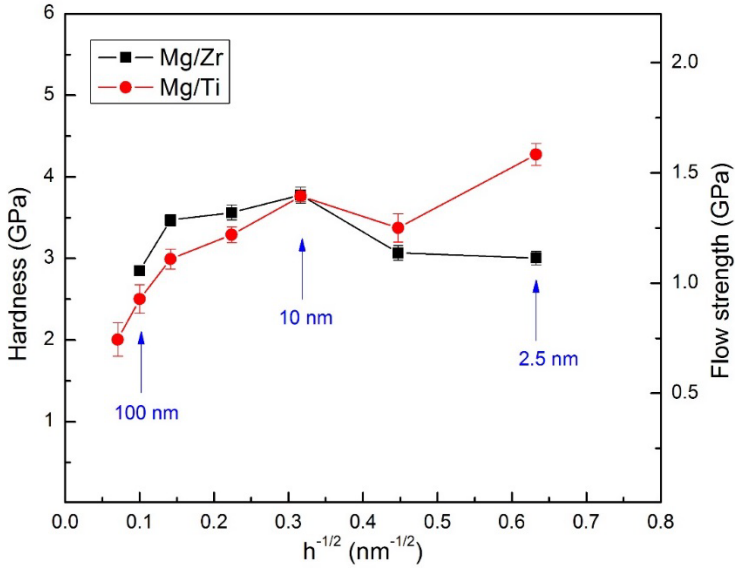

Figure 5.2: The plot of nanoindentation hardness H and flow strength σ as a function of $h^{-0.5}$ for Mg/Zr multilayer specimens. The experimental data of Mg/Ti multilayered naofilms has also been plotted for comparison.

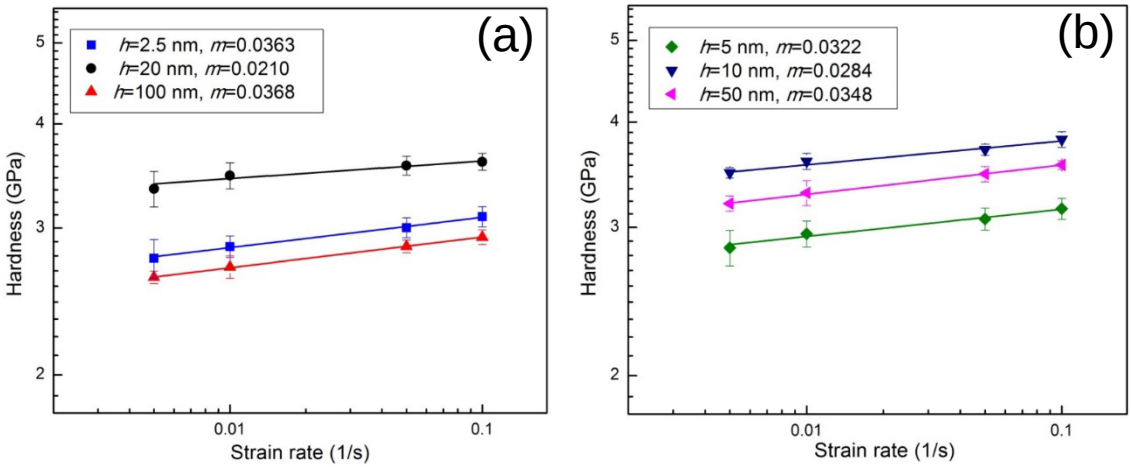

Figure 5.3: Experimental results of strain rate sensitivity (SRS) of the Mg/Zr multilayered specimens with various individual layer thicknesses (a) h=2.5, 20 and 100 nm; (b) h=5, 10 and 50 nm.

The hardness results in Figure 5.2 were collected under a constant strain rate $\dot{\varepsilon}$ of 0.05 s^{-1}. To further explore the plastic deformation of Mg/Zr metallic multilayers, we derived the strain rate sensitivity m by measuring the hardness at other strain rates, such as 0.005, 0.01 and 0.1 s^{-1}. The $\ln H$ *vs.* $\ln\dot{\varepsilon}$ plots of various Mg/Zr multilayer films are shown in Figure 5.3. For each specimen, the data points invariably fall onto a straight line (sketched out in Figure 5.3(a) and (b)), whose slope represents m. As summarized in Table 11, the SRS of the investigated Mg/Ti films ranges from 0.021 to 0.037 while the corresponding activation volume V^* (calculated by following Equation (21)) is in the range of 5.0—8.0 b^3. We can see that, the m and V^* values of Mg/Zr multilayers are almost identical to those of Mg/Ti multilayers (Table 5). Due to the relatively small activation volumes, boundary-related mechanisms are suggested to be responsible for the change of hardness with strain rate in HCP/HCP multilayered nanofilms. Unfortunately, a straightforward relationship between SRS and individual layer thickness could hardly be reached for Mg/Zr multilayers either.

Table 11: Strain rate sensitivity m and activation volume V^* of Mg/Zr multilayered nanofilms with various individual layer thicknesses.

h (nm)	2.5	5	10	20	50	100
m	0.0363	0.0322	0.0284	0.0210	0.0348	0.0368
V^*	5.526 b^3	6.073b^3	5.666 b^3	8.004 b^3	4.991 b^3	5.755 b^3

5.3 Discussions

In this study, Mg/Zr multilayers with various individual layer thicknesses were intentionally prepared and compared with Mg/Ti multilayers in microstructure and mechanical properties to reveal the influence of interface characteristics on the plastic deformation in HCP-based multilayered nanofilms. From the experimental results in Figure 5.2, when $h \geq 10$ nm, Mg/Zr multilayers are analogous to Mg/Ti multilayers, of which the flow strength exhibits an inversely proportional relation to the individual layer thickness. Nevertheless, the strength of Mg/Zr multilayers declines with decreasing h in the range of $2.5 \leq h \leq 10$ nm, deviating from that of Mg/Ti ones. The peak strength achieved in our Mg/Zr films is ~1.40 GPa. Prior to a numerical study of the resistance to glide, we need to understand the fundamental differences between coherent Mg/Zr and semi-coherent Mg/Ti interfaces.

As listed in Table 9, the lattice mismatch at Mg/Zr interfaces is remarkably small. By following Equation (22),

$$h_{\mathrm{cr}} = \frac{b}{2\pi\varepsilon_{\mathrm{m}}} \ln\left(\frac{\sqrt{2}h_{\mathrm{cr}}}{b}\right) \tag{22}$$

the critical thickness with respect to the formation of misfit dislocations is estimated to be ~28.25 nm. In other words, the layer interfaces in h=2.5, 5, 10 and 20 nm Mg/Zr specimens

should be fully coherent, without misfit dislocations deposited on them. In contrast, the value of h_{cr} for Mg/Ti system derived in Chapter 3 is only 0.6 nm, indicating a large number of misfit dislocations involved.

According to the model proposed by Hoagland et al. [112], the coherency stress σ_{coh} plays an important, or even dominant, role in blocking the slip transmission across coherent interfaces, which can be calculated via Equation (7)

$$\sigma_{coh} = \left(\frac{C_{Mg} C_{Zr}}{C_{Mg} + C_{Zr}} \right) \left(2 \frac{a_{Mg} - a_{Zr}}{a_{Mg} + a_{Zr}} \right) \tag{7}$$

where the symbol *C* represents the biaxial elastic constant of layer constituents. Given the assumption of isotropic structures, we replace them with the elastic moduli and then obtain the coherent stress of Mg/Zr interfaces as ~0.26 GPa.

In addition to coherency stress, the image stress arising from the different moduli between Mg and Zr would also make the multilayered nanofilms stronger. Similarly, the upper bound of image stress for Mg/Zr system can be determined by using Equation (6).

$$\tau_{image} = \frac{\mu_{Zr} - \mu_{Mg}}{\mu_{Zr} + \mu_{Mg}} \cdot \frac{\mu_{Mg} \sin\theta}{8\pi} \tag{6}$$

Substituting the detailed values into the above equation, τ_{image} is approximately equal to 0.20 GPa. With the Taylor factor multiplied to τ_{image}, the applied stress σ_{image} required to overcome the intrinsic modulus mismatch is 0.62 GPa.

However, the sum of σ_{coh} and σ_{image}, which is ~ 0.88 GPa, cannot match the peak strength of Mg/Zr multilayers measured from nanoindentation. We believe that, one possible reason for this is the theoretical underestimate of σ_{coh}. The Equation (7) was

derived by Hoagland and coworkers on the basis of FCC/FCC metallic multilayers with "transparent interfaces", across which the slip planes and slip directions are still continuous. Indeed, they found the maximum attainable flow strength of Cu/Ni multilayers was in a reasonable agreement with the simulation results. Our Mg/Zr system is characterized with coherent interfaces, but not exactly "transparent interfaces" as described, since the slip systems might not be continuous for glide dislocations when entering into the adjacent layers. For example, basal slips are the primary slip systems for Mg while Zr is prone to deform with non-basal slips at room temperature. Due to the epitaxial growth along *c*-axis, pyramidal slip systems are likely to be activated during deformation processes. But whether the pyramidal slip systems are continuous across interfaces is very doubtful. Other factors, such as the step creation, core spreading and cutting of misfit dislocations on crossing interfaces, could also enhance the flow strength [112]. Hence, more experimental efforts are needed to elucidate the strengthening mechanisms in the HCP-based multilayers with coherent interfaces.

The softening of metallic multilayers with the individual layer thickness decreased to a few nanometers has been observed in many FCC/FCC systems, e.g. Cu/Ni [91], Cu/304SS [77]. There are two major factors suggested to account for this phenomenon which might also work with the diminishing hardness of Mg/Zr films with $h<10$ nm. First, the strengthening effects from interfaces could be impaired as the layer thickness approaches the dislocation core size. Second, the image stress might decrease with the length scale of h [71, 112]. To affirm either of them in the context of HCP-based multilayers, the supports from atomistic simulation are essentially required.

5.4 Conclusions

Based on the preliminary experimental results about the microstructure and mechanical behavior of as-deposited Mg/Zr multilayered nanofilms as presented in this chapter, the following conclusions can be drawn.

Both Mg and Zr layers are highly textured along *c*-axis and exhibit strong preference of epitaxial growth, which are largely independent on the individual layer thickness. At $h \geq 10$ nm, the hardness/flow strength of Mg/Zr multilayers generally increases with decreasing layer periodicity. However, a gradual decline of hardness has been observed when *h* decreases from 10 nm to 2.5 nm. The distinct mechanical response of Mg/Zr multilayers from Mg/Ti ones at relatively small *h* might arise from the specific interaction between glide dislocations and intrinsic coherent interfaces of multilayered nanofilms composed of HCP metals.

CHAPTER 6: CONCLUSIONS AND FUTURE WORKS

6.1 Conclusions

As a typical HCP-based multilayer system, the Mg/Ti multilayered nanofilms investigated in this work exhibit distinctive characteristics in microstructure and mechanical behavior.

Based on the XRD results, the constituent layers of as-deposited Mg/Ti films are highly textured along Mg (0002) and Ti (0002). Such a tendency of epitaxial growth becomes stronger and stronger in Mg/Ti multilayers as the individual layer thickness *h* decreases from 200 nm to 2.5 nm. Accordingly, when *h*=2.5 nm, there is a single orientation relationship between Mg and Ti, Mg $\{0002\}$// Ti $\{0002\}$ and Mg $<01\bar{1}0>$// Ti $<01\bar{1}0>$ (or Mg $<2\bar{1}\bar{1}0>$ // Ti $<2\bar{1}\bar{1}0>$ with in-plane rotation of crystals), identified in TEM examinations. High resolution TEM further confirms this inter-epitaxial relationship between Mg and Ti layers at relatively small *h*. However, when the individual layer thickness is increased, another orientation relationship between Mg and Ti starts to emerge, which is Mg $\{0002\}$// Ti $\{01\bar{1}0\}$ and Mg $<2\bar{1}\bar{1}0>$// Ti $<0001>$.

Nanoindentation measurements on the as-deposited Mg/Ti multilayered nanofilms reveal the dependence of hardness/strength on the length scale of *h*. When $h \geq 50$ nm, the hardness increases with decreasing *h*, following the classical Hall-Petch relation. At relatively small individual layer thickness, the Hall-Petch slope levels off. The confined layer slip (CLS) model provides a better predication of flow strength in the Mg/Ti films

with $2.5 \leq h \leq 20$ nm. The maximum hardness of ~4.2 GPa is reached at the smallest individual layer thickness (h=2.5 nm).

Microcompression agrees well with nanoindentation in measuring the flow strength of Mg/Ti multilayer specimens when h is about a few tens of nanometers or larger. However, when h decreases to several nanometers, the microcompression measured flow strength is much higher than that derived from nanoindentation. This discrepancy can be explained by the nearly vanishing Schmid factor of all the fundamental slip systems of both Mg and Ti layers under uniaxial compressive loading. According to the post-loading morphology of Mg/Ti micropillars, plastic deformation proceeds from the top of the pillars while no shear band forms during compression. Moreover, the Mg/Ti micropillars exhibit a general trend of strain softening, which is largely independent of the individual layer thickness.

By examining the microstructure and mechanical properties of annealed Mg/Ti multilayer films, it is found that Mg/Ti multilayers with $h \geq 5$ nm possess excellent capabilities in maintaining the lamellar structure and high strength at elevated temperatures. There is no significant change in the crystallography and morphology of these Mg/Ti multilayers after annealing up to at 200 °C for 2 h. Mg and Ti layers are still highly textured along c-axis, with sharp interfaces between each other. Nevertheless, for the Mg/Ti multilayers with h=2.5 nm, annealing at 200 °C for 2 h enhances the columnar boundaries. A transition zone with rearranged Mg and Ti atoms has been observed at some columnar boundaries.

In consistency with the impressive morphological stability, the hardness of Mg/Ti multilayers with $h \geq 5$ nm exhibit almost no change after annealing. A moderate strength

loss is noticed in annealed h=2.5 nm Mg/Ti multilayers, which is associated with the obvious morphological changes at this intrinsic size level. Based on the microstructural and mechanical evolution of Mg/Ti multilayers over a variety of annealing temperature and annealing time, the thermal stability of Mg/Ti multilayers is also a function of the length scale of h.

Mg/Zr, an HCP-based multilayer system characterized by coherent interfaces, has also been investigated in this study. The preliminary experimental results about the microstructure and mechanical behavior of as-deposited Mg/Zr multilayered nanofilms indicate that, both Mg and Zr layers are highly textured along c-axis and exhibit strong preference of epitaxial growth, which are largely independent on the individual layer thickness. At $h \geq 10$ nm, the strength of Mg/Zr multilayers generally increases with decreasing layer periodicity. However, a gradual decline of hardness occurs when h decreases from 10 nm to 2.5 nm.

6.2 Future Works

This dissertation presents a comprehensive study of the microstructure and mechanical behavior of magnetron sputtered Mg/Ti and Mg/Zr multilayer thin films, aiming to provide insights into the deformation mechanisms of HCP-based multilayers. Due to these objectives, several improvements onto current research need be considered.

In Chapter 3, we correlated the hardness or flow strength of Mg/Ti multilayers to the dislocation induced deformation mechanisms as a function of individual layer thickness. Although the theoretical predications agree well with our nanoindentation measurements, we are still short of evidence to determine the explicit dislocation motions. For example, the CLS model, which describes the propagation of a dislocation (Orowan-type loop)

confined within a layer, was used to explain the increasing strength of Mg/Ti multilayered nanofilms at $2.5 \leq h \leq 20$ nm. Mg and Ti were experimentally identified to preferentially grow along [0002] direction, with the basal plane of Mg parallel to the phase interface. At this condition, the dislocations will never be able to transmit the interface and enter into the adjacent Ti layer, without gliding on the non-basal slip systems of Mg. To determine the specific route of dislocations gliding, microstructural examinations, such as TEM and HRTEM, on the deformed Mg/Ti films are necessary. They will also be helpful for us to verify the effects of twining on the mechanical behavior of Mg/Ti multilayers. When we calculated the maximum flow strength, twinning was assumed to have limited contributions to the plastic deformation of Mg/Ti films.

Referring to Figure 3.6, there is an obvious dip on the strength versus $h^{-0.5}$ plot, corresponding to the comparative low hardness of the Mg/Ti multilayers with h=5 nm. We realized that it is lower than the predicted value from CLS model by ~0.68 GPa, as indicated in Figure 3.12. Unfortunately, the mechanism accounting for this “abnormal” hardness value has not been well understood yet. It is suggested that the quality of thin films is extremely sensitive to the deposition parameters. An unstable deposition environment will lead to the fluctuations in microstructure and mechanical performance of the films. Therefore, some more Mg/Ti multilayered nanofilms should be prepared to ensure the consistency in hardness measurement.

Mg/Ti multilayers with $h \geq 5$ nm exhibit no significant change in microstructure and hardness up to 200 °C annealing. However, for industrial applications, the critical temperature at which the loss in stiffness of the films begins ought to be identified. Thereby, the annealing with higher temperature, e.g. 300 °C and 400 °C, could be devised on Mg/Ti

multilayers in future work. The fact that Mg and Ti have vanishingly small mutual solubility to each other implies that, below 200 °C, a longer annealing time than 2 h might not bring about remarkable changes to the Mg/Ti multilayers with $h \geq 5$ nm from current experimental observations. In contrast, the microstructure and mechanical performance of h=2.5 nm specimens are expected to vary with annealing time since the transition zone detected in Figure 4.5 is a result of time-related atomic diffusion of Mg and Ti. The design of annealing with longer annealing time or higher annealing temperature should be valuable for our further studies of the thermal stability of Mg/Ti multilayers.

For as-deposited Mg/Ti multilayers, the microcompression measured flow strength deviates from the nanoindentation measured value when h decreases below 5 nm. We attributed this phenomenon to the epitaxial growth of Mg and Ti along (0002) and the different stress states arising from different tips used in these two mechanical tests. Nevertheless, the Mg/Ti films with h=2.5 nm exhibit obvious morphological changes after annealing. Whether this discrepancy in measuring flow strength remains at high temperatures is open to doubt. The microcompression experiments on annealed Mg/Ti multilayers are part of our ongoing efforts.

Mg/Zr multilayers were compared with Mg/Ti multilayers in mechanical properties to reveal the significance of lattice mismatch at the layer interfaces on the strength of HCP-based multilayers, whereas the modulus mismatch between layer constituents, which also greatly affects the strength level of metallic multilayers, was not specifically investigated in this work. Other multilayers, such as Ti/Zr, Mg/Zn, Mg/Y, etc., can be prepared and examined to reach a universal understanding of the deformation mechanisms in HCP-based multilayered nanofilms.

REFERENCES

[1] Jones RM. Mechanics of composite materials: Taylor & Francis London, 1975.

[2] Ritchie RO. The conflicts between strength and toughness. Nature Materials 2011;10:817.

[3] Munch E, Launey ME, Alsem DH, Saiz E, Tomsia AP, Ritchie RO. Tough, bio-inspired hybrid materials. Science 2008;322:1516.

[4] Ortiz C, Boyce MC. Bioinspired structural materials. Science 2008;319:1053.

[5] Tang Z, Kotov NA, Magonov S, Ozturk B. Nanostructured artificial nacre. Nature Materials 2003;2:413.

[6] Wang R, Suo Z, Evans A, Yao N, Aksay I. Deformation mechanisms in nacre. Journal of Materials Research 2001;16:2485.

[7] Song F, Soh A, Bai Y. Structural and mechanical properties of the organic matrix layers of nacre. Biomaterials 2003;24:3623.

[8] Mayer G. Rigid biological systems as models for synthetic composites. Science 2005;310:1144.

[9] Sellinger A, Weiss PM, Nguyen A, Lu Y, Assink RA, Gong W, Brinker CJ. Continuous self-assembly of organic–inorganic nanocomposite coatings that mimic nacre. Nature 1998;394:256.

[10] Waraich SM, Hering B, Burghard Z, Bill J, Behrens P, Menzel H. Fabrication and characterization of biocompatible nacre-like structures from alpha-zirconium hydrogen phosphate hydrate and chitosan. Journal of Colloid and Interface Science 2012;367:74.

[11] Misra A, Verdier M, Lu YC, Kung H, Mitchell TE, Nastasi N, Embury JD. Structure and mechanical properties of Cu-X (X=Nb, Cr, Ni) nanolayered composites. Scripta Materialia 1998;39:555.

[12] Davis JR. Properties and selection: nonferrous alloys and special-purpose materials: Asm Intl, 1990.

[13] Vepřek S, Reiprich S. A concept for the design of novel superhard coatings. Thin Solid Films 1995;268:64.

[14] Lehoczky S. Strength enhancement in thin-layered Al-Cu laminates. Journal of Applied Physics 1978;49:5479.

[15] Kuan S, Du X, Chou H, Huang J. Mechanical response of amorphous ZrCuTi/PdCuSi nanolaminates under nanoindentation. Surface and Coatings Technology 2011;206:1116.

[16] Launey ME, Munch E, Alsem DH, Saiz E, Tomsia AP, Ritchie RO. A novel biomimetic approach to the design of high-performance ceramic–metal composites. Journal of The Royal Society Interface 2010;7:741.

[17] Esaki L, Tsu R. Superlattice and negative differential conductivity in semiconductors. IBM Journal of Research and Development 1970;14:61.

[18] Robinson P, Harrison RJ, McEnroe SA, Hargraves RB. Lamellar magnetism in the haematite–ilmenite series as an explanation for strong remanent magnetization. Nature 2002;418:517.

[19] Balogh Z, Reda Chellali M, Greiwe G-H, Schmitz G, Erdélyi Z. Interface sharpening in miscible Ni/Cu multilayers studied by atom probe tomography. Applied Physics Letters 2011;99:181902.

[20] Misra A, Verdier M, Kung H, Embury JD, Hirth JP. Deformation mechanism maps for polycrystalline metallic multiplayers. Scripta Materialia 1999;41:973.

[21] Cammarata R, Schlesinger T, Kim C, Qadri S, Edelstein A. Nanoindentation study of the mechanical properties of copper/nickel multilayered thin films. Applied Physics Letters 1990;56:1862.

[22] Bunshah R, Nimmagadda R, Doerr H, Movchan B, Grechanuk N, Dabizha E. Structure and property relationships in microlaminate Ni-Cu and Fe-Cu condensates. Thin Solid Films 1980;72:261.

[23] Springer R, Catlett D. Structure and mechanical properties of Al/Al_xO_y vacuum-deposited laminates. Thin Solid Films 1978;54:197.

[24] Lloyd SJ, Molina-Aldareguia JM. Multilayered materials: a palette for the materials artist. Philosophical Transactions of the Royal Society of London. Series A: Mathematical, Physical and Engineering Sciences 2003;361:2931.

[25] Ruggiero ST, Barbee TW, Jr., Beasley MR. Superconductivity in quasi-two-dimensional layered composites. Physical Review Letters 1980;45:1299.

[26] Takenaka H, Nagai K, Ito H, Ichimaru S, Sakuma T, Namikawa K, Muramatsu Y, Gullikson E, Perera C. Soft x-ray reflectivity and thermal stability of CoCr/C multilayer X-ray mirrors. Surface Review and Letters 2002;9:593.

[27] Kondratenko V, Pershin YP, Poltseva O, Fedorenko A, Zubarev E, Yulin S, Sagitov S, Chirkov V, Levashov V, Vinogradov A. Thermal stability of soft x-ray Mo–Si and $MoSi_2$-Si multilayer mirrors. Applied optics 1993;32:1811.

[28] Takenaka H, Ichimaru S, Ohchi T, Gullikson E. Soft-X-ray reflectivity and heat resistance of SiC/Mg multilayer. Journal of Electron Spectroscopy and Related Phenomena 2005;144:1047.

[29] Jilek M, Cselle T, Holubar P, Morstein M, Veprek-Heijman M, Veprek S. Development of novel coating technology by vacuum arc with rotating cathodes for industrial production of nc-($Al_{1-x}Ti_x$) N/a-Si_3N_4 superhard nanocomposite coatings for dry, hard machining. Plasma Chemistry and Plasma Processing 2004;24:493.

[30] Veprek S. The search for novel, superhard materials. Journal of Vacuum Science and Technology A 1999;17:2401.

[31] Cselle T. Application of coatings for tooling quo vadis 2005. Vakuum in Forschung und Praxis 2005;17:33.

[32] Veprek S, Veprek-Heijman MJ. Industrial applications of superhard nanocomposite coatings. Surface and Coatings Technology 2008;202:5063.

[33] Barbee Jr T. Atomic engineering with multilayers. Science and Technology Review 1997.

[34] Padture NP, Gell M, Jordan EH. Thermal barrier coatings for gas-turbine engine applications. Science 2002;296:280.

[35] Evans AG, Mumm D, Hutchinson J, Meier G, Pettit F. Mechanisms controlling the durability of thermal barrier coatings. Progress in Materials Science 2001;46:505.

[36] Wright P, Evans A. Mechanisms governing the performance of thermal barrier coatings. Current Opinion in Solid State and Materials Science 1999;4:255.

[37] Clarke DR, Oechsner M, Padture NP. Thermal-barrier coatings for more efficient gas-turbine engines. MRS Bulletin 2012;37:891.

[38] Shen Y, Clarke DR, Fuierer PA. Anisotropic thermal conductivity of the Aurivillus phase, bismuth titanate ($Bi_4Ti_3O_{12}$): a natural nanostructured superlattice. Applied Physics Letters 2008;93:102907.

[39] Costescu R, Cahill D, Fabreguette F, Sechrist Z, George S. Ultra-low thermal conductivity in W/Al_2O_3 nanolaminates. Science 2004;303:989.

[40] Grünberg P. Layered magnetic structures in research and application. Acta Materialia 2000;48:239.

[41] Lu Y, Zhang J, Tian L, Li Y, Ma C. Microstructural evolution of unidirectionally solidified Nb_{SS}-Nb_5Si_3 eutectic alloy. Rare Metals 2011;30:335.

[42] Cui C, Zhang J, Wu K, Zou D, Ma Y, Liu L, Fu H. Directional solidification of Ni-Ni_3Si eutectic in situ composites by electron beam floating zone melting. Physica B: Condensed Matter 2012.

[43] Wang YM, Li J, Hamza AV, Barbee TW. Ductile crystalline–amorphous nanolaminates PNAS 2007;104:11155.

[44] Koehler JS. Attempt to Design a Strong Solid. Physical Review B 1970;2:547.

[45] Zhang JY, Zhang X, Wang RH, Lei SY, Zhang P, Niu JJ, Liu G, Zhang GJ, Sun J. Length-scale-dependent deformation and fracture behavior of Cu/X (X=Nb, Zr) multilayers: The constraining effects of the ductile phase on the brittle phase. Acta Materialia 2011;59:7368.

[46] Ross C. Electrodeposited multilayer thin films. Annual Review of Materials Science 1994;24:159.

[47] Mattox DM. Handbook of physical vapor deposition (PVD) processing: Access Online via Elsevier, 2010.

[48] Rossnagel S. Thin film deposition with physical vapor deposition and related technologies. Journal of Vacuum Science & Technology A: Vacuum, Surfaces, and Films 2003;21:S74.

[49] Arnell R, Kelly P. Recent advances in magnetron sputtering. Surface and Coatings Technology 1999;112:170.

[50] Kelly P, Arnell R. Magnetron sputtering: a review of recent developments and applications. Vacuum 2000;56:159.

[51] Blum W. The structure and properties of alternately deposited metals. Transactions of the American Electrochemical Society 1921;40:307.

[52] Schlesinger M, Paunovic M. Modern electroplating: Wiley, 2011.

[53] Toth-Kadar E, Peter L, Becsei T, Tóth J, Pogány L, Tarnóczi T, Kamasa P, Lang G, Cziraki A, Schwarzacher W. Preparation and magnetoresistance characteristics of electrodeposited Ni-Cu alloys and Ni-Cu/Cu multilayers. Journal of the Electrochemical Society 2000;147:3311.

[54] Lenczowski S, Schönenberger C, Gijs M, De Jonge W. Giant magnetoresistance of electrodeposited Co/Cu multilayers. Journal of Magnetism and Magnetic Materials 1995;148:455.

[55] Jyoko Y, Kashiwabara S, Hayashi Y. Preparation of giant magnetoresistance Co/Cu multilayers by electrodeposition. Journal of The Electrochemical Society 1997;144:L5.

[56] Tench D, White J. Enhanced tensile strength for electrodeposited nickel-copper multilayer composites. Metallurgical transactions A 1984;15:2039.

[57] Saito Y, Utsunomiya H, Tsuji N, Sakai T. Novel ultra-high straining process for bulk materials—development of the accumulative roll-bonding (ARB) process. Acta Materialia 1999;47:579.

[58] Zheng S, Beyerlein I, Wang J, Carpenter J, Han W, Mara N. Deformation twinning mechanisms from bimetal interfaces as revealed by in situ straining in the TEM. Acta Materialia 2012;60:5858.

[59] Lee S-B, LeDonne J, Lim S, Beyerlein I, Rollett A. The heterophase interface character distribution of physical vapor-deposited and accumulative roll-bonded Cu–Nb multilayer composites. Acta Materialia 2012;60:1747.

[60] Beyerlein IJ, Mara NA, Wang J, Carpenter JS, Zheng SJ, Han WZ, Zhang RF, Kang K, Nizolek T, Pollock TM. Structure–property–functionality of bimetal interfaces. JOM 2013;64:1192.

[61] Lim S, Rollett A. Length scale effects on recrystallization and texture evolution in Cu layers of a roll-bonded Cu–Nb composite. Materials Science and Engineering: A 2009;520:189.

[62] Han WZ, Carpenter JS, Wang J, Beyerlein IJ, Mara NA. Atomic-level study of twin nucleation from face-centered-cubic/body-centered-cubic interfaces in nanolamellar composites. Applied Physics Letters 2012;100:11911.

[63] Zheng S, Beyerlein IJ, Carpenter JS, Kang K, Wang J, Han W, Mara NA. High-strength and thermally stable bulk nanolayered composites due to twin-induced interfaces. Nature Communications 2013;4:1696.

[64] Misra A, Zhang X, Hammon D, Hoagland R. Work hardening in rolled nanolayered metallic composites. Acta Materialia 2005;53:221.

[65] Zhu X, Liu X, Zong R, Zeng F, Pan F. Microstructure and mechanical properties of nanoscale Cu/Ni multilayers. Materials Science and Engineering: A 2010;527:1243.

[66] Josell D, Van Heerden D, Read D, Bonevich J, Shechtman D. Tensile testing low density multilayers: aluminum/titanium. Journal of Materials Research-Pittsburgh 1998;13:2902.

[67] Mara NA, Bhattacharyya D, Dickerson P, Hoagland RG, Misra A. Deformability of ultrahigh strength 5 nm Cu/Nb nanolayered composites. Applied Physics Letters 2008;92.

[68] Kim Y, Budiman AS, Baldwin JK, Mara NA, Misra A, Han SM. Microcompression study of Al-Nb nanoscale multilayers. Journal of Materials Research 2012;27:592.

[69] Han SM, Phillips MA, Nix WD. Study of strain softening behavior of Al–Al_3Sc multilayers using microcompression testing. Acta Materialia 2009;57:4473.

[70] Mara N, Sergueeva A, Misra A, Mukherjee A. Structure and high-temperature mechanical behavior relationship in nano-scaled multilayered materials. Scripta Materialia 2004;50:803.

[71] Misra A, Hirth JP, Hoagland RG. Length-scale-dependent deformation mechanisms in incoherent metallic multilayered composites. Acta Materialia 2005;53:4817.

[72] Fu EG, Li N, Misra A, Hoagland RG, Wang H, Zhang X. Mechanical properties of sputtered Cu/V and Al/Nb multilayer films. Materials Science and Engineering a-Structural Materials Properties Microstructure and Processing 2008;493:283.

[73] Wen S, Zong R, Zeng F, Gao Y, Pan F. Evaluating modulus and hardness enhancement in evaporated Cu/W multilayers. Acta Materialia 2007;55:345.

[74] McKeown J, Misra A, Kung H, Hoagland RG, Nastasi M. Microstructures and strength of nanoscale Cu-Ag multilayers. Scripta Materialia 2002;46:593.

[75] Huang H, Spaepen F. Tensile testing of free-standing Cu, Ag and Al thin films and Ag/Cu multilayers. Acta Materialia 2000;48:3261.

[76] Zhang X, Misra A, Wang H, Shen TD, Nastasi M, Mitchell TE, Hirth JP, Hoagland RG, Embury JD. Enhanced hardening in Cu/330 stainless steel multilayers by nanoscale twinning. Acta Materialia 2004;52:995.

[77] Zhang X, Misra A, Wang H, Kung H, Embury J, Hoagland R, Nastasi M. Microstructures and mechanical properties of nanostructured copper-304 stainless steel multilayers synthesized by magnetron sputtering. Materials Research Society Symposium Proceedings 2003;740:49.

[78] Zhu X-Y, Liu X-J, Zeng F, Pan F. Microstructure and nanoindentation hardness of Ag/Fe multilayers. Transactions of Nonferrous Metals Society of China 2010;20:110.

[79] Yu K, Liu Y, Rios S, Wang H, Zhang X. Strengthening mechanisms of Ag/Ni immiscible multilayers with fcc/fcc interface. Surface and Coatings Technology 2013.

[80] Ham B, Zhang X. High strength Mg/Nb nanolayer composites. Materials Science and Engineering A-Structural Materials Properties Microstructure and Processing 2011;528:2028.

[81] Phillips M, Clemens B, Nix W. Microstructure and nanoindentation hardness of Al/Al_3Sc multilayers. Acta Materialia 2003;51:3171.

[82] Mara N, Misra A, Hoagland R, Sergueeva A, Tamayo T, Dickerson P, Mukherjee A. High-temperature mechanical behavior/microstructure correlation of Cu/Nb nanoscale multilayers. Materials Science and Engineering: A 2008;493:274.

[83] Zhu X, Li Y, Zhang G, Tan J, Liu Y. Understanding nanoscale damage at a crack tip of multilayered metallic composites. Applied Physics Letters 2008;92:161905.

[84] Li Y, Zhang G. On plasticity and fracture of nanostructured Cu/X (X=Au, Cr) multilayers: The effects of length scale and interface/boundary. Acta Materialia 2010;58:3877.

[85] Wang YC, Misra A, Hoagland RG. Fatigue properties of nanoscale Cu/Nb multilayers. Scripta Materialia 2006;54:1593.

[86] Kang BC, Kim HY, Kwon OY, Hong SH. Bilayer thickness effects on nanoindentation behavior of Ag/Ni multilayers. Scripta Materialia 2007;57:703.

[87] Shen Y-L, Suresh S. Steady-state creep of metal-ceramic multilayered materials. Acta Materialia 1996;44:1337.

[88] Misra A, Demkowicz M, Zhang X, Hoagland R. The radiation damage tolerance of ultra-high strength nanolayered composites. JOM 2007;59:62.

[89] Demkowicz MJ, Hoagland RG, Hirth JP. Interface structure and radiation damage resistance in Cu-Nb multilayer nanocomposites. Physical Review Letters 2008;100:136102.

[90] Yu K, Sun C, Chen Y, Liu Y, Wang H, Kirk M, Li M, Zhang X. Superior tolerance of Ag/Ni multilayers against Kr ion irradiation: an in situ study. Philosophical Magazine 2013;93:3547.

[91] Misra A, Hirth JP, Kung H. Single-dislocation-based strengthening mechanisms in nanoscale metallic multilayers. Philosophical Magazine 2002;82:2935.

[92] Hall E. The deformation and ageing of mild steel: III discussion of results. Proceedings of the Physical Society: Section B 1951;64:747.

[93] Petch N. The cleavage strength of polycrystals. Journal of Iron and Steel Institute 1953;174:25.

[94] Courtney TH. Mechanical behavior of materials: McGraw-Hill, 1990.

[95] Li JCM. Petch relation and grain boundary sources. Transactions of the Metallurgical Society of AIME 1963;227:239.

[96] Ashby MF. The deformation of plastically non-homogeneous materials. Philosophical Magazine 1970;21:399.

[97] Louchet F, Weiss J, Richeton T. Hall-Petch law revisited in terms of collective dislocation dynamics. Physical Review Letters 2006;97:075504.

[98] Carlton C, Ferreira P. What is behind the inverse Hall–Petch effect in nanocrystalline materials? Acta Materialia 2007;55:3749.

[99] Meyers MA, Mishra A, Benson DJ. Mechanical properties of nanocrystalline materials. Progress in Materials Science 2006;51:427.

[100] Barnett MR, Keshavarz Z, Beer AG, Atwell D. Influence of grain size on the compressive deformation of wrought Mg-3Al-1Zn. Acta Materialia 2004;52:5093.

[101] Chokshi AH, Rosen A, Karch J, Gleiter H. On the validity of the Hall-Petch relationships in nanocrystalline materials. Scripta Metallurgica 1989;23:1679.

[102] Fu H-H, Benson DJ, Meyers MA. Analytical and computational description of effect of grain size on yield stress of metals. Acta Materialia 2001;49:2567.

[103] Liu Y, Bufford D, Wang H, Sun C, Zhang X. Mechanical properties of highly textured Cu/Ni multilayers. Acta Materialia 2011;59:1924.

[104] Anderson PM, Li C. Hall-Petch relations for multilayered materials. Nanostructured Materials 1995;5:349.

[105] Embury J, Hirth J. On dislocation storage and the mechanical response of fine scale microstructures. Acta metallurgica et materialia 1994;42:2051.

[106] Nix WD. Mechanical-properties of thin-films. Metallurgical Transactions a-Physical Metallurgy and Materials Science 1989;20:2217.

[107] Phillips MA, Clemens BM, Nix WD. A model for dislocation behavior during deformation of Al/Al_3Sc (fcc/L1(2)) metallic multilayers. Acta Materialia 2003;51:3157.

[108] Misra A, Hirth JP, Hoagland RG, Embury JD, Kung H. Dislocation mechanisms and symmetric slip in rolled nano-scale metallic multilayers. Acta Materialia 2004;52:2387.

[109] Zhang J, Niu J, Zhang X, Zhang P, Liu G, Zhang G, Sun J. Tailoring nanostructured Cu/Cr multilayer films with enhanced hardness and tunable modulus. Materials Science and Engineering: A 2012;543:139.

[110] Lehoczky S. Strength enhancement in thin-layered Al-Cu laminates. Journal of Applied Physics 1978;49:5479.

[111] Ramaswamy V, Nix WD, Clemens BM. Coherency and surface stress effects in metal multilayers. Scripta Materialia 2004;50:711.

[112] Hoagland RG, Kurtz RJ, Henager CH. Slip resistance of interfaces and the strength of metallic multilayer composites. Scripta Materialia 2004;50:775.

[113] Zhang JY, Zhang P, Zhang X, Wang RH, Liu G, Zhang GJ, Sun J. Mechanical properties of fcc/fcc Cu/Nb nanostructured multilayers. Materials Science and Engineering A-Structural Materials Properties Microstructure and Processing 2012;545:118.

[114] Niu JJ, Zhang JY, Liu G, Zhang P, Lei SY, Zhang GJ, Sun J. Size-dependent deformation mechanisms and strain-rate sensitivity in nanostructured Cu/X (X=Cr, Zr) multilayer films. Acta Materialia 2012;60:3677.

[115] Lu L, Shen YF, Chen XH, Qian LH, Lu K. Ultrahigh strength and high electrical conductivity in copper. Science 2004;304:422.

[116] Rao SI, Hazzledine PM. Atomistic simulations of dislocation–interface interactions in the Cu-Ni multilayer system. Philosophical Magazine A 2000;80:2011.

[117] Mara NA, Bhattacharyya D, Dickerson P, Hoagland RG, Misra A. Ultrahigh strength and ductility of Cu-Nb nanolayered composites. In: Zhao Y, Liao X, editors. Ductility of Bulk Nanostructured Materials 2010;633-634:647.

[118] Mara NA, Bhattacharyya D, Hirth JP, Dickerson P, Misra A. Mechanism for shear banding in nanolayered composites. Applied Physics Letters 2010;97:021909.

[119] Wei Q, Kecskes L, Jiao T, Hartwig K, Ramesh K, Ma E. Adiabatic shear banding in ultrafine-grained Fe processed by severe plastic deformation. Acta Materialia 2004;52:1859.

[120] Li Y, Tan J, Zhang G. Interface instability within shear bands in nanoscale Au/Cu multilayers. Scripta Materialia 2008;59:1226.

[121] Dayal P, Quadir M, Kong C, Savvides N, Hoffman M. Transition from dislocation controlled plasticity to grain boundary mediated shear in nanolayered aluminum/palladium thin films. Thin Solid Films 2011;519:3213.

[122] Zhang JY, Lei S, Liu Y, Niu JJ, Chen Y, Liu G, Zhang X, Sun J. Length scale-dependent deformation behavior of nanolayered Cu/Zr micropillars. Acta Materialia 2012;60:1610.

[123] Zarkades A, Larson F, Jaffee R, Promisel N. The science, technology and application of titanium. Pergamon Press, Oxford, UK, 1970.

[124] Yoo M, Wei C. Slip modes of hexagonal-close-packed metals. Journal of Applied Physics 1967;38:4317.

[125] Avedesian MM, Baker H. Magnesium and magnesium alloys. Materials Park, OH 44073: ASM International, 1999.

[126] Hutchinson WB, Barnett MR. Effective values of critical resolved shear stress for slip in polycrystalline magnesium and other hcp metals. Scripta Materialia 2010;63:737.

[127] Reedhill RE, Robertson WD. Deformation of magnesium single crystals by nonbasal slip. Transactions of the American Institute of Mining and Metallurgical Engineers 1957;209:496.

[128] Byer CM, Li B, Cao B, Ramesh K. Microcompression of single-crystal magnesium. Scripta Materialia 2010;62:536.

[129] Koike J, Kobayashi T, Mukai T, Watanabe H, Suzuki M, Maruyama K, Higashi K. The activity of non-basal slip systems and dynamic recovery at room temperature in fine-grained AZ31B magnesium alloys. Acta Materialia 2003;51:2055.

[130] Hauser FE, Landon PR, Dorn JE. Fracture of magnesium alloys at low temperature. Transactions of the American Institute of Mining and Metallurgical Engineers 1956;206:589.

[131] Partridge P. The crystallography and deformation modes of hexagonal close-packed metals. International Materials Reviews 1967;12:169.

[132] Chun Y, Davies C. Investigation of prism <a> slip in warm-rolled AZ31 alloy. Metallurgical and Materials Transactions A 2011;42:4113.

[133] Yoshinaga H, Horiuchi R. Deformation mechanisms in magnesium single crystals compressed in the direction parallel to hexagonal axis. JIM 1963;4:1.

[134] Serra A, Bacon D. A new model for {1012} twin growth in hcp metals. Philosophical Magazine A 1996;73:333.

[135] Wu XL, Youssef KM, Koch CC, Mathaudhu SN, Kecskes LJ, Zhu YT. Deformation twinning in a nanocrystalline hcp Mg alloy. Scripta Materialia 2011;64:213.

[136] Li B, Ma E. Zonal dislocations mediating twinning in magnesium. Acta Materialia 2009;57:1734.

[137] Lütjering G, Williams JJC. Titanium: Springer, 2007.

[138] Levine ED. Deformation mechanisms in titanium at low temperatures. Transactions of the Metallurgical Society of AIME 1966;236:1558.

[139] Akhtar A, Teghtsoonian E. Prismatic slip in alpha-titanium single-crystals. Metallurgical Transactions A-Physical Metallurgy and Materials Science 1975;6:2201.

[140] Westlake DG, Levine ED. Discussion of deformation mechanisms in titanium at low temperatures. Transactions of the Metallurgical Society of AIME 1967;239:1101.

[141] Williams J, Baggerly R, Paton N. Deformation behavior of HCP Ti-Al alloy single crystals. Metallurgical and Materials Transactions A 2002;33:837.

[142] Gong J, Wilkinson AJ. Micro-cantilever testing of ⟨a⟩ prismatic slip in commercially pure Ti. Philosophical Magazine 2011;91:1137.

[143] Sun QY, Guo Q, Yao X, Xiao L, Greer JR, Sun J. Size effects in strength and plasticity of single-crystalline titanium micropillars with prismatic slip orientation. Scripta Materialia 2011;65:473.

[144] Wang J, Hoagland R, Hirth J, Capolungo L, Beyerlein I, Tomé C. Nucleation of a twin in hexagonal close-packed crystals. Scripta Materialia 2009;61:903.

[145] Yoo M. Slip, twinning, and fracture in hexagonal close-packed metals. Metallurgical transactions A 1981;12:409.

[146] Wang J, Hirth J, Tomé C. Twinning nucleation mechanisms in hexagonal-close-packed crystals. Acta Materialia 2009;57:5521.

[147] Capolungo L, Beyerlein I. Nucleation and stability of twins in hcp metals. Physical Review B 2008;78:024117.

[148] Akhtar A. Compression of zirconium single crystals parallel to the c-axis. Journal of Nuclear Materials 1973;47:79.

[149] Akhtar A, Teghtsoonian A. Plastic deformation of zirconium single crystals. Acta Metallurgica 1971;19:655.

[150] Akhtar A. Prismatic slip in zirconium single crystals at elevated temperatures. Metallurgical transactions A 1975;6:1217.

[151] Akhtar A. Basal slip in zirconium. Acta Metallurgica 1973;21:1.

[152] Mason T, Bingert J, Kaschner G, Wright S, Larsen R. Advances in deformation twin characterization using electron backscattered diffraction data. Metallurgical and Materials Transactions A 2002;33:949.

[153] McCabe R, Cerreta E, Misra A, Kaschner G, Tomé C. Effects of texture, temperature and strain on the deformation modes of zirconium. Philosophical Magazine 2006;86:3595.

[154] Morrow B, McCabe R, Cerreta E, Tomé C. Variability in EBSD statistics for textured zirconium. Materials Science and Engineering: A 2013;574:157.

[155] McCabe RJ, Proust G, Cerreta EK, Misra A. Quantitative analysis of deformation twinning in zirconium. International Journal of Plasticity 2009;25:454.

[156] Kaschner G, Tomé C, McCabe R, Misra A, Vogel S, Brown D. Exploring the dislocation/twin interactions in zirconium. Materials Science and Engineering: A 2007;463:122.

[157] Baldi A, Pálsson GK, Gonzalez-Silveira M, Schreuders H, Slaman M, Rector JH, Krishnan G, Kooi BJ, Walker GS, Fay MW, Hjörvarsson B, Wijngaarden RJ, Dam B, Griessen R. Mg/Ti multilayers: structural and hydrogen absorption properties. Physical Review B 2010;81:224203.

[158] Murray J. The Mg-Ti (magnesium-titanium) system. Bulletin of Alloy Phase Diagrams 1986;7:245.

[159] Klug HP, Alexander LE. X-ray diffraction procedures: for polycrystalline and amorphous materials. X-Ray Diffraction Procedures: For Polycrystalline and Amorphous Materials, 2nd Edition, by Harold P. Klug, Leroy E. Alexander, pp. 992. ISBN 0-471-49369-4. Wiley-VCH, May 1974. 1974;1.

[160] Noyan I, Huang T, York B. Residual stress/strain analysis in thin films by x-ray diffraction. Critical Reviews in Solid State and Material Sciences 1995;20:125.

[161] Fullerton EE, Schuller IK, Vanderstraeten H, Bruynseraede Y. Structural refinement of superlattices from x-ray diffraction. Physical Review B 1992;45:9292.

[162] Bhushan B, Koinkar VN. Nanoindentation hardness measurements using atomic force microscopy. Applied Physics Letters 1994;64:1653.

[163] Oliver WC, Pharr GM. Measurement of hardness and elastic modulus by instrumented indentation: advances in understanding and refinements to methodology. Journal of Materials Research 2004;19:3.

[164] Li X, Bhushan B. A review of nanoindentation continuous stiffness measurement technique and its applications. Materials Characterization 2002;48:11.

[165] D Nix W. Elastic and plastic properties of thin films on substrates: nanoindentation techniques. Materials Science and Engineering: A 1997;234:37.

[166] Saha R, Nix WD. Effects of the substrate on the determination of thin film mechanical properties by nanoindentation. Acta Materialia 2002;50:23.

[167] Buckle H. Use of the hardness test to determine other material properties. In: Westbrook JH, Conrad H, editors. The Science of Hardness Testing and Its Research Applications. Metals Park, Ohio: The American Society for Metals, 1972. p.453.

[168] Uchic MD, Shade PA, Dimiduk DM. Micro-compression testing of fcc metals: a selected overview of experiments and simulations. JOM 2009;61:36.

[169] Schuster B, Wei Q, Hufnagel T, Ramesh K. Size-independent strength and deformation mode in compression of a Pd-based metallic glass. Acta Materialia 2008;56:5091.

[170] Lee CJ, Huang JC, Nieh TG. Sample size effect and microcompression of $Mg_{65}Cu_{25}Gd_{10}$ metallic glass. Applied Physics Letters 2007;91.

[171] Biener J, Hodge AM, Hayes JR, Volkert CA, Zepeda-Ruiz LA, Hamza AV, Abraham FF. Size effects on the mechanical behavior of nanoporous Au. Nano letters 2006;6:2379.

[172] Ramesh K. Nanomaterials: mechanics and mechanisms, 2009. Dordrecht: Springer.

[173] Uchic MD, Shade PA, Dimiduk DM. Plasticity of micrometer-scale single crystals in compression. Annual Review of Materials Research 2009;39:361.

[174] Zhang H, Schuster BE, Wei Q, Ramesh KT. The design of accurate micro-compression experiments. Scripta Materialia 2006;54:181.

[175] Shan Z, Mishra RK, Asif SS, Warren OL, Minor AM. Mechanical annealing and source-limited deformation in submicrometre-diameter Ni crystals. Nature Materials 2007;7:115.

[176] Carpenter JS, Misra A, Uchic MD, Anderson PM. Strain rate sensitivity and activation volume of Cu/Ni metallic multilayer thin films measured via micropillar compression. Applied Physics Letters 2012;101.

[177] Wei Q. Strain rate effects in the ultrafine grain and nanocrystalline regimes--its influence on some constitutive behavior. Journal of Materials Science 2007;42:1709.

[178] Wei Q, Cheng S, Ramesh KT, Ma E. Effect of nanocrystalline and ultrafine grain sizes on the strain rate sensitivity and activation volume: fcc versus bcc metals. Materials Science and Engineering A 2004;381:71.

[179] Tabor D. A simple theory of static and dynamic hardness. Proceedings of the Royal Society, London A 1948;192:247.

[180] Soderberg H, Oden M, Molina-Aldareguia JM, Hultman L. Nanostructure formation during deposition of TiN/SiN_x nanomultilayer films by reactive dual magnetron sputtering. Journal of Applied Physics 2005;97:114327.

[181] Shull AL, Spaepen F. Measurements of stress during vapor deposition of copper and silver thin films and multilayers. Journal of Applied Physics 1996;80:6243.

[182] Schuller IK. New class of layered materials. Physical Review Letters 1980;44:1597.

[183] Williams DB, Carter CB. Transmission electron microscopy Springer, 1996.

[184] Oliver WC, Pharr GM. An improved technique for determining hardness and elastic modulus using load and displacement sensing indentation experiments. Journal of Materials Research 1992;7:1564.

[185] Meyers MA, Mishra A, Benson DJ. Mechanical properties of nanocrystalline materials. Progress in Materials Science 2006;51:427.

[186] Schuster BE, Wei Q, Hufnagel TC, Ramesh KT. Size-independent strength and deformation mode in compression of a Pd-based metallic glass. Acta Materialia 2008;56:5091.

[187] Wu XL, Guo YZ, Wei Q, Wang WH. Prevalence of shear banding in compression of $Zr_{41}Ti_{14}Cu_{12.5}Ni_{10}Be_{22.5}$ pillars as small as 150 nm in diameter Acta Materialia 2009;57:3562.

[188] Zhang J, Lei S, Niu J, Liu Y, Liu G, Zhang X, Sun J. Intrinsic and extrinsic size effects on deformation in nanolayered Cu/Zr micropillars: from bulk-like to small-volume materials behavior. Acta Materialia 2012;60:4054.

[189] Dorn J, Mitchell J. High strength materials. John Wiley, New York 1965:510.

[190] Trojanova Z, Lukac P, Szaraz Z. Deformation behavior of nanocrystalline Mg studied at elevated temperatures. Reviews on Advanced Materials Science 2005;10:437.

[191] Hwang S, Nishimura C, McCormick PG. Deformation mechanism of nanocrystalline magnesium in compression. Scripta Materialia 2001;44:1507.

[192] Conrad H. High strength materials. John Wiley, New York 1965;1:145.

[193] Jia D, Wang Y, Ramesh K, Ma E, Zhu Y, Valiev R. Deformation behavior and plastic instabilities of ultrafine-grained titanium. Applied Physics Letters 2001;79:611.

[194] Massalski TB. Binary alloy phase diagrams. Materials Park: ASM International, 1990.

[195] Shewmon P. Diffusion in solids, 1989.

[196] Asano K, Enoki H, Akiba E. Synthesis of HCP, FCC and BCC structure alloys in the Mg-Ti binary system by means of ball milling. Journal of Alloys and Componds 2009;480:558.

[197] Lowe W, Geballe T. NbZr multilayers. I. structure and superconductivity. Physical Review B 1984;29:4961.

[198] Bain JA, Chyung LJ, Brennan S, Clemens BM. Elastic strains and coherency stresses in Mo/Ni multilayers. Physical Review B 1991;44:1184.

[199] Zheng JG, Partridge PG, Steeds JW, Wilkes DMJ, WardClose CM. Microstructure of vapour quenched Ti-29 wt% Mg alloy solid solution. Journal of Materials Science 1997;32:3089.

[200] Wei Q, Misra A. Transmission electron microscopy study of the microstructure and crystallographic orientation relationships in V/Ag multilayers. Acta Materialia 2010;58:4871.

[201] Freund LB, Suresh S. Thin film materials: stress, defect formation and surface evolution: Cambridge University Press, 2004.

[202] Matthews JW, Blakeslee AE. Defects in epitaxial multilayers: misfit dislocations. Journal of Crystal Growth 1974;27:118.

[203] Matthews J. Defects associated with the accommodation of misfit between crystals. Journal of Vacuum Science and Technology 1975;12:126.

[204] Niinomi M. Mechanical properties of biomedical titanium alloys. Materials Science and Engineering A-Structural Materials Properties Microstructure and Processing 1998;243:231.

[205] Yin WH, Xu F, Ertorer O, Pan Z, Zhang XY, Kecskes LJ, Lavernia EJ, Wei Q. Mechanical behavior of microstructure engineered multi-length-scale titanium over a wide range of strain rates. Acta Materialia 2013;61:3781.

[206] International A. Properties and selection: nonferrous alloys and special-purpose materials. Ohio: ASM International, 1990.

[207] Anderson P, Foecke T, Hazzledine P. Dislocation-based deformation mechanisms in metallic nanolaminates. MRS Bulletin-Materials Research Society 1999;24:27.

[208] Knorr I, Cordero N, Lilleodden E, Volkert C. Mechanical behavior of nanoscale Cu/PdSi multilayers. Acta Materialia 2013.

[209] Yoo MH. Slip, twinning, and fracture in hexagonal close-packed metals. Metallurgical Transactions A-Physical Metallurgy and Materials Science 1981;12:409.

[210] Akhtar A. Basal slip and twinning in alpha-titanium single-crystals. Metallurgical Transactions 1975;A 6:1105.

[211] Paton NE, Backofen WA. Plastic deformation of titanium at elevated temperatures. Metallurgical Transactions 1970;1:2839.

[212] Yoshinaga H. Deformation mechanisms in magnesium single crystals compressed in the direction parallel to hexagonal axis. Transactions of the Japan Institute of Metals 1963;4:1.

[213] Larsson PL, Giannakopoulos AE, Soderlund E, Rowcliffe DJ, Vestergaard R. Analysis of Berkovich indentation. International Journal of Solids and Structures 1996;33:221.

[214] Lu Y, Kotoka R, Ligda J, Cao B, Yarmolenko S, Schuster B, Wei Q. The microstructure and mechanical behavior of Mg/Ti multilayers as a function of individual layer thickness. Acta Materialia 2014;63:216.

[215] Lei S, Zhang JY, Niu JJ, Liu G, Zhang X, Sun J. Intrinsic size-controlled strain hardening behavior of nanolayered Cu/Zr micropillars. Scripta Materialia 2012;66:706.

[216] Yu Q, Shan ZW, Li J, Huang XX, Xiao L, Sun J, Ma E. Strong crystal size effect on deformation twinning. Nature 2010;463:335.

[217] Lilleodden E. Microcompression study of Mg (0001) single crystal. Scripta Materialia 2010;62:532.

[218] Zhang JY, Wang YQ, Wu K, Zhang P, Liu G, Zhang GJ, Sun J. Strain rate sensitivity of nanolayered Cu/X (X=Cr, Zr) micropillars: Effects of heterophase interface/twin boundary. Materials Science and Engineering: A 2014;612:28.

[219] Weihs TP, Barbee TW, Wall MA. Hardness, ductility, and thermal processing of Cu/Zr and Cu/Cu-Zr nanoscale multilayer foils. Acta Materialia 1997;45:2307.

[220] Lee H-J, Kwon K-W, Ryu C, Sinclair R. Thermal stability of a Cu/Ta multilayer: an intriguing interfacial reaction. Acta Materialia 1999;47:3965.

[221] Jiang Z, Jiang X, Liu W, Wu Z. Thermal stability of multilayer films Pt/Si, W/Si, Mo/Si, and W/C. Journal of Applied Physics 1989;65:196.

[222] Kucharska B, Kulej E, Wrobel A. Thermal stability of the Cu/Ni multilayer system in X-ray diffraction and scanning microscopy examinations. Optica Applicata 2012;4:725.

[223] Kucharska B, KuLej E, Gwozdzik M. Evaluation of the temperature stability of a Cu/Ni multilayer. Archives of Metallurgy and Materials 2012;57:671.

[224] Beke D, Langer G, Kis-Varga M, Dudas A, Nemes P, Daróczi L, Kerekes G, Erdélyi Z. Thermal stability of amorphous and crystalline multilayers produced by magnetron sputtering. Vacuum 1998;50:373.

[225] Dudás A, Langer G, Beke D, Kis-Varga M, Daróczi L, Erdélyi Z. Thermal stability of Mo–V epitaxial multilayers. Journal of Applied Physics 1999;86:2008.

[226] Zhai Q, Kongq D, Morrone A, Ebrahimi F. Characterization of high strength Cu/Ag multilayered composites. Materials Research Society Symposium Proceedings, vol. 451: Cambridge University Press, 1997. p.489.

[227] Czigány Z, Kovacs I, Radnoczi G. Growth and microstructure of sputtered Ag/Cu multilayers. Thin Solid Films 1998;317:266.

[228] Wen S, Zong R, Zeng F, Gu Y, Gao Y, Pan F. Thermal stability of microstructure and mechanical properties of Ni/Ru multilayers. Surface and Coatings Technology 2008;202:2040.

[229] Misra A, Hoagland R, Kung H. Thermal stability of self-supported nanolayered Cu/Nb films. Philosophical Magazine 2004;84:1021.

[230] Misra A, Hoagland R. Effects of elevated temperature annealing on the structure and hardness of copper/niobium nanolayered films. Journal of Materials Research 2005;20:2046.

[231] Yang Q, Zhao LR. Thermal stability of polycrystalline TiN/CrN superlattice coatings. Journal of Vacuum Science and Technology A 2003;21:558.

[232] Sharma G, Ramanujan R, Tiwari G. Instability mechanisms in lamellar microstructures. Acta Materialia 2000;48:875.

[233] Mazor A, Srolovitz D, Hagan P, Bukiet, BG. Columnar growth in thin films. Physical Review Letters 1988;60:424.

[234] Han Y, Zhuang H, Lu J. Deformation-induced ambient temperature α-to-β phase transition and nanocrystallization in (α+ β) titanium alloy. Journal of Materials Research 2009;24:3439.

[235] Jona F, Marcus P. Magnesium under pressure: structure and phase transition. Journal of Physics: Condensed Matter 2003;15:7727.

[236] Junkaew A, Ham B, Zhang X, Talapatra A, Arróyave R. Stabilization of bcc Mg in thin films at ambient pressure: experimental evidence and ab initio calculations. Materials Research Letters 2013;1:161.

[237] Josell D, Spaepen F. Surfaces, interfaces, and changing shapes in multilayered films. MRS Bulletin 1999;24:39.

[238] Knoedler HL, Lucas G, Levi C. Morphological stability of copper-silver multilayer thin films at elevated temperatures. Metallurgical and Materials Transactions A 2003;34:1043.

LIST OF PUBLICATIONS AND PRESENTATIONS

1. Lu Y, Kotoka R, Ligda J, Cao B, Yarmolenko S, Schuster B and Wei Q. The microstructure and mechanical behavior of Mg/Ti multilayers as a function of individual layer thickness. *Acta Materialia* 2014;63:216.

2. Lu Y, Ligda J, Kotoka R, Schuster B, Yarmolenko S and Wei Q. The intrinsic size-dependent plasticity of Mg/Ti metallic multilayers. (*To be submitted).*

3. Lu Y, Kotoka R, Ligda J, Cao B, Yarmolenko S, Schuster B and Wei Q. The microstructure and mechanical behavior of multilayered Mg/Ti Nanofilm as a function of layer thickness. *MRS 2012 Fall Meeting (Oral).*

4. Lu Y, Kotoka R, Ligda J, Cao B, Yarmolenko S, Schuster B and Wei Q. Microstructure and Mechanical Behavior of HCP-based Multilayers at Nanoscale. *TMS 2014 Annual Meeting and Exhibition (Poster).*

5. Lu Y, Kotoka R, Ligda J, Yarmolenko S, Schuster B and Wei Q. The intrinsic size-dependent plasticity of MgTi multilayer thin films. *TMS 2015 Annual Meeting and Exhibition (Abstract accepted).*

VITA

Yuanyuan Lu was born and raised in Anqing city, located at west-southern part of Anhui Province in China. After completing the middle school and high school studies in Huaining Middle School, she was enrolled at Beijing University of Science and Technology in 2003, majoring Material Processing and Control Engineering. Four years later, she was recommended to the Department of Material Science and Engineering at Beihang University for graduate studies. She obtained her master degree in 2010 and then was admitted to the PhD program of Mechanical Engineering in the University of North Carolina at Charlotte.